Investigating the evolution of the aluminum-silicon coating on 22MnB5 steel during heating

by

Cameron Klassen

A thesis

presented to the University of Waterloo

in fulfillment of the

thesis requirement for the degree of

Master of Applied Science

in

Mechanical and Mechatronics Engineering

Waterloo, Ontario, Canada, 2022

Author's Declaration

I hereby declare that I am the sole author of this thesis. This is a true copy of the thesis, including any required final revisions, as accepted by my examiners.

I understand that my thesis may be made electronically available to the public.

Abstract

To combat greenhouse gas emissions and improve fuel economy, automotive manufacturers have searched for methods to reduce vehicle weight. As such, hot stamping has become an increasingly popular sheet metal forming technique, due to its ability to produce exceedingly strong parts that can downgauged while maintaining sufficient strength to protect passengers in the event of a collision. In this process, steel blanks are heated in a roller hearth furnace to approximately 930°C to austenitize the grain structure before they are automatically transferred to a die where they are simultaneously quenched and formed into the final part shape. Rapid cooling converts austenitic grains to martensite, achieving ultimate tensile strength values greater than 1500 MPa.

The blanks are often coated with a protective aluminum-silicon (Al-Si) layer to prevent oxidization and decarburization at elevated temperatures. However, the coating melts around 577°C and undergoes a temporary liquid phase before iron-rich intermetallics diffuse from the base steel and solidify the coating. The molten aluminum can pollute and degrade the furnace rollers, leading to their failure. The state change also dramatically alters the radiative properties of the blanks, complicating thermal modelling attempts. Furnace operators have attempted to minimize the impact of coating liquefication through trial-and-error adjustments to the heating parameters of the blanks, but without a clear understanding of the transformation behaviour of the coating, these attempts fail to attain an optimal solution.

This work documents several measurement techniques employed to characterize the evolution of the Al-Si coating during heating. *In-situ* laser-based reflectance measurements

revealed that the liquefication of the coating is comprised of multiple reaction steps at different temperatures. An expansion of this technique captured time-resolved roughness profiles of the blanks, and a quantitative assessment of coating transformation was acquired. *Ex-situ* spectral reflectance and *in-situ* spectral emittance measurements were also performed to correlate changes in radiative properties to the developmental stages of the coating. Additionally, inflection points in the radiative spectra were linked to the morphology of an oxide layer or the diffusion of intermetallic compounds. Finally, the chemical evolution of the surface was captured through Raman spectroscopy measurements, documenting the Raman spectra of several intermetallic compounds unpublished in literature. These results expand the knowledge base on the Al-Si coating, benefitting hot stamping practitioners and furnace operators alike.

Acknowledgements

I would like to begin by thanking my supervisor, Dr. Kyle Daun. I have been incredibly fortunate to spend the past few years working with such a brilliant researcher, leader, and motivator. You have made my graduate experience 100 times better with your unrivaled enthusiasm. You go above and beyond and care deeply for your students and their well-being. I owe a large part of any success that I might have, present and future, to you. I am happy that I did not burn down your lab with one of my experiments.

I would also like to thank some of the fellow researchers with whom I have had the privilege of working. Dr. Rodney Smith – bringing in your expertise was one of the better things to happen with this project. I admire your intelligence and problem-solving ability. The description of a "successful researcher" that you have on the door to your lab describes you perfectly. I am also thankful that I did not burn down your lab with one of my experiments. Jixi Zhang – you have been a wonderful addition to this project, I wish you all the best as you continue! I know you will do great. Intelligence and strong work ethic travel far. Dr. Johannes Emmert – you are a genius. How you can understand so many complicated scientific concepts and explain them succinctly (in a second language no less) to someone who knew nothing about them is baffling to me. Congratulations on your doctorate and whatever comes next. From Cosma: Eric, Eddy, Alex, Jason, Cangji – thank you gentlemen for keeping this project grounded and relevant, we always appreciated your recommendations and insight into the practical side of things. I am also grateful to Dr. Nina Heinig, Dr. Maedeh Pourmajidian, Dr. Yuquan Ding, Dr. Kaihsiang Lin, Mr. Neil Griffett, Mr. Mark

Whitney, and Mr. Roger Tsang for their tremendous help with all things SEM, roughness, circuitry, wiring, programming, etc. Thank you for being so generous with your time.

Furthermore, I would like to acknowledge my fellow members of WatLIT, past and present: Boxuan (Tom), Arpan, Fatima, Kaihsiang, Nishant, Rodrigo, Michael, Paule, Stephen, Stanislav (Stas), Sina, Daniel, Ned, Roger, and Mohit. It has been wonderful sharing a research space with such incredibly bright and nice people. I certainly would not have survived the trials known as inverse and radiation without the constant help of some of you. I always appreciated your friendly faces in the lab and during meetings and games nights. I wish you all success for wherever life takes you as you finish your studies at the university or begin/continue your professional careers. I hope our paths cross again someday.

To my undergraduate classmates, Amanda, Kyle, Lauren, Lukas, MacGregor, and Spencer, an enormous thank you. I truly do not know how I would have graduated without your help. Now, I can look back on all those long days and late nights and smile, as I hope you can too. Thank you for making my university degree more than just a piece of paper. It was wonderful tackling one of the most challenging things in my life with some of my very best friends. The next paragraph applies to you too.

I can’t forget some of the other great Waterloo friends with whom I did not share a classroom: Abby, Ben, Connor, Isaac, Kyra, Leah, Olivia, Rebecca, and Stefan. While I hate moving and having to make new friends, I am truly blessed to have met a group of such amazing people. Some of the very best memories in my life come from the trips we took, games we made up, and conversations late into the night that we shared. I have learned so

much from all of you. Although we may be spread far apart in different cities now, I can't wait for the events that Rebecca will plan to get us back together when we are old geezers.

To my wonderful family: Marv, Annette, Paul, Darren, Julianne, Oscar, and ??. Thank you for your constant love and support through these long years of school away from home. Thank you for checking in on me, pretending to be interested in all of the boring math and science, and cheering me on during the peaks and being there for me in the valleys. The assurance that there is always a clean bed and warm meal awaiting me when I get home is a true blessing. Wherever my life takes me, I pray it is not far from each of you.

To my wonderful (second) family: Dave, Heidi, Andrew, Brian, Tom, and Carolyn. It is safe to say that we have gotten to know each other a bit better these past few years. I am so grateful for your generosity and love, letting Leah and I stay with you for extended periods of time when the world was falling apart. I don't think "in-law," you are all true family.

To my amazing, beautiful wife, my sagwa, my vanilla bean, thank you. Leah, meeting you was the best thing to ever happen to me. You continually inspire me to become a better husband and person, and your support has been second-to-none. I cannot imagine doing life without you, especially these past two years. Thank you for always being my cheerleader and encouraging me to step out of my comfort zone. To the years ahead. I love you.

Finally, I thank God for the rich blessings He has given me. To Him be the glory.

Table of Contents

List of Figures

List of Tables

Chapter 1

Hot Stamping of Al-Si coated 22MnB5 Steel

This chapter provides a fundamental background on the automotive sheet metal forming technique known as hot stamping. The use of aluminum-silicon (Al-Si) coatings as a preventative method against oxidation and decarburization of the steel blanks during heating is reviewed. Particularly, the melting and resolidification of the Al-Si coating during heating is discussed in detail, with the resultant issues incurred by industrial practitioners serving as the motivation for this work. The chapter concludes with an outline of the thesis structure.

1.1 Introduction to Hot Stamping

In recent decades, automotive manufacturers have employed various lightweighting practices to mitigate emissions and improve the fuel economy of their vehicles [1]. Hot stamping of Al-Si coated 22MnB5 steel has become a popular sheet metal forming technique, as it can produce light and crashworthy vehicle components, yielding an ultimate tensile strength of up to 1500 MPa [2]. The elemental composition of 22MnB5 steel can be seen in Table 1-1 [3]. Key alloying elements such as carbon (C), manganese (Mn), and boron (B) increase the strength and hardness of the steel and allow a martensitic microstructure to form upon quenching [4].

Table 1-1: Composition of alloying elements and impurities of 22MnB5 steel [3].

Element	C	Si	Mn	P	S	Al	Ti	Nb	Cu	B	Cr	Fe
Max. wt.%	0.25	0.4	1.4	0.03	0.01	0.1	0.05	0.01	0.2	0.005	0.35	Bal.

1.1.1 Phase Transformation During Heating

A representation of the direct hot stamping method can be seen in Figure 1-1 [2]. Steel blanks are first heated to approximately 930°C and austenitized in a furnace, before being transferred to a die where they are simultaneously formed and quenched, creating the final part geometry and dramatically increasing the strength and toughness of the steel [5]. Roller hearth furnaces 30-40 m long are typically used to heat unformed parts, with rollers to transmit the blanks and several temperature-independent zones to control the heating rate of the steel [6].

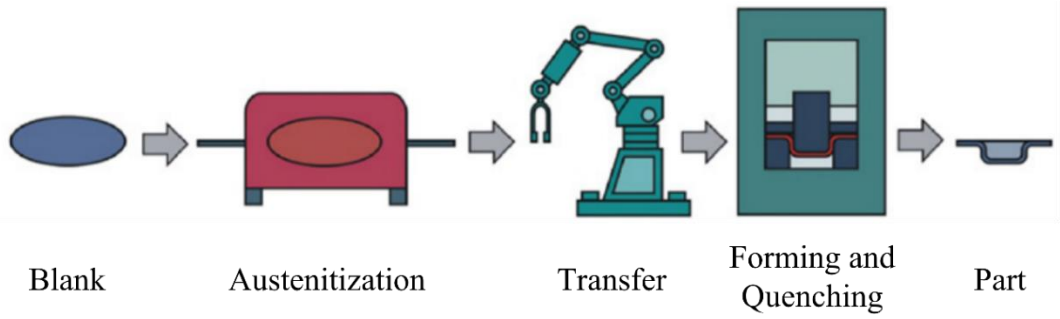

Figure 1-1: Schematic of the direct hot stamping process, adapted from Karbasian and Tekkaya [2].

In the as-received state, 22MnB5 steel consists of ferrite (α) and pearlite (θ) grains, as seen in the Fe-C phase diagram in Figure 1-2 [7]. At elevated temperatures, the initial grain structure transforms into austenite (γ) grains between the austenitization onset and completion temperatures, T_{Ac1} and T_{Ac3}, respectively.

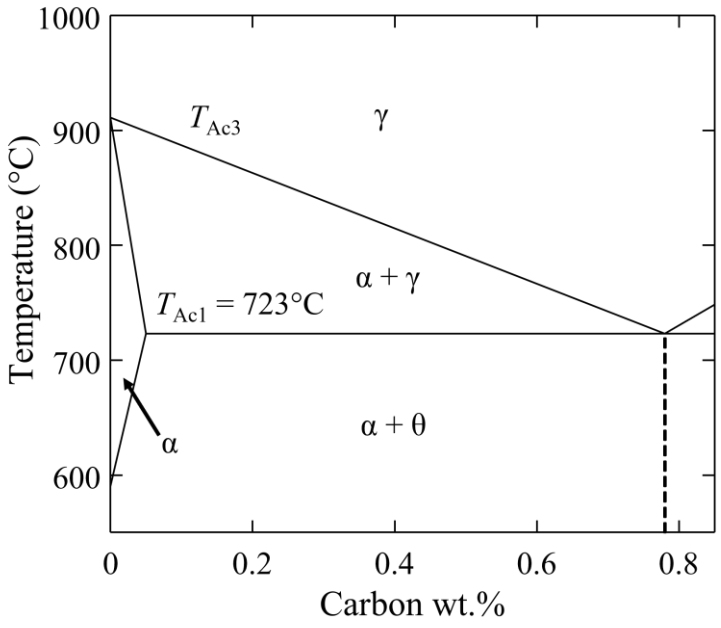

Figure 1-2: Fe-C phase diagram, adapted from Freudenberger et al. [7].

The austenitic structure is then converted to a martensitic (M) structure upon quenching in the forming die [5]. To avoid undesirable transitions to ferrite, pearlite, or bainite (B) during quenching, the blanks must be cooled at approximately $25°C \cdot s^{-1}$ or faster, as seen in Figure 1-3 [8]. The microstructure of as-received and heat-treated blanks can be seen in Figure 1-4 [9], revealing pearlite, ferrite, and martensite grains.

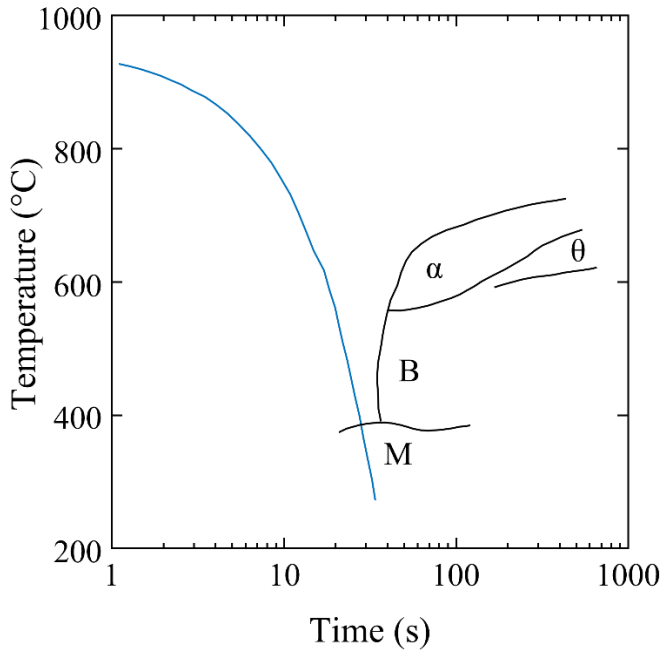

Figure 1-3: Critical cooling curve for 22MnB5 steel, adapted from Zhang et al. [8].

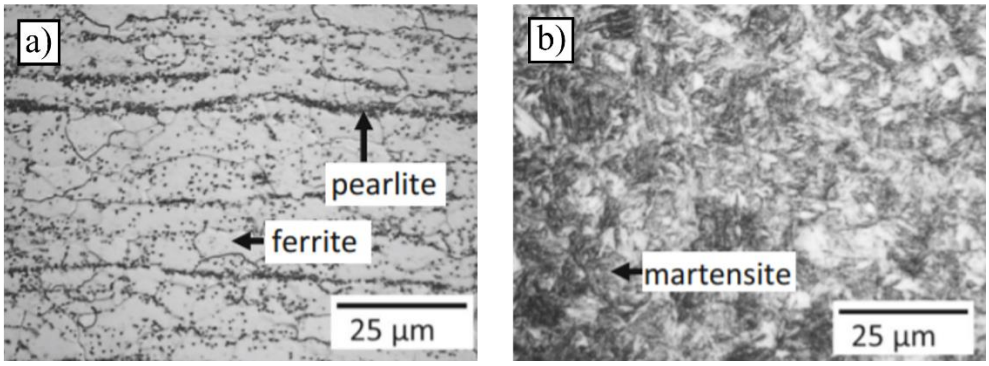

Figure 1-4: Steel microstructure a) before and b) after heat treatment, from Di Ciano et al. [9]. Ferrite, pearlite, and martensite grains can be identified.

1.1.2 Use of Al-Si Coatings

To protect against oxidation and decarburization of the steel while heating, blanks are coated with an aluminum-silicon (Al-Si) layer (typically 90-10 wt.% [10]) applied through a hot dipping process [11]. The Al-Si coating in its as-received state can be seen in Figure 1-5,

which shows a scanning electron microscope (SEM) image with specific intermetallic and oxide compounds documented with the use of energy-dispersive x-ray spectroscopy (EDS) measurements. The most common coating weight utilized in production is 150 g/m^2 (AS150, ~25 μm thick), but a weight of 80 g/m^2 (AS80, ~14 μm thick) is also utilized in some hot stamping applications, with the intention of lowering production costs given the reduced coating material. Structural and mechanistic information for the most common intermetallic compounds detected in the coating during heating is given in Table 1-2. The addition of silicon causes a continuous intermetallic layer comprised of mainly τ_5 to form between the coating and the base steel [12, 13]. An extremely thin intermetallic layer separates the τ_5 strip and the base steel, which has been reported to be different combinations of intermetallic phases (η and θ [11, 14], η and τ_1 [15], or η, θ, and τ_1 [16, 17]). Distinct ternary intermetallic compounds such as τ_5 and τ_6 and some iron oxides can be detected at the surface of the coating prior to heat treatment, perhaps due to the tendency of Al-Fe-Si intermetallics to nucleate on the underside of an oxide layer formed on molten Al-Si [18]. Small Si and Fe aggregates are also present throughout the coating after the hot-dipping process.

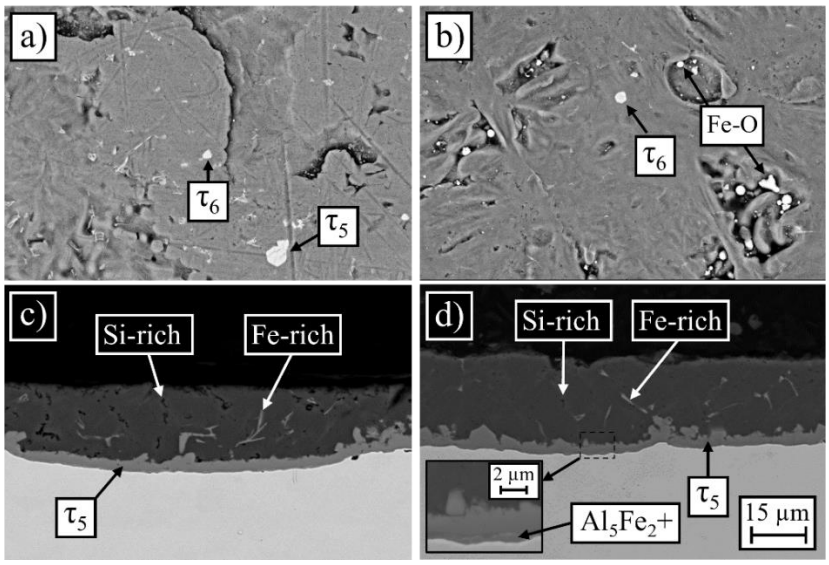

Figure 1-5: Top view SEM images for as-received a) AS80 and b) AS150 coupons; and cross-sectional SEM images for as-received c) AS80 and d) AS150 coupons at 750x magnification.

Table 1-2: Structural and mechanistic data for common intermetallic compounds present in the Al-Si coating before and after heat treatment.

Symbol	Composition	Space Group	Reference
τ_1	$Al_2Fe_3Si_3$ ($Al_3Fe_3Si_2$)	P1	[19, 20]
τ_2	Al_3FeSi	-	[19]
τ_5	$Al_{7.4}Fe_2Si$ (Al_7Fe_2Si)	$P6_3/mmc$	[19, 21]
τ_6	$Al_{4.5}FeSi$	A2/a	[19, 22]
θ	Al_3Fe ($Al_{13}Fe_4$)	C2/m	[23, 24]
η	Al_5Fe_2	Cmcm	[23, 25]
ζ	Al_2Fe	P1	[23, 26]

In typical hot stamping operations, the Al-Si coating will melt at approximately 577°C, as seen in Figure 1-6 [27]. Some researchers [28] suggest that the liquefication of the Al-Si coating can be avoided altogether by heating the steel below a critical rate, which would allow the coating to transform into intermetallics below the Al-Si melting point. This is unlikely to be the case, however, since diffusion of iron from the substrate 22MnB5 steel into

the coating is minimal at temperatures below the Al-Si melting temperature. Grauer et al. carried out differential scanning calorimetry analysis on Al-Si coated 22MnB5 coupons heated at rates as low as 0.08 K/s (far lower than what would be practical in an industrial setting) and showed that the endothermic phase transformation associated with coating liquefication always occurs [29], thereby disproving this hypothesis.

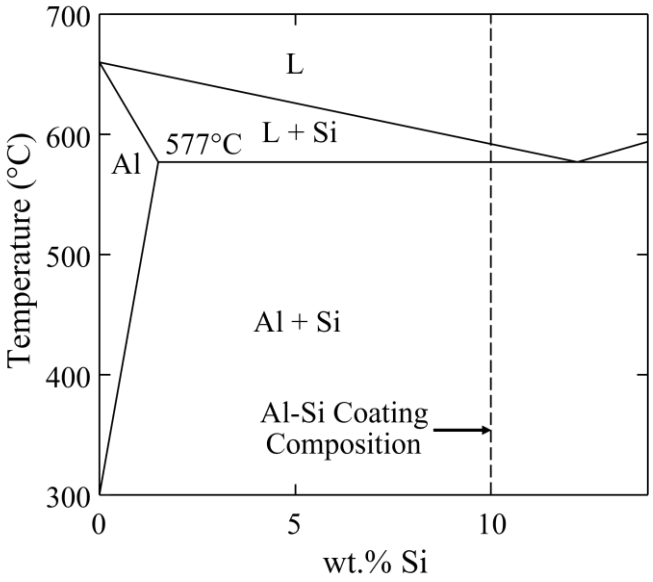

Figure 1-6: Al-Si phase diagram, adapted from Murray and McAlister [27].

Figure 1-7 shows a sample heating curve of the coated steel at a furnace setpoint of 950°C, along with the temperature derivative calculated by first-order central finite differences. The coating melting temperature corresponds to a sharp drop in the heating rate of the sample due to the corresponding drop in absorptance, which reduces the rate of heat transfer from the furnace to the coupon. The austenitization start (T_{Ac1}) and completion (T_{Ac3}) temperatures are also visible through inflection points in the temperature derivative, consistent with the findings of Jhajj et al [30].

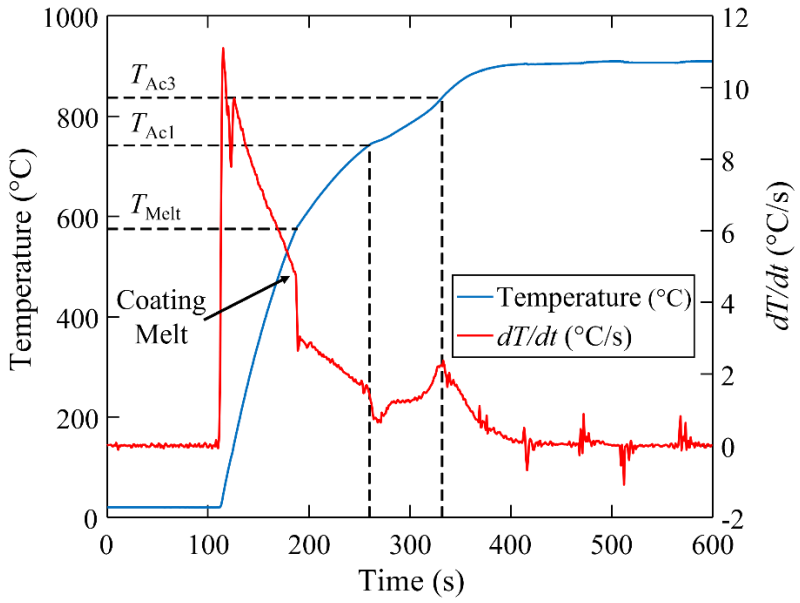

Figure 1-7: Coupon heating curve for a furnace setpoint of 950°C.

After melting, iron from the steel substrate rapidly diffuses into the liquid and creates a solid layer containing several intermetallic aluminum-iron-silicon (Al-Fe-Si) and aluminum-iron (Al-Fe) sublayers, as seen in Figure 1-8. It is important to characterize the final dispersion of intermetallic phases within the coating, as they affect the overall formability and crack-resistance of the coating [31, 32] as well as its weldability [33, 34]. A fully developed intermetallic Al-Fe-Si layer is known to provide long-term corrosion resistance [35, 36]. Iron diffusion through the Al-Si coating during heating has been studied extensively in literature, mainly through *ex-situ* characterization techniques on cross-sectioned samples. When heated to approximately 900°C, the primary intermetallic layer that progresses through the molten coating has often been identified as τ_5, followed by iron-rich layers such as θ, η, and ζ [14, 37]. Solid state iron enrichment continues even after the coating has been completely solidified as a mixture of intermetallics, leading to discrepancies in the phases

reported in the final coating obtained after heat treatment. Such discrepancies may also be attributable to differences in the heating conditions of the hot stamping blanks. Grigorieva et al. [14] and Jenner et al. [38] report that the final coating consists of alternating τ_1 and η layers, while Kolaříková et al. identified these compounds as well as AlFe layers for longer dwell times [16]. On the other hand, Fan and De Cooman [11] and Liang et al. [17] documented alternating τ_1 and ζ layers.

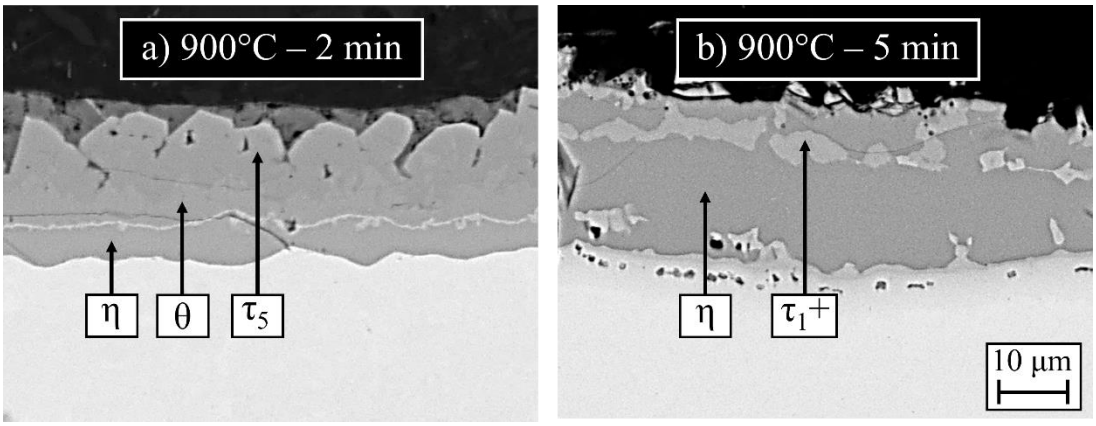

Figure 1-8: Evolution of the Al-Si coating when heated at 900°C for a) 2 min and b) 5 min.

The coating evolution is further complicated by surface oxidation during heating, and a comprehensive review regarding the oxidation of Al-Si coated blanks is largely absent in literature. The coatings have a native Al_2O_3 layer that is approximately 10 nm thick in their as-received state [39]. Classified as the α-Al_2O_3 phase [40], the oxide grows slightly at elevated temperatures and prevents widescale oxidation of the Al-Si coating and the base steel [11, 41]. Fan et al. reported two oxidation stages during heating: a lower temperature reaction in which the aluminum combines with oxygen in the atmosphere, and a higher temperature reaction in which water vapor decomposes on the surface to form Al_2O_3 and H_2

[42]. In addition to aluminum oxide, iron-rich [43] and silicon-rich [44] oxides have also been identified at the surface of hot stamping blanks. However, these findings are limited as they do not directly consider the effect of coating liquefication during oxidation.

1.2 Research Motivation

Despite the protective benefits of the Al-Si coating, its melting causes significant issues and inefficiencies in the production of hot stamping blanks. Molten aluminum can penetrate into and degrade the ceramic furnace rollers [45], an extreme case of which is shown in Figure 1-9. The polluted rollers need to be cleaned, leading to furnace downtime and decreased throughput, or they can break and need to be replaced [46]. Molten aluminum at the surface of the blanks and coating buildup on the rollers can also cause the parts to slide and relocate atop the rollers, complicating their automated transfer from the furnace.

Figure 1-9: Failed furnace rollers covered with aluminum contamination from the Al-Si coating.

Industrial practitioners have noted that the degree of coating transfer often depends on the parameters used to heat the blanks. Accordingly, furnace operators heuristically adjust the temperature of the zones within the furnace to minimize the damage incurred by the rollers. Unfortunately, current literature typically focuses on the diffusion of intermetallic compounds that solidify the coating, and not on the melting of the coating and its behaviour in the molten state. Without a clear understanding of the underlying phenomena, heating strategies attempting to reduce roller contamination amount to a suboptimal trade-off between avoiding coating liquefication issues and overall throughput.

It is possible that preventing roller contamination is linked to the formation of a robust oxide layer, which would act as a protective boundary between the molten coating and the rollers [47]. Conceivably, certain heating rates employed by furnace operators generate an oxide layer that is resilient to the melting of the coating. Nevertheless, Al-Si coating oxidation and its potential to protect the rollers is not extensively documented in literature.

Moreover, the evolving surface state leads to substantial changes in the radiative properties of the blanks, as seen in Figure 1-10 [30], and consequently, their heating profile in the furnace [6]. Accurate estimates of the radiative properties are vital to thermal models predicting the temperature profile of the parts, which balance complete austenitization of the steel and short cycle times. However, it is difficult to measure the radiative properties of the blanks *in-situ*, and the applicability of *ex-situ* measurements on samples removed from the furnace and quenched is weakened due to the temperature dependence of the radiative properties and the possible state changes undergone by the coating upon cooling.

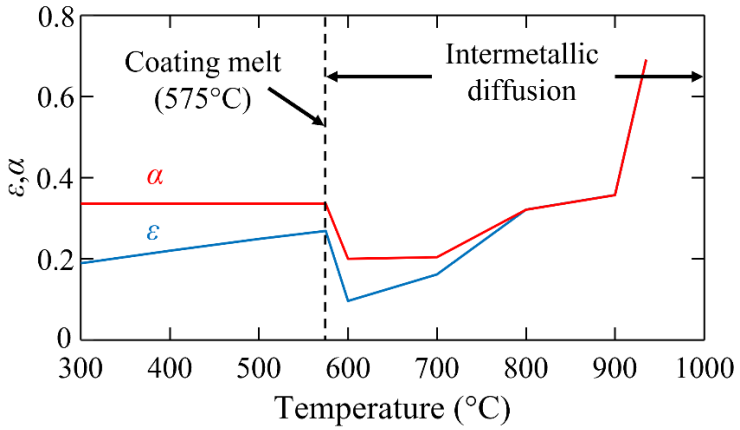

Figure 1-10: Total absorptance (α) and emittance (ε) of Al-Si coated blanks during heating, adapted from Jhajj et al. [30].

Therefore, *in-situ* measurement techniques are needed to expand the knowledge base on the melting and intermetallic development of the Al-Si coating, its oxidation, and the effect of these processes on the radiative properties of the hot stamping blanks.

1.3 Overview of Thesis

This work analyzes the evolution of the Al-Si coating in four additional sections. Relevant theory and background necessary to understand the content of subsequent chapters will be provided therein.

Chapter 2 introduces a laser-based reflectance measurement technique to infer state changes within the coating during heating. These measurements are compared to *ex-situ* reflectance measurements which show the development of an oxide layer and intermetallic diffusion through the presence of characteristic peaks. These tests are combined with SEM-EDS measurements to assess the intermetallic development of the coating and the characteristics of the oxide layer that forms at its surface.

Chapter 3 expands upon the laser-reflectance measurements in Chapter 2 by correlating the scattering of the reflected light to the roughness of the surface. The roughness measurement method and SEM-EDS analysis are applied to hot stamping blanks of two different coating weights to assess differences during the development of the coating caused by its thickness. *In-situ* emittance tests were also performed to investigate how the radiative properties changed at high temperatures and with the evolution of the coating.

Chapter 4 uses Raman spectroscopy to refine mechanistic understanding on the structural evolution of the Al-Si coating. *In-situ* videos of the transforming surface were captured, providing visual confirmation of the state changes detected in Chapter 2 and Chapter 3. *In-situ* Raman spectroscopy demonstrated that state changes were accompanied by different chemical signatures, and unique and unpublished Raman spectra were discovered and linked to intermetallic compounds through SEM-EDS analysis.

Finally, Chapter 5 summarizes the results of this research with recommendations for future work.

1.4 Research Contributors

This section provides the list of researchers who directly contributed to some of the results present in this thesis.

Dr. Kaihsiang Lin is responsible for the SEM-EDS measurements in Section 2.3.1.

Dr. Maedeh Pourmajidian conducted the FIB-SEM experiments in Section 2.3.2.

Dr. Johannes Emmert aided in the construction of the setup to acquire the speckle patterns and co-authored the MATLAB® code to process the results in Section 3.3.1.

Dr. Nina Heinig performed the SEM-EDS analysis in Section 3.3.2 and Section 4.3.3.

Finally, Dr. Rodney Smith and Ms. Yutong Liu made the α-Fe_2O_3 sample used in Section 4.3.3.

Chapter 2

In-situ and *Ex-situ* Reflectance Measurements

To better understand the evolution of the Al-Si coating on 22MnB5 steel and its impact on industrial practices, laser-based *in-situ* reflectance tests were performed on samples heated within a muffle furnace in order to infer the surface state of the coating with respect to time and temperature. SEM images coupled with EDS analysis performed on samples extracted at different heating durations correlated changes in the *in-situ* reflectance with intermetallic development and oxide formation. While these measurements provide a highly resolved estimate of when the coating liquefies and resolidifies, additional information on the morphology and chemistry of the surface can be attained through spectral reflectance measurements over a wide wavelength range. Accordingly, *ex-situ* reflectance measurements captured using a Fourier-transform infrared spectrometer were compared to high-magnification SEM images to assess the structure of the oxide layer on samples subjected to a variety of heat treatment protocols and removed from the furnace and quenched. This chapter is comprised of content from a published journal article [48] and an accepted conference paper [49].

2.1 Theory

2.1.1 Evolution of the Al-Si Coating Surface

The formation and evolution of intermetallic phases after the Al-Si layer melts can be separated into two main processes: the growth of intermetallic compounds from the base steel and their progression through the Al-Si coating as documented in Chapter 1; and the

transformation of intermetallic compounds at the surface of the coating, which has significant implications for roller hearth furnace operations and will be expanded upon herein.

Grigorieva et al. [14] attributed the initial melting of the coating to reaction (1)

$$577°C: Al + Si + \tau_6 \rightarrow L \quad (1)$$

based on the Al-Si [27] and Al-Fe-Si [50] phase diagrams and electron microscopy measurements on samples removed from a furnace at intermittent dwell times. However, it appears that the liquefication of the coating cannot be defined by this single reaction. For instance, differential scanning calorimetry experiments by Grauer et al. identified the melting reaction at 577°C, plus additional reactions between 625°C and 675°C [29]. Grigorieva et al. [14] hypothesized that the τ_5 sublayer separating the initial coating and substrate becomes enriched with aluminum during austenitization, causing θ nucleation according to reaction (2)

$$620°C: Al + \tau_5 \rightarrow \theta + L \quad (2)$$

which could also affect the localized τ_5 compounds at the surface of the coating. Barreau et al. [39] used a scanning electron microscope (SEM) equipped with a heating stage to visualize specific melting reactions occurring at the surface during heating. This approach revealed that reaction (1) was followed by alternative reaction steps that occur below the temperature for reaction (2). They proposed the existence of the reaction step described by reaction (3)

$$615°C: Al + \tau_6 \rightarrow \tau_5 + L \quad (3)$$

Barreau et al. [39] also noticed dissolution of the surface taking place between 650°C and 690°C, attributing it to reaction (4)

$$655°C: Al + \theta \rightarrow L \quad (4)$$

Finally, both Barreau et al. [39] and Grigorieva et al. [14] proposed that at higher temperatures, any remaining τ_5 compounds become further enriched with iron to produce τ_2 and θ according to reaction (5)

$$855°C: \tau_5 \rightarrow \tau_2 + \theta + L \quad (5)$$

Barreau et al. also indicated that reactions (4) and (5) occur at higher temperatures when higher heating rates are utilized [39], indicating that the heating parameters of the blanks must be considered as well.

These analyses show that the transformation of the coating involves a complex network of several reaction steps and intermediate phases, but their relevance is limited due to the implementation of *ex-situ* analysis techniques or dissimilar heating methods compared to industry practices. The need for assessing the development of the coating *in-situ* with industrially relevant heating methods will be addressed by linking phase changes within the coating to changes in the radiative properties, specifically reflectance, of the blanks.

2.1.2 Radiative Properties

Spectral reflectance, ρ_λ, and spectral absorptance, α_λ, define the fraction of incident radiation over a hemisphere and at a given wavelength that a surface reflects and absorbs, respectively.

In the context of hot stamping, these properties dictate how efficiently blanks can absorb heat within the furnace and play a critical role in thermal models [6, 30].

The theoretical reflectance at normal incidence, $\rho_{\lambda,n}$, of a smooth aluminum surface as seen in Figure 2-1 can be calculated using its refractive index, n, and extinction coefficient, k [51] according to equation (6) [52]

$$\rho_{\lambda,n}=\frac{(n-1)^2+k^2}{(n+1)^2+k^2} \quad (6)$$

A significant drop in the spectral reflectance can be seen at approximately 0.83 µm near an inflection point in the refractive indices, which is caused by a transition between pairs of parallel absorption bands [53], before increasing at longer wavelengths as the surface becomes optically smooth.

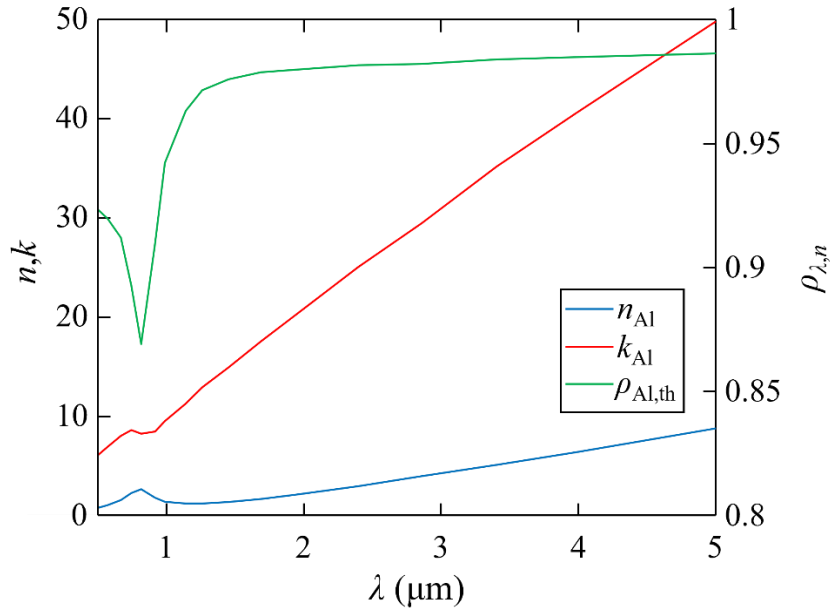

Figure 2-1: Theoretical reflectance for pure aluminum calculated using Eq. (6) [52] and its refractive indices [51].

However, the radiative properties of a surface depend on several factors, including temperature, surface roughness, and degree of oxidation [52]. Radiative properties also depend on direction, as smooth surfaces reflect radiation in a specular manner while radiation reflected by rough (or diffuse) surfaces is more evenly distributed over a hemisphere [52].

The presence of an oxide generally leads to rougher and less reflective surfaces, but can also cause significant inflection points in the radiative properties of a surface due to the thin film-interference effect [52], as shown in Figure 2-2. Incident radiation, I_a, on an oxidized surface with thickness, D, will refract through the oxide at an altered frequency, I_f. As the radiation reflects off the aluminum substrate and travels towards the oxide surface, it will constructively or destructively interfere with incident radiation, effectively increasing or decreasing the intensity of the reflected radiation at certain wavelengths, I_i. This effect occurs when the wavelength is much larger than the oxide film thickness ($\lambda \sim 100D$) [54]. Some studies [55-57] have exploited this effect and have inferred the thickness of the oxide layer through the location of interference maxima and minima and the refractive indices of the oxide [58].

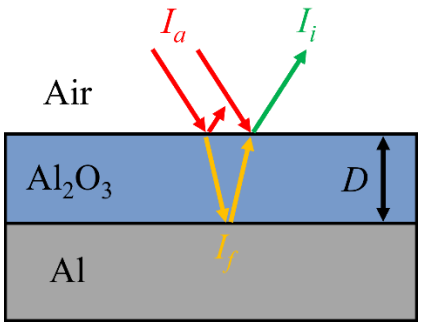

Figure 2-2: Film-interference schematic.

Because ρ_λ depends on the roughness and degree of oxidation of the surface, *in-situ* measurements of the reflectance of hot stamping samples would indicate sudden state changes as the coating undergoes the melting reactions (1-5) and resolidifies. Several researchers have linked changes in radiative properties to the evolving surface state of samples, such as Makino et al. [59] and Yu et al. [60], who inferred the oxidation of metal samples using spectral reflectance and emittance measurements, respectively. Jones and Richards performed reflectance measurements on aluminum coated steel and found that peaks in the reflectance signal corresponded to oxidation and phase changes within the coating [61].

In the context of hot stamping samples, Shi et al. performed *in-situ* and *ex-situ* spectral emittance measurements on Al-Si coated samples heated in a Gleeble® thermomechanical simulator [30, 62]. They found that the initial radiative properties resembled a roughened aluminum surface with increasing spectral reflectance as the wavelength increased, before becoming highly reflective and specular once the coating melted. The surface then roughened as it transformed into an intermetallic coating due to iron diffusion and oxidation. However, the validity of these results is questioned as the resistive heating method introduced visible surface artifacts into the coating between the electrodes. Thus, in addition to ensuring the radiative properties are measured *in-situ*, the proposed experiments will use heating conditions similar to industrial practices.

2.2 Experimental Methods

2.2.1 *In-situ* Reflectance Measurements

To conduct *in-situ* reflectance experiments, an apparatus was constructed around a laboratory-scale muffle furnace, as seen in Figure 2-3. Light from a green laser diode with a wavelength of 520 nm (Thorlabs® CPS 520) was directed using a mirror through the exhaust port of the furnace onto the samples at near-normal incidence. The reflected light was directed via a second mirror into a photodiode (PD, Thorlabs® SM05PD1A) which converted the light intensity into a voltage signal. Because the second mirror images most of the light leaving the exhaust port that has been reflected off the samples, the PD signal is comprised of light reflected in the specular and near-specular directions. To improve the signal-to-noise ratio of the photodiode measurement, the laser light was modulated using an optical chopper wheel rotating at 110 Hz and fed from the photodiode into a lock-in amplifier (LIA, Scitec® 410). Finally, the LIA output signal was recorded using a National Instruments® NI USB-6009 data acquisition (DAQ) unit and expressed either in Volts or normalized relative to a maximum value.

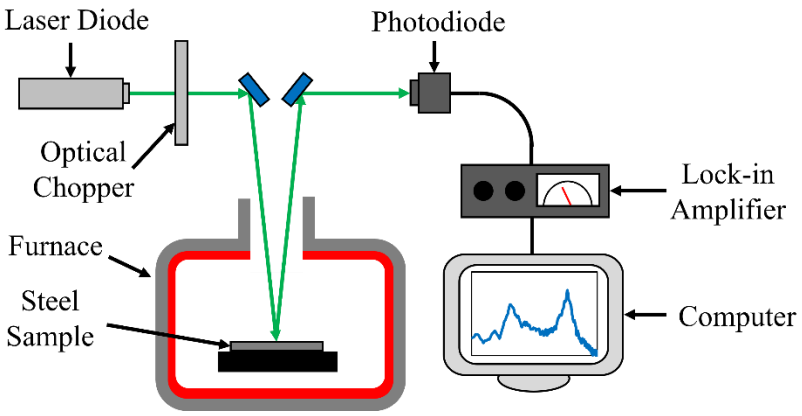

Figure 2-3: *In-situ* reflectance analysis schematic.

Samples consisted of 25 mm x 25 mm x 2.0 mm coupons cut from a Usibor® 1500-AS150 [3, 10] sheet and heated at setpoints between 600°C and 950°C. To ensure the furnace had reached its steady-state temperature, it was soaked for at least 5 min before testing. Samples heated at the 600°C, 750°C, and 950°C setpoints were instrumented with K-type thermocouples to collect temperature data. Additional samples were also heated to 600°C, 700°C, and 800°C, quenched with nitrogen gas, and analyzed *ex-situ*. The near-normal hemispherical reflectance ($\rho_{\lambda,d\text{-}h}$) of the samples heated to 700°C was measured with a Varian Cary 600 UV-Vis-NIR spectrophotometer equipped with an integrating sphere (250-800 nm) and compared with the photodiode measurements. The samples extracted at the 600°C and 800°C setpoints were analyzed using scanning electron microscopy and energy-dispersive X-ray spectroscopy to assess the degree of intermetallic diffusion and oxidation with respect to the changes in reflectance measured with the photodiode.

2.2.2 *Ex-situ* Reflectance Measurements and Oxide Characterization

The *ex-situ* reflectance measurements were collected using a Bruker® Invenio X FTIR spectrometer. Integrating spheres constructed out of Spectralon® and Infragold® materials were used to measure 0.4-1.1 μm and 1.1-25 μm spectral ranges, respectively. A schematic of the integrating spheres used in these tests can be seen in Figure 2-4. Light from the FTIR is shone through the entrance port of the integrating sphere and directed towards the sample port. The reflected radiation then reflects off the surface of the integrating sphere until it enters the detector port and is absorbed. Reflective baffles, not shown in the schematic, prevent specularly-reflected light from reaching the detector port, yielding a measurement of the hemispherical spectral reflectance of the sample. Si diode and deuterated, L-alanine doped triglycine sulfate (DTGS) detectors were used for the 0.4-1.1 μm and 1.1-25 μm measurement ranges, respectively.

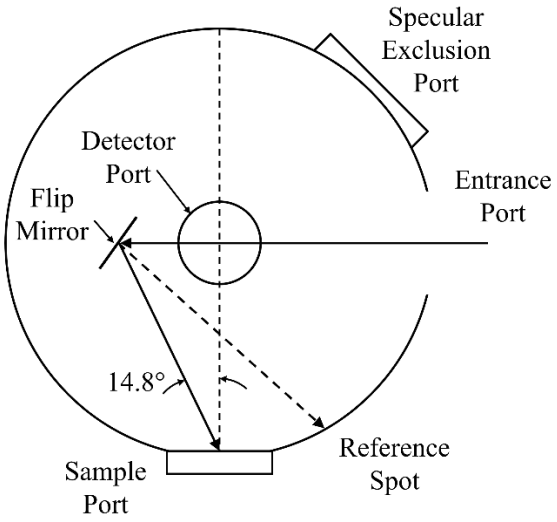

Figure 2-4: Integrating sphere schematic for *ex-situ* reflectance experiments.

However, the integrating spheres do not perfectly reflect all incident radiation, as seen in Figure 2-5, which could bias the results and create gaps between the wavelength measurement ranges. This was accounted for by following the procedure outlined by Blake et al. [63]. To begin, a sample was first placed in the sample port. Then, the instrument reading with the flip mirror pointed at the sample port, V_s, was divided by the measurement acquired when the flip mirror was directed at the reference spot shown in Figure 2-4, $V_{s,ref}$. The sample was then removed and replaced by a Spectralon® or Infragold® standard with spectral reflectances given in Figure 2-5 (ρ_{st}). The previous two measurements were repeated with the standard in place, yielding V_{st} and $V_{st,ref}$. Then, the corrected spectral reflectance, $\rho_{s,corr}$, can be acquired according to

$$\rho_{s,corr} = \frac{V_s / V_{s,ref}}{V_{st} / V_{st,ref}} \rho_{st} \quad (7)$$

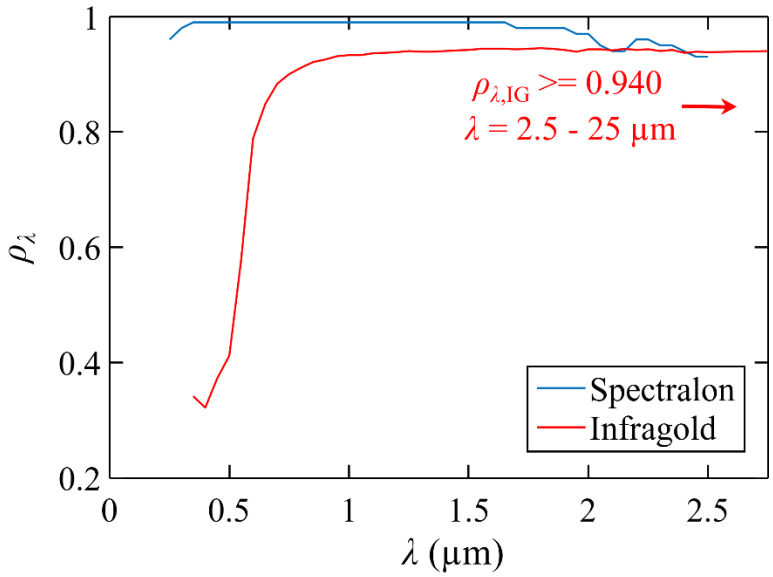

Figure 2-5: Spectral reflectance of Labsphere Spectralon® and Infragold® coatings for the integrating spheres [64]. Spectral reflectance of the Infragold® coating in the near- to mid-infrared is listed as >0.94.

For these tests, 38 mm x 38 mm x 2.0 mm samples were cut from a Usibor® 1500-AS150 [3, 10] sheet and heated in a furnace soaked for five minutes at 900°C for 0 s (as-received), 45 s, 90 s, 150 s, and 300 s. Additional samples were heated for 300 s at 500°C, 600°C, 640°C, 670°C, and 800°C to detect any changes in behaviour around the melting reactions (1-5) of the coating.

Traditional SEM measurements (Figure 1-5) do not show an oxide layer at the surface of the samples, perhaps because it is destroyed in the mounting process. Therefore, after the *ex-situ* reflectance data for these samples had been acquired, they were subjected to SEM analysis according to the procedures described by Pourmajidian et al. [65] to assess the oxide morphology of the samples. Surfaces of samples were analyzed using a JEOL 7000F field

emission gun scanning electron microscope. To acquire cross-sections, a protective layer of tungsten was first applied to the sample surface and then focused ion-beam (FIB, Zeiss® NVision 40 FIB-SEM microscope) trench cuts measuring 10 µm x 10 µm were performed. The thickness of the oxide was measured by drawing bounds on the upper and lower extents of the oxide, and sampling height measurements every 3 nm using MATLAB® software. An example of this process is shown in Figure 2-6. The measured oxide thicknesses given in this work represent the mean of these height samplings, presented with the upper and lower bounds of the 95% confidence interval.

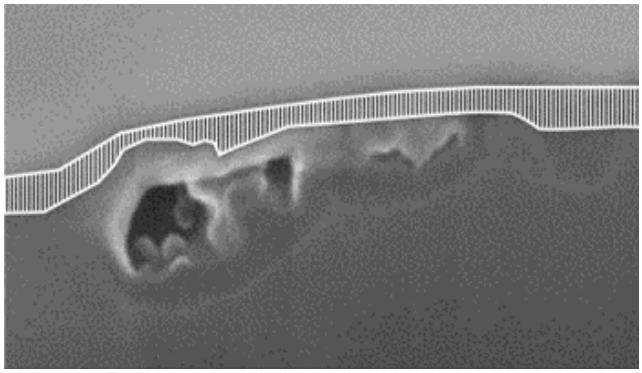

Figure 2-6: Example of the oxide thickness measurement process showing the upper and lower extents of the oxide and the individual height measurements captured by MATLAB®.

2.3 Results

2.3.1 *In-situ* Reflectance Measurements

The *ex-situ* reflectance measurements performed with the spectrophotometer on the subset of samples heated to the 700°C setpoint can be seen in Figure 2-7a. The as-received sample has the spectral reflectance of a moderately rough aluminum surface [66]. With further heating, the spectral reflectance drastically decreases, with the sample heated for 250 s having a low

reflectance characteristic of a fully transformed, rough intermetallic surface. Figure 2-7b compares the near-normal hemispherical reflectance at 520 nm of the samples in Figure 2-7a to the voltage measured by the photodiode at room temperature. Except for sample 4, good agreement and a proportional relationship were found between the two measurement methods. Because the photodiode measures specular reflectance in addition to a portion of the diffuse reflection, this measurement cannot be converted directly to a specular or hemispherical reflectance, but this comparison confirms the ability of the experimental setup to detect relative changes in reflectance.

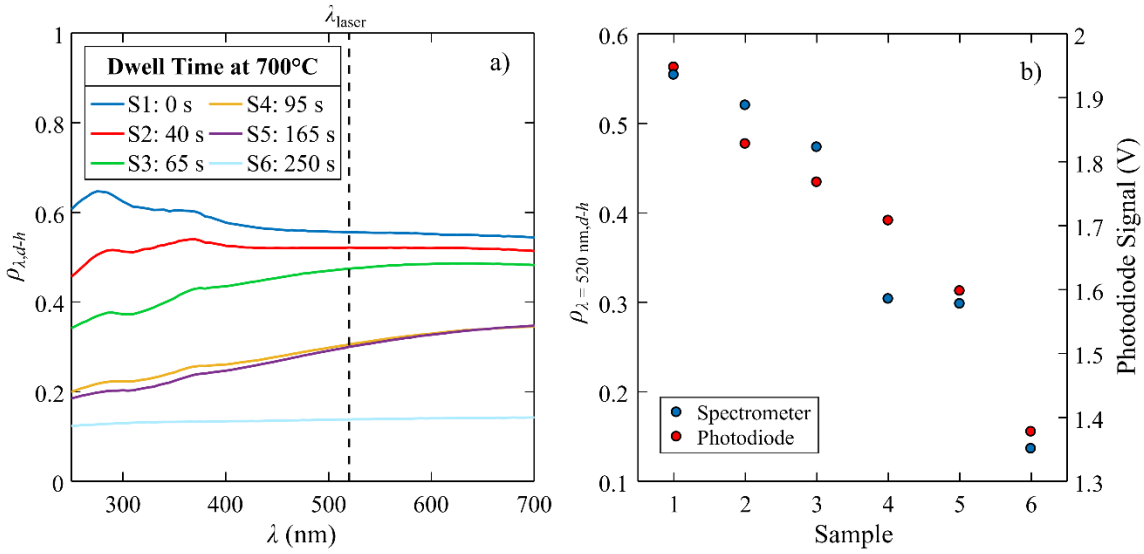

Figure 2-7: Reflectance measurements for samples heated at 700°C for various dwell times using a) a spectrophotometer capturing spectral, near-normal hemispherical reflectance and b) the photodiode setup, which are compared to the spectrophotometry measurements at the wavelength of the laser.

The normalized photodiode signal of a sample heated to 750°C can be seen in Figure 2-8a. The signal remains constant as the temperature of the coupon reaches the melting point of the

coating, ~577°C, where it abruptly increases. Similar to Figure 1-7, an inflection point in the heating rate is detected at this point, indicating that the coating has melted. With further heating, the signal drops rapidly before a secondary peak emerges, after which the signal decreases to its lowest value and does not increase again. To see if this behaviour was consistent with different heating conditions, the effect of furnace setpoint on the photodiode signal was assessed, which can be seen in Figure 2-8b. The two-peak signal is consistent for the sample heated to 950°C, but the sample heated to 600°C only decreases in reflectance after the melting point of the coating is reached. For additional samples heated to 550°C, no change in reflectance behaviour was observed. Additionally, while the peak associated to the onset of coating liquefication remained at a constant temperature, the subsequent peak for the sample heated to 950°C was shifted to a higher temperature compared to the sample heated to 750°C. This indicates that the surface evolution depends on heating rate in addition to the furnace dwell temperature.

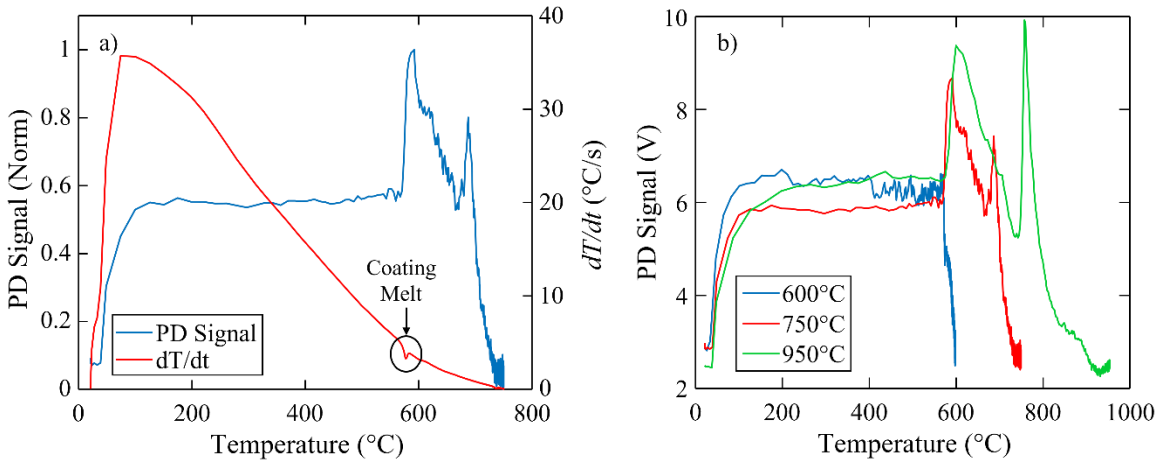

Figure 2-8: a) Normalized photodiode signal and coupon heating rate at a furnace setpoint of 750°C and b) normalized photodiode signal vs. temperature for furnace setpoints of 600°C, 750°C, and 950°C.

While the first reflectance peak corresponds to coating liquefication, it is unclear why the sample heated to 600°C does not exhibit this behaviour. According to the reactions proposed by Barreau et al. [39], it is possible that, corresponding to reaction (1), the coating only undergoes a partial dissolution at 577°C, which allows intermetallic diffusion to occur, but reactions (2) and (3) aid in the creation of a smooth, reflective surface. Additionally, for the samples heated to 750°C and 950°C, the second peak in the photodiode signal occurs near the temperature in reaction (4) given by Barreau et al. [39], indicating its cause is due to an additional melting reaction. Further evidence for these hypotheses will be attained through the SEM-EDS analysis later in this section.

Additional trials were conducted to further illustrate the effect of furnace setpoint and to investigate the repeatability of the experiment. The average of ten independent reflectance measurements were taken at setpoints between 650°C and 950°C; an example of this process

at the 800°C setpoint can be seen in Figure 2-9, showing repeatable results. The mean curves for each setpoint are shown in Figure 2-10. Increasing the furnace setpoint caused the peaks in the signal to occur sooner in the heating process, suggesting that the overall liquid window of the coating could be shortened with higher heating rates.

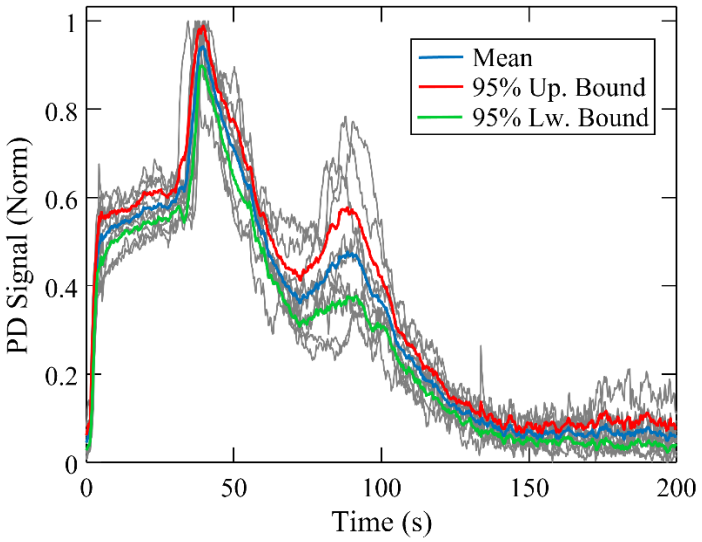

Figure 2-9: Ten normalized photodiode signals for AS150 samples heated at the 800°C setpoint (gray), with the mean and 95% confidence interval.

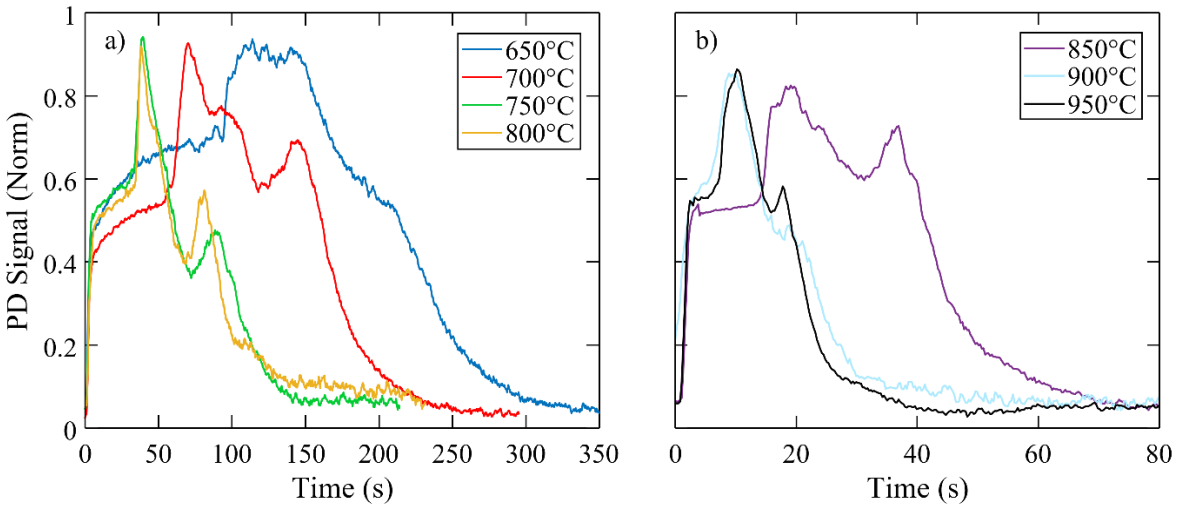

Figure 2-10: Normalized photodiode signals vs. time for furnace setpoints of a) 650°C-800°C and b) 850°C-950°C.

To link the changes in reflectance to intermetallic development within the coating, several samples were removed from the furnace at intermittent dwell times, quenched, and subjected to SEM-EDS analysis. The heating times corresponding to approximate regions in the photodiode signal for setpoints of 600°C and 800°C can be seen in Figure 2-11. The average surface composition measured over a 150 μm x 100 μm area for a single sample can be seen in Table 2-1. Oxygen content increases with further heating in the furnace at both setpoints, but oxide formation occurs more rapidly and to a greater degree at 800°C. Similarly, the percentage of iron at the surface increases for longer dwell times as intermetallic layers diffuse through the coating. This aligns with the results of Shi et al., who showed increasing oxygen and iron content at the surface of the coating as the heating duration was increased [43, 67].

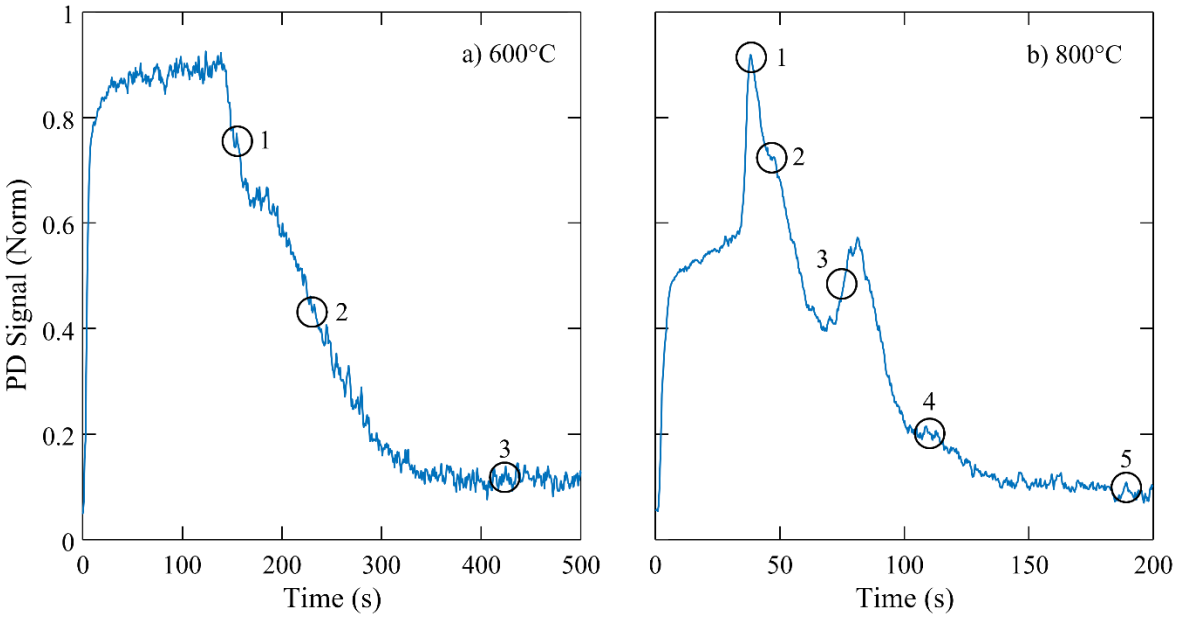

Figure 2-11: Approximate extraction times for *ex-situ* samples at furnace setpoints of a) 600°C and b) 800°C.

Table 2-1: Surface chemical composition by furnace setpoint and dwell time.

Furnace setpoint (°C)	Sample #	Dwell time (s)	Chemical composition (at. %)			
			Al	Fe	Si	O
600	1	150	81.8	0.39	14.4	3.41
	2	210	86.8	1.03	8.37	3.76
	3	420	86.5	2.31	2.46	8.70
800	1	40	86.4	0.57	11.8	1.21
	2	50	84.9	1.01	11.8	2.28
	3	80	77.6	0.70	11.4	10.3
	4	100	80.3	0.75	11.4	7.61
	5	180	78.1	1.38	10.2	10.3

Backscattered SEM images of the sample surfaces can be seen in Figure 2-12, with phases identified through the EDS measurements. At these setpoints, the Al-Si coating with small Si aggregates was permeated by τ_5 or τ_6 compounds as the soak time increased. Borsetto et al.

documented small Si-rich compounds in the Al-Si coating that disappeared with further heat treatment [68]. Moreover, Grigorieva et al. [14] and Barreau et al. [39] reported isolated τ_6 compounds before and in the early stages of heat treatment. Between Figure 2-12e and f, there does appear to be a smoothening of the surface state, which corresponds with the onset of the second peak in the photodiode signal. Oxygen-rich phases were detected in Figure 2-12h, which aligns with the results of Shi et al., who found aluminum and iron oxides after heat treatment [43, 67]. Higher dwell temperatures enhance iron diffusion through the coating, accelerating phase transformation and overall coating evolution [31]. A combination of oxidation and intermetallic diffusion significantly roughens the surface, corresponding to the low reflectance at the end of heat treatment measured in the photodiode experiments.

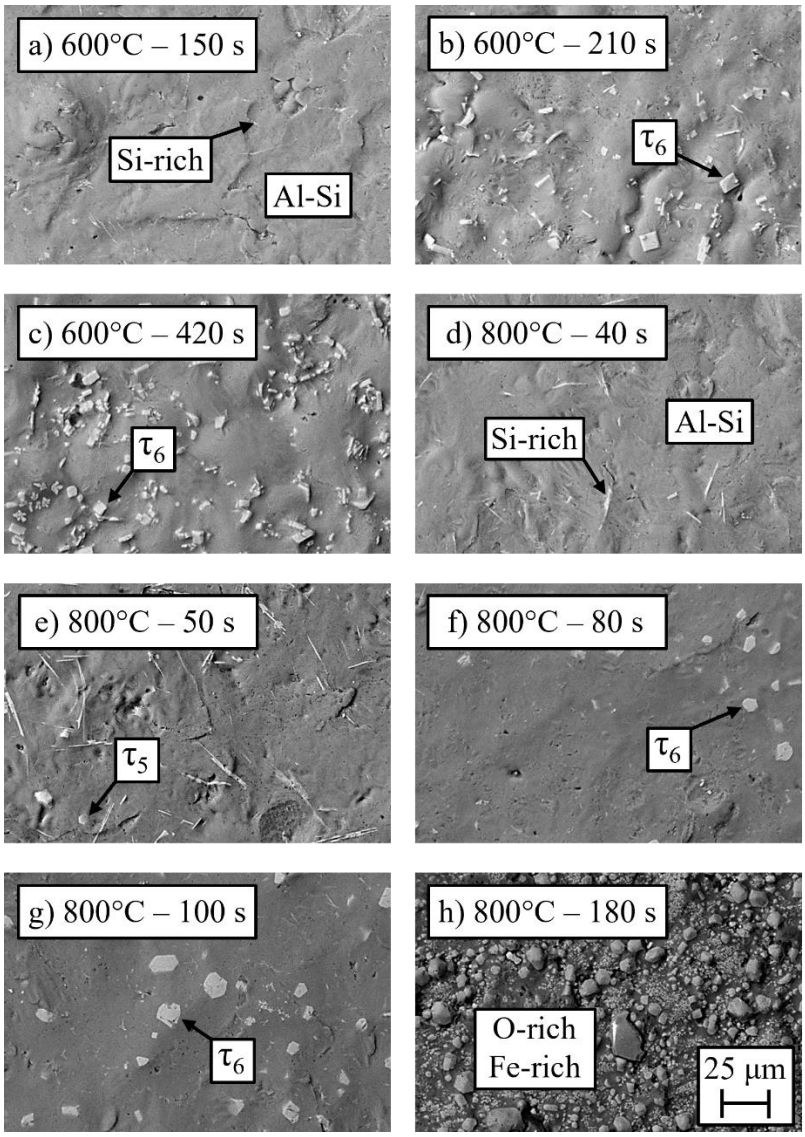

Figure 2-12: Backscattered SEM images at 500x magnification showing phase transformations on the Al-Si coating surface after heating at 600°C for a) 150 s, b) 210 s, and c) 420 s; and at 800°C for d) 40 s, e) 50 s, f) 80 s, g) 100 s, and h) 180 s.

Cross-sectional images with EDS line scans through the coating layer seen in Figure 2-13 yield further information on the development of the coating and the changing reflectance measured with the photodiode. At the 600°C setpoint (Figure 2-13a), τ_6, τ_5, and η sublayers travelled towards the coating surface, while only τ_5 and η compounds could be detected at the

800°C setpoint (Figure 2-13c), similar to literature [14, 37, 68]. Akin to the results in Figure 2-12, iron diffusion occurs more rapidly at the higher furnace setpoint. The oxygen concentration at the surface increases with longer furnace dwell times for both temperature setpoints but remains localized at the surface layer, indicating that a thick oxide layer forms with further dwell time.

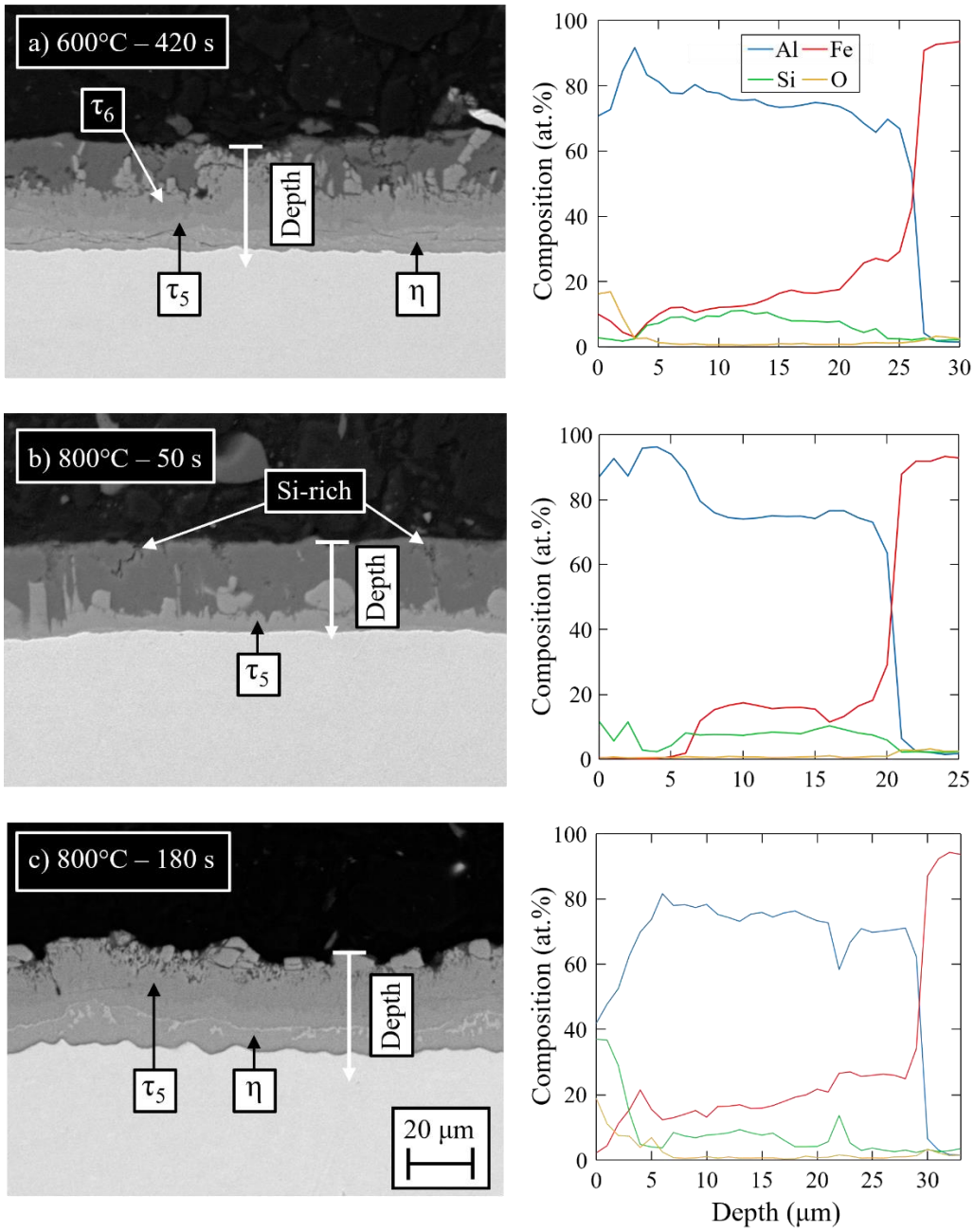

Figure 2-13: Backscattered SEM cross-section images at 750x magnification and EDS line scans showing coating evolution after heating at a) 600°C for 420 s; and 800°C for b) 50 s and c) 180 s.

Cross-sections of samples held at the longest dwell times show intermetallic layers reaching the surface, corresponding with the final decrease in the photodiode signal. It is

clear that intermetallic diffusion through the coating does not cause the initial drop in reflectance after the first peak, as evidenced by Figure 2-13b. However, from the data in Table 2-1, oxygen content begins to increase rapidly after the melting point of the coating, accounting for the change in reflectance of the samples shown in Figure 2-12d and e. Then, once the temperature of the coupon approaches the temperature specified in reaction (4), it is likely a secondary melting reaction occurs, causing the second spike in reflectance, before a combination of oxidation and intermetallic diffusion creates a stable, rough, and non-reflective layer.

While these results provided qualitative insights into how the coating evolved within the furnace, they are limited to a single wavelength, and details regarding the structure of the surface could be inferred from inflection points in a broader spectral signal. Therefore, *ex-situ* spectral reflectance measurements were performed on samples heated according to several heat treatment protocols to compliment the *in-situ* data.

2.3.2 *Ex-situ* Reflectance Measurements and Oxide Characterization

The *ex-situ* reflectance data for quenched samples can be seen in Figure 2-14. Generally, the spectral reflectance is larger at longer wavelengths, at which the samples are optically-smooth. The samples subjected to less extreme heating conditions also display strong peaks from 0.6 μm to 3 μm, caused by constructive and destructive wave interference patterns associated with the oxide layer [55]. In Figure 2-14a, the overall reflectance of the samples increased with increasing furnace setpoint up to 600°C, after which the reflectance dropped sharply when heated to temperatures up to 900°C. As the reflectance decreased, inflection

points in the visible and near-infrared regions disappeared, presumably as the oxide layer thickens, but were replaced by a peak at approximately 10.2 µm. Shi et al. reported a similar peak at 10.7 µm and attributed it to the stretching-mode of intermetallic compounds penetrating the surface of the coating [43, 67]. For the samples heated at 900°C in Figure 2-14b, the reflectance increased at most wavelengths for shorter heating times before dropping for extended dwell times, in addition to the disappearance of the inflection points between 0.6 µm and 3 µm and the appearance of a peak at 10.2 µm, which appeared for the samples heated to 150 s and 300 s. Compared to the *in-situ* reflectance analysis, a significant increase in reflectance was not detected near the melting reactions of the coating, likely due to the state change that occurs when the samples are removed from the furnace and quenched, highlighting the usefulness of analyzing the reflectance of the samples both *in-situ* and *ex-situ*.

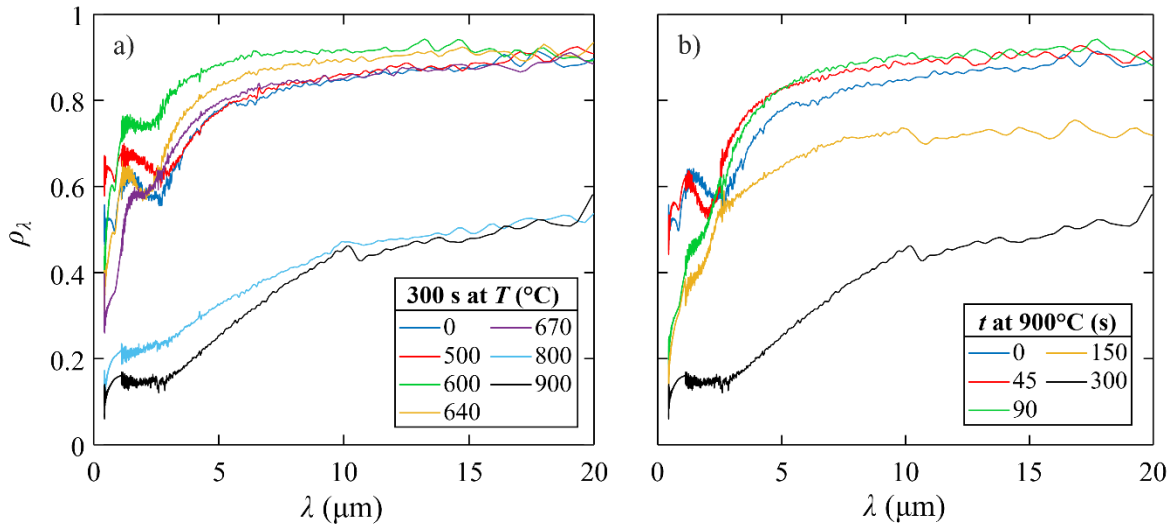

Figure 2-14: a) Effect of heating temperature and b) dwell time at 900°C on the *ex-situ* reflectance of hot stamping samples.

Top-view SEM images of samples subjected to the different heating conditions are shown in Figure 2-15. Although a distinct difference cannot be seen between the as-received sample (Figure 2-15a) and the sample heated to 500°C for 300 s (Figure 2-15b), the remaining samples show drastic changes in surface morphology. The surfaces proportionally roughen with increasing dwell time and furnace temperature due to oxidation and intermetallic diffusion, aligning with the SEM results presented in Section 2.3.1. Small, black oxide nodules appear at the surfaces of samples heated to the more extreme conditions (Figure 2-15e, f, h-j), which was noted by Barreau et al. [39].

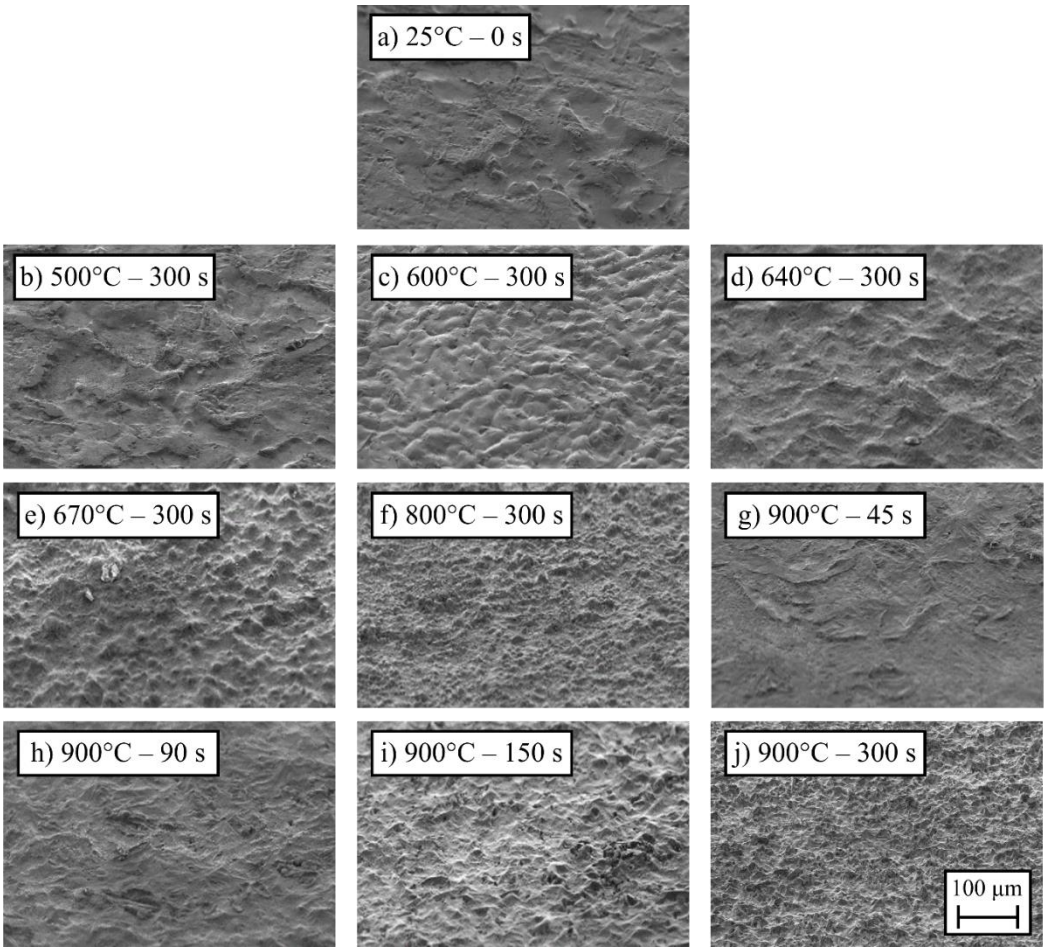

Figure 2-15: Top-view secondary electron SEM images for samples heated at a) 25°C for 0 s (as-received), b) 500°C for 300 s, c) 600°C for 300 s, d) 640°C for 300 s, e) 670°C for 300 s, f) 800°C for 300 s, g) 900°C for 45 s, h) 900°C for 90 s, i) 900°C for 150 s, and j) 900°C for 300 s.

Cross-sectional images of the same samples in Figure 2-15 can be seen in Figure 2-16, showing the degree of oxidation that has occurred at the surface. All the samples except the one heated at 600°C for 300 seconds (Figure 2-16c) show an oxide layer. For the samples heated around the melting reaction temperatures (Figure 2-16d and e) or at 900°C for shorter dwell times (Figure 2-16g and h), an extremely thin and discontinuous oxide layer was detected. A thicker, continuous oxide was detected at the more extreme heating conditions

(Figure 2-16f, i, and j). Moreover, for the sample heated below the melting point of the coating (Figure 2-16b), the oxide layer appeared to be slightly thinner, but more continuous. When comparing these measurements to the spectral reflectances of the samples shown in Figure 2-14, the thickness of the oxide layer was proven to be inversely proportional to reflectance. Because the thickness of the oxide layer remains extremely thin when heated to temperatures slightly above the melting reaction temperatures, the melting reactions have the effect of repeatedly dissolving the oxide layer, before a new oxide forms at the molten surface. When the surface is completely solidified by intermetallics, a thick and robust oxide layer will form at high temperatures, eliminating the film-effect inflection points in the reflectance signal as the roughness of the surface dominates the interaction with electromagnetic waves. Moreover, Figure 2-14a and b suggest that the oxide layer can be modified with heat treatment procedures below the melting point of the coating.

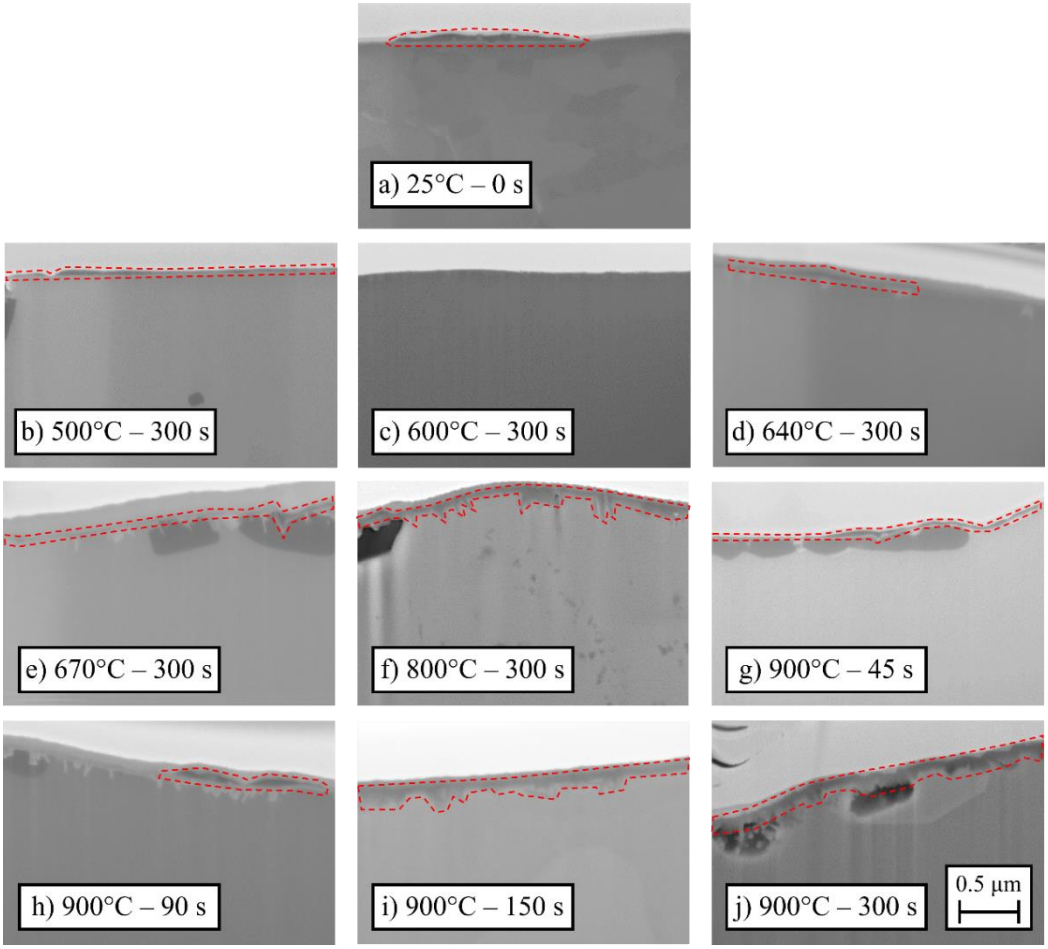

Figure 2-16: Cross-sectional secondary electron SEM images at for samples heated at a) 25°C for 0 s (as-received), b) 500°C for 300 s, c) 600°C for 300 s, d) 640°C for 300 s, e) 670°C for 300 s, f) 800°C for 300 s, g) 900°C for 45 s, h) 900°C for 90 s, i) 900°C for 150 s, and j) 900°C for 300 s. Oxide regions are marked in red.

The thicknesses of the oxide layer on the samples in Figure 2-16 can be seen in Table 2-2, along with the locations of interference peaks (λ_{int}) present in the *ex-situ* reflectance measurement. C_1 and D_1 represent a constructive or destructive interference peak in the 0.6-0.9 µm range, while C_2 and D_2 represent a constructive or destructive interference peak in the 1.1-2.8 µm range. As the oxide layer became thicker and more continuous, the interference

peaks disappeared, approximately at the $\lambda \sim 100D$ criterion given by Lin et al. [54]. Variation in wavelength for the C_1, C_2, and D_2 interference peaks for the samples subjected to different heat treatment methods was detected, but a clear pattern linking the location of these peaks to the thickness of the oxide layer could not be found. This is likely due to the discontinuous nature of the oxide for the samples heated near the melting point of the coating and for lower dwell times at 900°C, making it difficult to produce an appropriate average thickness of the oxide layer. Conversely, the D_1 peak at approximately 0.83 µm was stationary across all the samples that showed interference peaks and aligned with the peak present in the theoretical reflectance curve shown in Figure 2-1, indicating that this peak is likely caused by the refractive indices of the oxide layer rather than a film effect.

Table 2-2: Interference peak locations and measured and calculated oxide thickness for the samples shown in Figure 2-15 and Figure 2-16. Dashes indicate that a corresponding interference peak in the reflectance data or oxide layer thickness could not be tabulated, and an asterisk indicates that the detected oxide layer was discontinuous.

Furnace Temperature (°C)	Holding Time (s)	λ_{int} (µm)				Oxide thickness (nm)
		C_1	D_1	C_2	D_2	
25	0	0.639	0.834	1.493	2.418	46.9* ± 1.9
500	300	0.600	0.835	1.389	2.723	32.4* ± 0.7
600		0.731	0.830	1.458	1.985	-
640		0.763	0.830	1.382	2.038	25.0* ± 0.2
670		-	-	1.626	2.022	22.7* ± 0.9
800		-	-	-	-	53.6 ± 2.2
900	45	0.651	0.829	1.175	1.997	28.6* ± 0.7
	90	-	-	-	-	42.2* ± 1.9
	150	-	-	-	-	87.6 ± 1.9
	300	-	-	-	-	121.6 ± 8.0

2.4 Summary

Through a series of reflectance experiments and SEM-EDS characterization, important findings into the evolution of the Al-Si coating during heating and its oxidation were acquired. *In-situ* reflectance tests confirmed that the dissolution of the coating consists of multiple reaction steps. SEM-EDS measurements on samples quenched near peaks of high and low reflectance suggested an initial decrease in reflectance occurs due to rapid oxidation of the molten surface, before an additional melting reaction at a higher temperature causes a second spike in reflectance, after which intermetallic diffusion combined with oxidation created a rough, reflective surface. Modifying the holding temperature and heating rate of the samples altered the liquefication and solidification dynamics of the coating, indicating that the changes in radiative properties of the blanks and the damage to the furnace rollers caused by molten aluminum contamination could be diminished with careful control of the heating rate within the hot stamping furnace.

Ex-situ reflectance experiments on samples subjected to a variety of heat treatment conditions aligned with the *in-situ* results. More importantly, these measurements showed morphological information about the degree of oxidation and intermetallic development occurring at the surface of the coating through inflection points in the spectral reflectance at shorter and longer wavelengths, respectively. These readings were compared to high-magnification SEM images of the coating surface to determine the structure and thickness of the oxide layer that had formed on the hot stamping blanks. The inflection points

corresponding to the film-oxide effect disappeared as the oxide layer thickened and became more continuous at the more extreme heating conditions.

Although the *in-situ* reflectance measurements provide an informative look into the development of the coating and its oxidation, they were unable to quantify the development of coating topography because the signal was normalized relative to the maximum value in each trial. Among other drawbacks, this approach precludes a quantitative comparison of the evolving surface state when different heating conditions were used. Moreover, peaks in the *ex-situ* spectral reflectance measurements yielded insight into the morphology of a surface oxide layer and intermetallic development, but the relevance of these results was diminished because they were acquired at room temperature. Thus, *in-situ* quantitative measurements of the development of the coating will be detailed in Chapter 3 and *in-situ* spectroscopic measurements inferring the chemical composition of the surface during heating will be provided in Chapter 4.

Chapter 3

In-situ Roughness and Emittance Measurements

This chapter expands upon the laser-based reflectance measurements in the previous chapter by inferring the surface roughness of the blanks during heating through the scattering characteristics of the reflected light. This analysis was applied to blanks with two different coating thicknesses subjected to different heat treatment procedures, to attain a quantitative measurement of the development of the coating. SEM images with EDS analysis compliment the *in-situ* roughness analysis and contrast the intermetallic development and oxidation of the different coating weights. *In-situ* emittance measurements were conducted with a heated stage attached to the FTIR spectrometer to assess the changes in radiative properties during heat treatment, expanding upon the spectral reflectance measurements in Chapter 2. The *in-situ* roughness and SEM-EDS analysis in this chapter has been published in a journal article [69].

3.1 Theory

3.1.1 Surface Roughness

In Chapter 2, changes in surface roughness were shown to have dramatic effects on the radiative properties of the surface. However, the final surface roughness of the blank also influences the heat transfer coefficient and friction between the blanks and the die during forming [70, 71], as well as the paint adhesion [72] and weldability [73] of the blank after hot stamping. Therefore, quantifying the roughness of hot stamping blanks *in-situ* would yield

important benefits to industrial practitioners. The two-dimensional arithmetic average roughness, S_a, is defined by

$$S_a = \frac{1}{L_x L_y} \int_0^{L_x} \int_0^{L_y} |z(x,y)| dy dx \quad (8)$$

where $z(x,y)$ is the difference between the sample height at the (x,y) location and the mean profile height, and L_x and L_y define the extents of the sampling area in the x- and y-directions.

Characterization of surface roughness is typically limited to *ex-situ* profilometry conducted at room temperature for samples heated to various dwell times and then quenched. Studies employing this technique demonstrated that surface roughness increased to a maximum value shortly after the melting of the coating. While most studies showed that a higher heating temperature produces rougher surfaces [17, 43, 68], some others have shown the opposite result [38, 74]. This suggests that the final surface roughness of the blanks is dependent on heating rate in addition to holding temperature. Most studies include roughness measurements after extended dwell times at elevated temperatures, *i.e.*, long after the important melting reactions given in equations (1-5), due to the state change that would occur when the samples are removed from the furnace and quenched. This necessitates the need to determine the roughness of the blanks *in-situ*.

Using the setup specified by Barreau et al. [39] and software to generate 3D height maps from the SEM images, Podor et al. performed *in-situ* roughness measurements on hot stamping samples and found a distinct increase in the surface roughness of the blanks at

approximately 650°C to a maximum value around 3.5 µm at 700°C, before regressing to a final surface roughness of 3.1 µm with further heating to 900°C [75]. While this work provides the most accurate depiction of the evolution of surface roughness of hot stamping samples, assessing the surface roughness of the blanks while using traditional heating methods would be more relevant to the hot stamping industry.

3.1.2 Non-Contact Surface Characterization Techniques

Several laser-based non-contact methods of inferring the structure of a surface have been proposed in literature. When collimated light is reflected off of a surface, variations in surface height cause the reflected and incident light to interfere constructively and destructively. In certain cases, if the scattered light is projected into the far-field, a "speckle" pattern is produced, as seen in Figure 3-1, with bright and dark regions in the image caused by constructive and destructive interference, respectively. While seemingly incoherent, researchers have indirectly related the intensity distribution of the speckle image to the structure sizes of the surface through autocorrelation functions [76, 77].

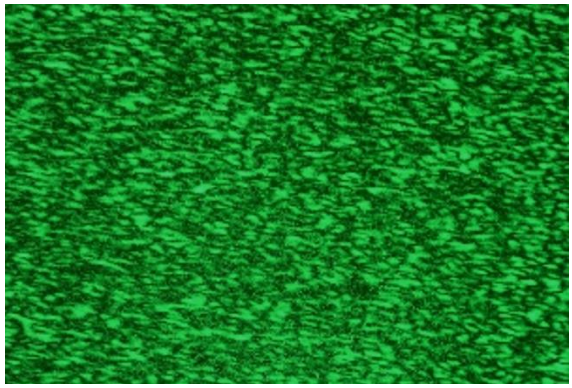

Figure 3-1: Example of a speckle pattern.

More empirical techniques have also been applied to analyze speckle patterns [78, 79]. The standard deviation of the pixel intensities of speckle images has been demonstrated to be proportional to the roughness of the surface if

$$S_a < \frac{\lambda_L}{4\cos\theta_L} \quad (9)$$

where λ_L and θ_L represent the wavelength and incidence angle of the laser, respectively [78]. However, given a laser wavelength of 520 nm and a near-normal incidence angle, this method would only be able to distinguish surfaces with roughnesses less than 0.13 μm, far smoother than hot stamping blanks before or after the heating process.

Surface roughness can also be related to the speckle pattern by a technique known as the "bright-dark ratio method" or "binary analysis" [80-82]. In this method, a threshold is specified, and each pixel within the speckle image is converted to one or zero if that specific pixel intensity is greater or smaller than the threshold intensity, respectively, creating a binarized image. The ratio of the total number of bright (B) and dark (D) pixels can then be correlated to the roughness of the surface, usually according to

$$S_a \propto \frac{1}{(B/D)^2} \quad (10)$$

A previous work showed that a threshold of the mean intensity of the image pixels mitigated noise and produced monotonic results [83].

3.1.3 Spectral and Total Emittance

While the roughness of a surface can be correlated to its radiative properties, the spectral emittance, ε_λ, has been measured directly at high temperatures in the literature [84-86]. Spectral emittance is defined as the ratio of emitted radiation with respect to wavelength over a hemisphere by a surface, E_λ, to a blackbody at the same temperature, $E_{\lambda,b}$. Spectral emittance can be related to spectral reflectance and absorptance through Kirchhoff's law, $\varepsilon_\lambda = \alpha_\lambda$, and if the spectral transmittance, τ_λ, of the surface is neglected,

$$\varepsilon_\lambda = 1 - \rho_\lambda \quad (11)$$

The total, hemispherical emittance, ε, can be acquired by integrating the spectral emittance over all wavelengths according to

$$\varepsilon = \frac{\int_0^\infty \varepsilon_\lambda E_{\lambda,b}(\lambda,T)d\lambda}{\int_0^\infty E_{\lambda,b}(\lambda,T)d\lambda} = \frac{\int_0^\infty \varepsilon_\lambda E_{\lambda,b}(\lambda,T)d\lambda}{\sigma T^4} \quad (12)$$

where σ is the Stefan-Boltzmann constant.

Ideally, the spectral emittance of a surface, $\varepsilon_{\lambda,x}$, can be determined by dividing its emission measured by a detector, $S_{\lambda,x}$, by the emission of a material at the same temperature, $S_{\lambda,ref}$, with known spectral emittance, $\varepsilon_{\lambda,ref}$, according to

$$\varepsilon_{\lambda,x}(T) = \varepsilon_{\lambda,ref}(T)\frac{S_{\lambda,x}(T)}{S_{\lambda,ref}(T)} \quad (13)$$

Often, a blackbody cavity with high spectral emittance (>0.99) is used as the reference, and $\varepsilon_{\lambda,ref} \approx 1$. However, Xiao et al. [87] states that this equation is only valid when the

background emission is negligible. They propose that the spectral emission measured by a detector can be characterized by

$$S_{\lambda,x}(\mathrm{T}) = m_\lambda\left[\varepsilon_{\lambda,x}(T)I_{\lambda,b}(T) + B_\lambda(T)\right] \quad (14)$$

where m_λ is the spectral response function or the sensitivity of the detector, B_λ is the background emission, and $I_{\lambda,b}$ is the blackbody spectral intensity given by Planck's law [52]. If the emittance of a reference is independent of temperature, the spectral response function can be calculated by taking measurements at two temperatures, according to [87]

$$m_\lambda = \frac{S_{\lambda,ref}(T_1) - S_{\lambda,ref}(T_2)}{\varepsilon_{\lambda,ref}\left[I_{\lambda,b}(T_1) - I_{\lambda,b}(T_2)\right]} \quad (15)$$

Moreover, if the spectral emittance of a surface is known to be temperature-independent, it can be calculated without knowing the background and spectral response function by taking measurements at two temperatures, according to equation (16) [87]

$$\varepsilon_{\lambda,x} = \varepsilon_{\lambda,ref}\frac{S_{\lambda,x}(T_1) - S_{\lambda,x}(T_2)}{S_{\lambda,ref}(T_1) - S_{\lambda,ref}(T_2)} \quad (16)$$

However, if the background is non-negligible and the emittance of the surface changes with temperature, a full calibration of the measurement setup is required to find the contribution of the background, which is documented by Xiao et al. [87].

3.2 Experimental Methods

3.2.1 *In-situ* Roughness Measurements and Effect of Coating Weight

To acquire the speckle patterns used for the *in-situ* roughness measurements, a modification was made to the *in-situ* reflectance apparatus in Chapter 2, as shown in Figure 3-2. Instead of directing the light reflected from the sample into a photodiode, a portion of the scattered light was projected onto the imaging chip of a Nikon® D7200 camera. The camera was automatically triggered to capture a picture approximately every two seconds using the DAQ, and the resultant images were cropped to an area measuring 500 x 500 pixels.

Samples were removed from the furnace and quenched at intermediate dwell times at setpoints of 600°C and 900°C and then analyzed with an optical profilometer (Wyko® NT1100) to corroborate the *in-situ* surface roughness measurements. These experiments used AS150 Usibor® samples [3, 10] measuring 38 mm x 38 mm x 2.0 mm and instrumented with K-type thermocouples, which were heated to setpoints of 600°C, 700°C, 800°C, and 900°C.

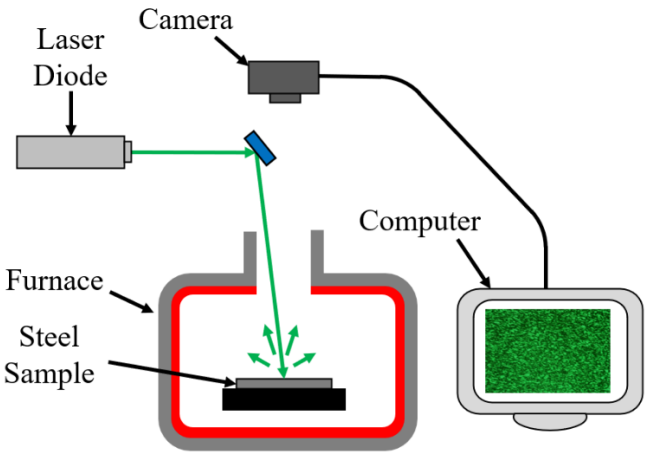

Figure 3-2: *In-situ* speckle pattern analysis schematic.

To illustrate the effect of coating weight, the *in-situ* roughness experiments were also performed on AS80 coated samples measuring 38 mm x 38 mm x 2.0 mm. AS80 and AS150 coupons were heated to 600°C and 900°C and extracted at various dwell times and subjected to SEM-EDS analysis to assess the differences in intermetallic diffusion between the two coating weights. In these tests, the average surface chemical composition was calculated over an approximately 500 µm x 400 µm region.

3.2.2 *In-situ* Emittance Measurements

To acquire the *in-situ* emittance measurements, sapphire discs from Edmund Optics® (36-252) and circular AS150 Usibor® 1500 samples [3, 10] measuring 2.0 mm thick with a diameter of 12.7 mm were placed into a Specac® High Temperature High Pressure (HTHP) cell, which can be seen in Figure 3-3 [88]. High temperatures are achieved by a resistively-heated block surrounding the sample. Emission from the sample is then directed into the FTIR via a series of mirrors, where it passes through an interferometer and various optical components before reaching the DTGS detector, as seen in Figure 3-4. The DTGS detector can theoretically measure emission at wavelengths greater than 1.1 µm, but due to noise limitations, a lower and higher limit of 2 µm and 25 µm was set. Because the FTIR measurement will be comprised of emission primarily in the normal direction, spectral and total emittance measurements will be assigned labels of $\varepsilon_{\lambda,n}$ and ε_n, respectively.

Figure 3-3: Specac® High Temperature High Pressure cell [88].

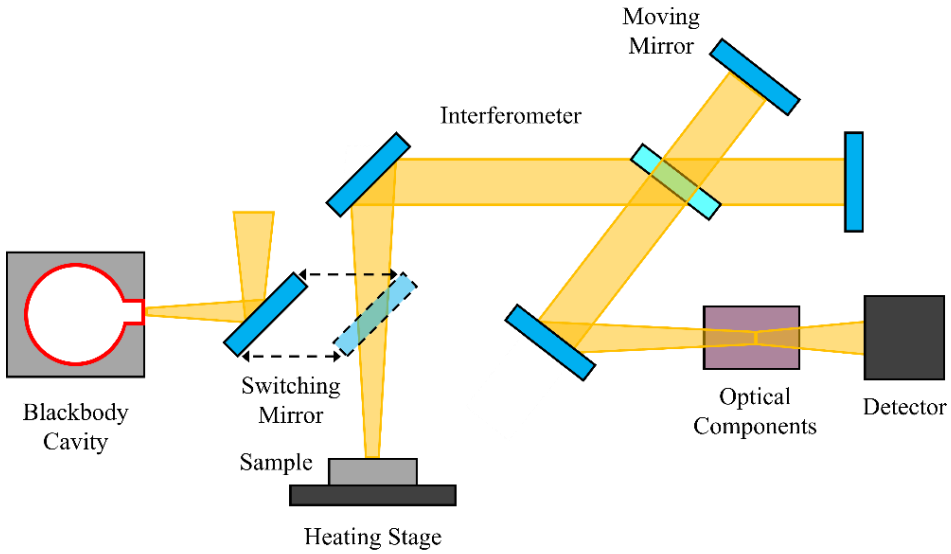

Figure 3-4: Schematic for FTIR reflectometer and heated stage for *in-situ* emittance measurements.

The emission signal is converted to spectral emittance by using equations (13) or (16). An Infrared Systems Development Corporation® IR-563/301 blackbody source with $\varepsilon > 0.99$ [89] was used as the reference. The window facing the FTIR was removed to avoid accounting for the transmittance of the window. Initial testing on the sapphire samples was

performed at 380°C, 400°C, and 420°C to assess to accuracy of the measurement process. The spectral emittance of sapphire is generally independent of temperature in the 6-10 μm range, where it exhibits a plateau close to unity, and increases slightly with increasing temperature at higher and shorter wavelengths, with a characteristic peak at approximately 16 μm [90, 91]. For the hot stamping samples, a K-type thermocouple was welded to the opposite side of the samples and threaded out through the window opening to monitor temperature. These samples were heated from room temperature to approximately 680°C at 0.5°C·s, which were the maximum heating conditions allowable by this system. A total of five individual trials were performed to assess the repeatability of the experiments.

3.3 Results

3.3.1 *In-situ* Roughness Measurements

To build a dataset linking *B*/*D* measurements to surface roughness, a variety of samples were first heated to different furnace temperatures and dwell times and extracted from the furnace and quenched. The samples were then placed in the furnace at room temperature and a speckle image was captured to generate a *B*/*D* value. Finally, the surface roughness of the blanks was measured using a profilometer, and the roughness measurement compared to the *B*/*D* value can be seen in Figure 3-5. A decreasing exponential relationship was attained as given in equation (17)

$$S_a = 1.12(B/D)^2\text{-}2.60(B/D)\text{+}3.19 \quad (17)$$

which aligns with equation (10) and the results of Kayahan et al. [80]. Some significant outliers were detected, which were as-received AS150 coupons. These outliers were excluded from the fitting process, and their potential origin will be discussed later in this section.

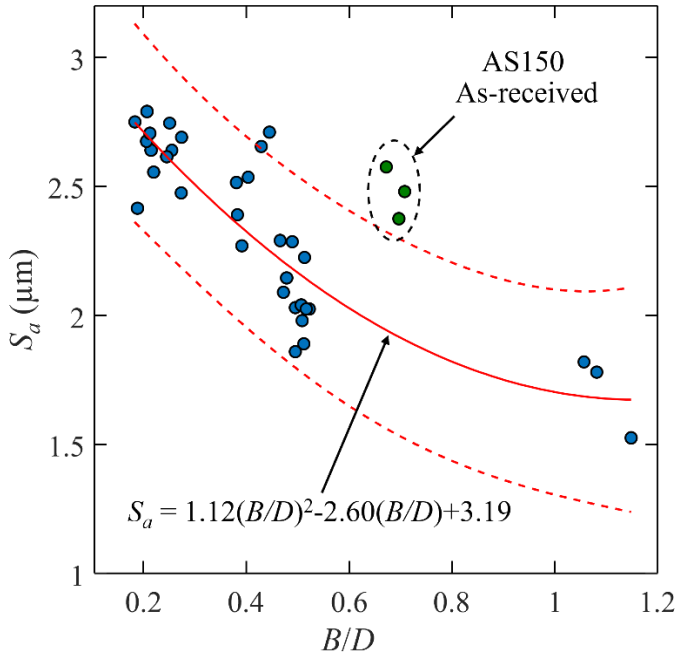

Figure 3-5: *B/D* value for *ex-situ* samples (blue) with quadratic line of best fit with 95% confidence interval (red) and neglected outliers (green) vs. surface roughness.

In-situ B/D signals were generated on samples heated to 600°C, 700°C, 800°C, and 900°C, and an example at the 800°C setpoint can be seen in Figure 3-6a. Similar to the photodiode signal measurements in Figure 2-8a, the *in-situ B/D* signal showed a spike at the melting point of the coating and shortly thereafter, but the peaks are less distinguished and without a corresponding drop between them. This indicates two distinct decreases in roughness followed by a sharp increase after increased oxidation and intermetallic compounds diffuse to the surface. Before the *B/D* signals were converted to roughness values, the average of ten

trials was acquired. An example of this process at the 800°C setpoint is shown in Figure 3-6b, along with the 95% confidence interval. It appears the averaging process has further obscured the two individual peaks.

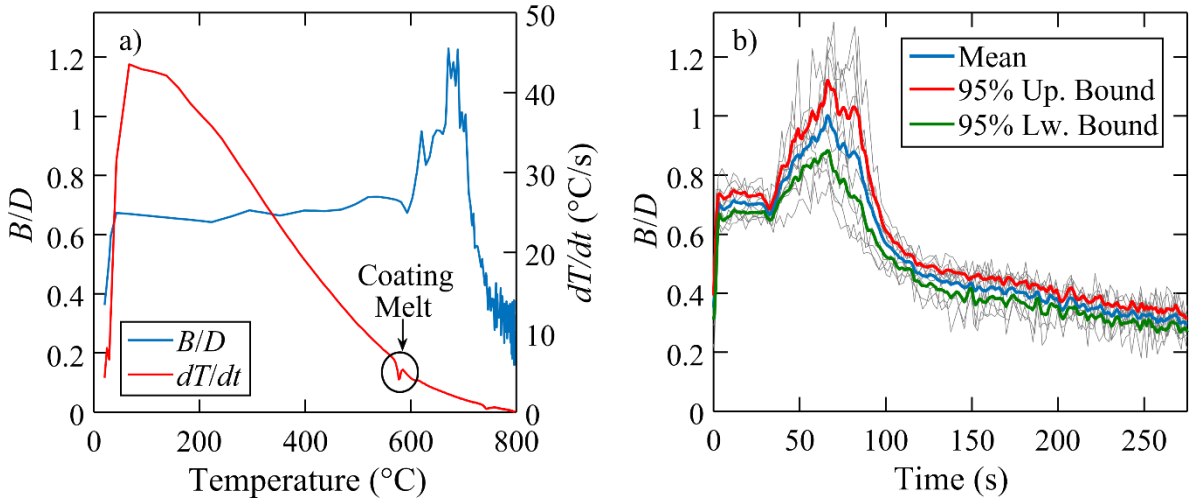

Figure 3-6: a) B/D vs. dT/dt for an AS150 sample heated at the 800°C setpoint and b) 10 B/D plots for AS150 samples heated at the 800°C setpoint (gray), with the mean and 95% confidence interval.

Using the average B/D signals and equation (17), *in-situ* roughness profiles were produced, as seen in Figure 3-7. For the furnace setpoints between 700°C and 900°C, the surface roughness decreased at the melting point of the coating before increasing as the surface solidified through oxidation and intermetallic diffusion, while the samples heated to 600°C only progressively roughened when the coating melted. This mirrors the *in-situ* reflectance measurements in Section 2.3.1. In general, the surface roughness of the blank at the end of heat treatment was proportional to heating temperature, but there was a minimal difference between the setpoints of 700°C and 900°C and a large difference between 600°C and the

higher testing temperatures, pointing to temperature-dependent reactions occurring between 600°C and 700°C, such as reactions (2), (3), and (4). The roughness curve at 900°C mostly aligns with the findings of Podor et al. [75], but shows a slight decrease in roughness at the initial melting of the coating at 577°C and a lower final roughness of 2.7 µm compared to approximately 3.4 µm. Shi et al. also show a final roughness value around 3.4 µm when heating samples to 900°C, but samples tested at the same temperature for similar dwell times by Borsetto et al. [68] and Ghiotti et al. [74] have final roughnesses of 2.3 µm and 2.4 µm, respectively. This indicates that there could be significant variability in the samples themselves or the heating method incurs differences in the final surface state of the blanks.

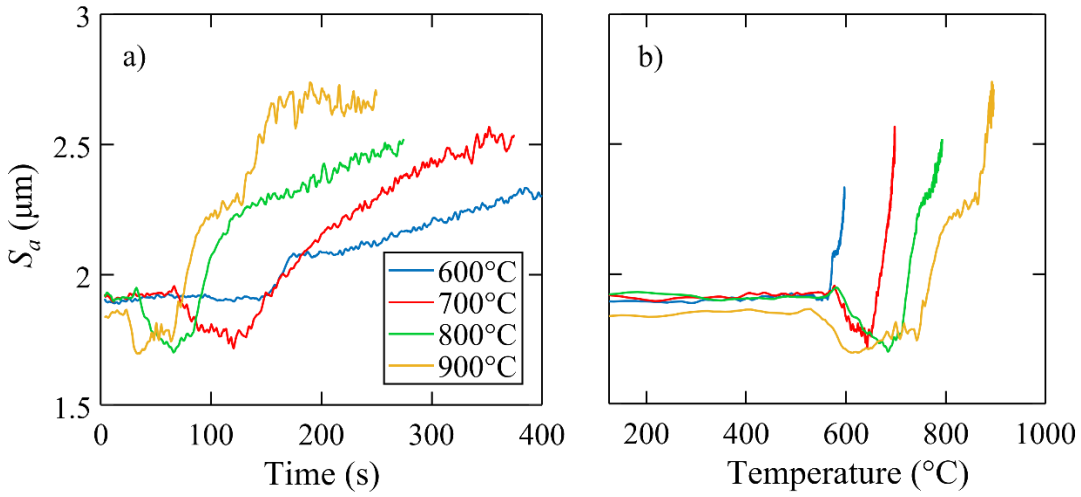

Figure 3-7: Mean of ten *in-situ* roughness profiles at furnace setpoints of 600°C, 700°C, 800°C, and 900°C vs. a) time and b) temperature.

The *ex-situ* roughness of samples extracted at the 600°C and 900°C setpoints measured using a profilometer was compared to the *in-situ* roughness profiles to validate the accuracy of the roughness measurements predicted by the *in-situ* B-D ratio method, which can be seen

in Figure 3-8. The two measurement methods closely align at the end of the heating cycle, when the coating has completely solidified. However, the *in-situ* prediction is notably lower than the sample heated to 900°C for 50 s and the as-received coupons (gray). The former case could be attributed to the state change that occurs when the samples with a molten coating are removed from the furnace and quenched, again emphasizing the importance of performing the roughness measurements *in-situ*.

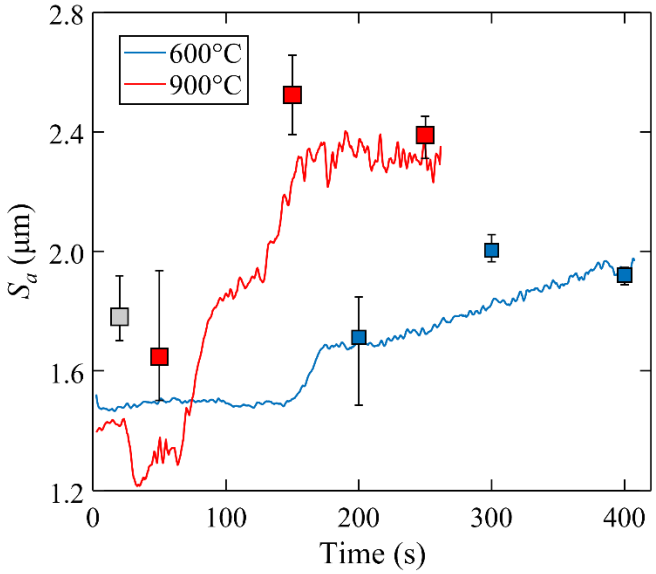

Figure 3-8: *In-situ* roughness prediction for samples heated at 600°C and 900°C furnace setpoints with the mean of three *ex-situ* roughness measurements at various furnace dwell times. The gray data point represents as-received samples.

However, this hypothesis does not explain why the *in-situ* roughness prediction would be significantly lower than the *in-situ* prediction in the as-received case. To this end, optical profilograms were captured of the as-received coupons and three samples heated at 900°C for 50 s, 150 s, and 250 s, as seen in Figure 3-9. For the as-received sample in Figure 3-9a and b, locally flat areas separated by large height differences were detected, perhaps as a result of

"air knives" which smooth the surface of the Al-Si coating after hot dipping. While the profilometry results capture and incorporate this phenomenon into the roughness measurement, the speckle-inferred measurements do not, and underpredict the roughness for as-received samples.

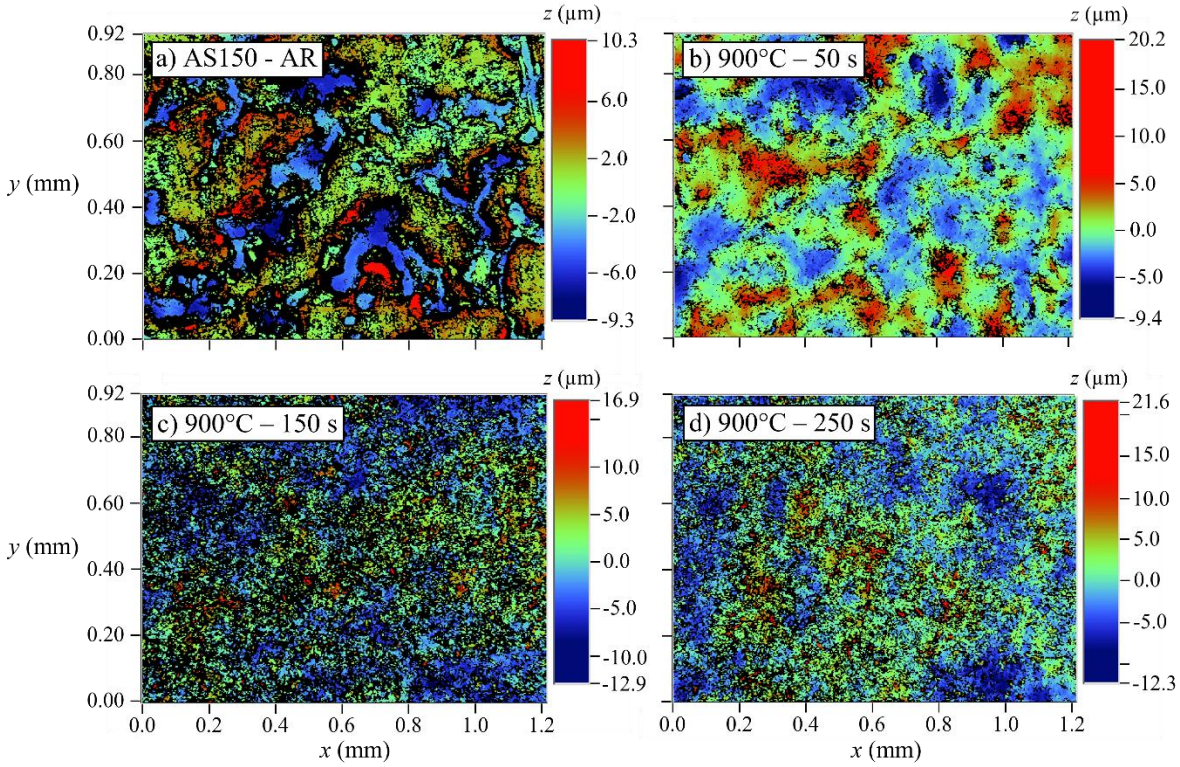

Figure 3-9: 2D height maps for an AS150 coupon heated at 900°C for a) 0 s (as-received), b) 50 s, c) 150 s, and d) 250 s.

3.3.2 Effect of Coating Weight

With the previous section establishing the validity of the *in-situ* roughness method, this technique was applied to AS80 samples with the thinner coating to investigate the impact of thickness on the evolution of the Al-Si coating. Heating curves for setpoints of 600°C, 700°C, 800°C, and 900°C for the two coating weights can be seen in Figure 3-10. From these

results, it appears that the AS80 samples heat slightly faster than the AS150 coated blanks. As demonstrated in Figure 1-7, coating liquefication causes a drop in the blank heating rate, while the roughening of the surface after intermetallic diffusion allows the blanks to absorb heat more effectively. Therefore, if the coating applied to the AS80 blanks solidifies in less time due to the decreased diffusion path, the required austenitization time in the furnace may be reduced. While Billur and Son claim that this is the case [92], Yakubtsov and Sohmshetty show similar heating profiles regardless of coating thickness [93].

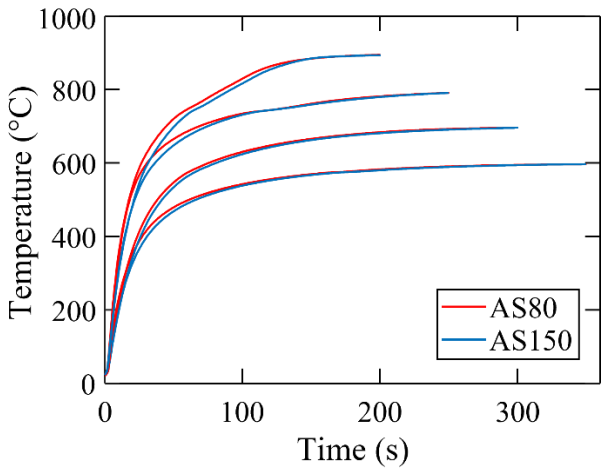

Figure 3-10: Heating profiles for furnace setpoints of 600°C, 700°C, 800°C, and 900°C for AS80 and AS150 coating weights.

The *in-situ* roughness method in Section 2.3.2 was applied for AS80 samples and compared to the previous results in Figure 3-8, which can be seen in Figure 3-11. From these results, the intermetallic compounds penetrate the top of the AS80 coating at lower temperatures and times compared to the AS150 coupons, due to the decreased diffusion path length. This was also demonstrated by Windmann et al., who showed that thinner coatings converted into η and AlFe compounds in less time [94]. Additionally, after heat treatment to

900°C, the AS80 blanks were slightly rougher than the AS150 blanks. Although the implementation of a thinner coating may not significantly affect the heating rate of the coupons, if the overall liquid window of the molten coating is shortened, the less time the furnace rollers are susceptible to Al-Si contamination, and roller life could be extended.

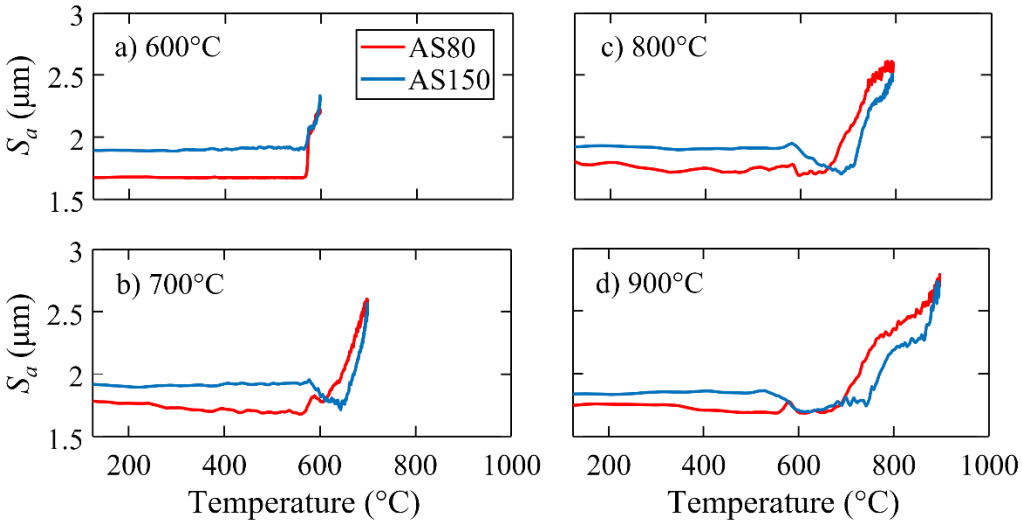

Figure 3-11: Mean of ten *in-situ* roughness profiles for AS80 and AS150 coupons at furnace setpoints of 600°C, 700°C, 800°C, and 900°C.

Ex-situ SEM-EDS experiments were also performed to assess the oxide and intermetallic development of the different coatings after different heat treatment regimens. The average surface compositions are shown in Table 3-1. Similar to the results in Table 2-1, iron and oxygen content increased as the samples were heated in the furnace for longer dwell times, and this effect was intensified at the 900°C setpoint. Again, these results align with the findings of Shi et al. [43, 67]. Due to the decreased diffusion path length, AS80 coupons are expected to contain more surface iron than AS150 blanks at a given heating time.

Table 3-1: Coupon surface composition by coating weight, furnace setpoint and dwell time.

Coating weight	Furnace setpoint (°C)	Dwell time (s)	Chemical composition (at. %)			
			Al	Fe	Si	O
AS80	-	0	83.3	0.6	13.4	2.7
	600	240	87.2	1.0	5.2	6.6
		480	84.0	3.2	2.6	10.2
	900	60	80.3	1.5	10.4	7.8
		120	65.7	12.7	7.7	13.9
AS150	-	0	77.9	0.5	13.8	7.8
	600	240	82.6	0.5	12.7	4.2
		480	85.7	2.0	2.6	9.7
	900	60	77.9	0.5	13.2	8.4
		120	74.7	2.1	9.6	13.6

The microstructural development at the surface of the coating can be seen through the SEM images and EDS analysis in Figure 3-12. Corresponding with the *in-situ* roughness measurements in Figure 3-11, τ_5 and τ_6 compounds are more abundant for the AS80 specimens for both heating temperatures. Additionally, while both τ_5 and τ_6 were detected at the 600ºC setpoint, only τ_5 was detected for the samples heated to 900°C. Both Shi et al. [43, 67] and Barreau et al. [39] documented τ_5 compounds but not τ_6 when heating to temperatures above 600°C. The intermetallic compounds also formed in square and hexagonal shapes at the higher heating temperature, but tended to propagate in large amorphous clusters at 600°C.

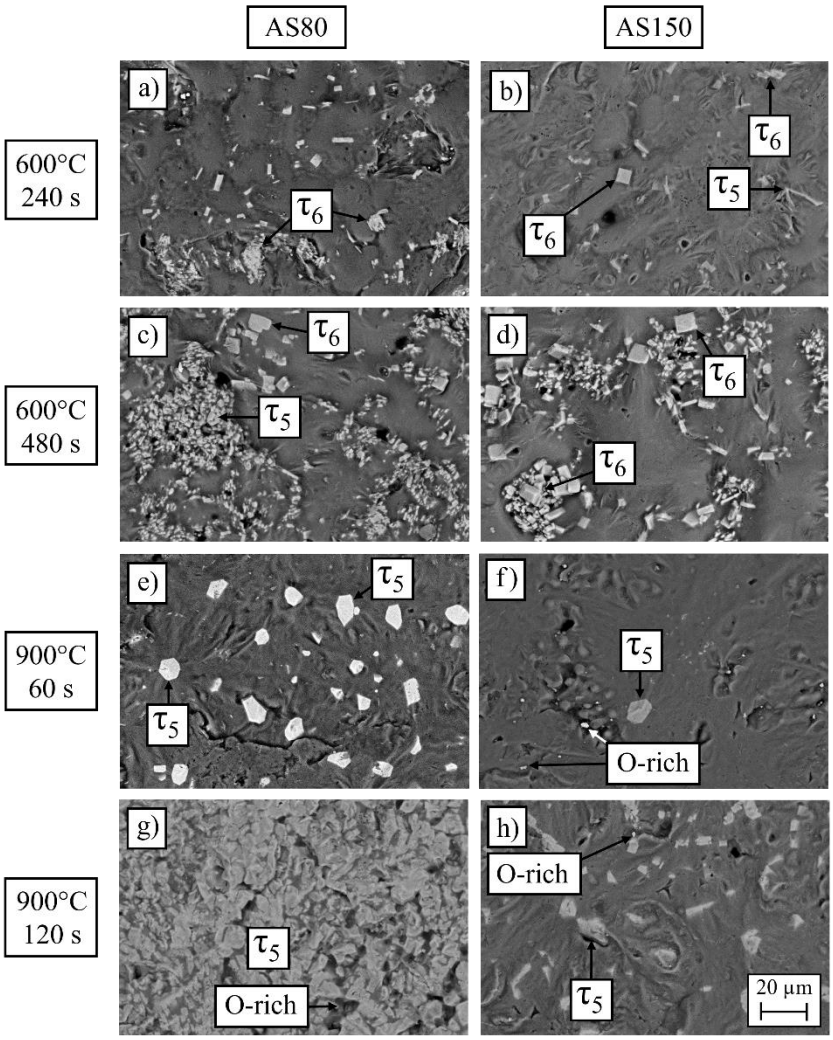

Figure 3-12: Backscattered SEM top-view images at 750x magnification for AS80 and AS150 coupons heated at 600°C for a-b) 240 s and c-d) 480 s; and 900°C for e-f) 60 s and g-h) 120 s.

Cross-sectional SEM images were also acquired to highlight any differences in intermetallic layer development between the two coating weights, which can be seen in Figure 3-13, and EDS analysis was used to characterize the various intermetallic sublayers within the coating. (The top portion of the coating in Figure 3-13g was destroyed during the mounting process, concealing the intermetallic compounds present near the surface.) These images reveal that a distinct τ_5 layer was present in almost all the images and for both coating

weights, preceded in some cases by τ_6. With further heating durations, binary layers of η and ζ appeared near the steel-coating interface as the τ_5 and τ_6 layers travelled towards the surface. These results generally agree with the SEM images in Figure 2-13, and provide a more detailed description of the layers that form at the 900°C setpoint. Yakubtsov and Sohmshetty note that the microstructural development of AS80 and AS150 coupons were essentially identical [93]. It did not appear that the rate of intermetallic diffusion was higher for either coating weight, but due to the decreased thickness of the AS80 coating, intermetallic compounds reach the surfaces earlier for these samples compared to the AS150 blanks. Windmann et al. found samples with far higher proportions of η compounds than the current study and even found thin bands of τ_1 in both AS80 and AS150 blanks (referred to as AS140 in their work), but the difference may be attributed to the higher soaking temperature of 920°C [94].

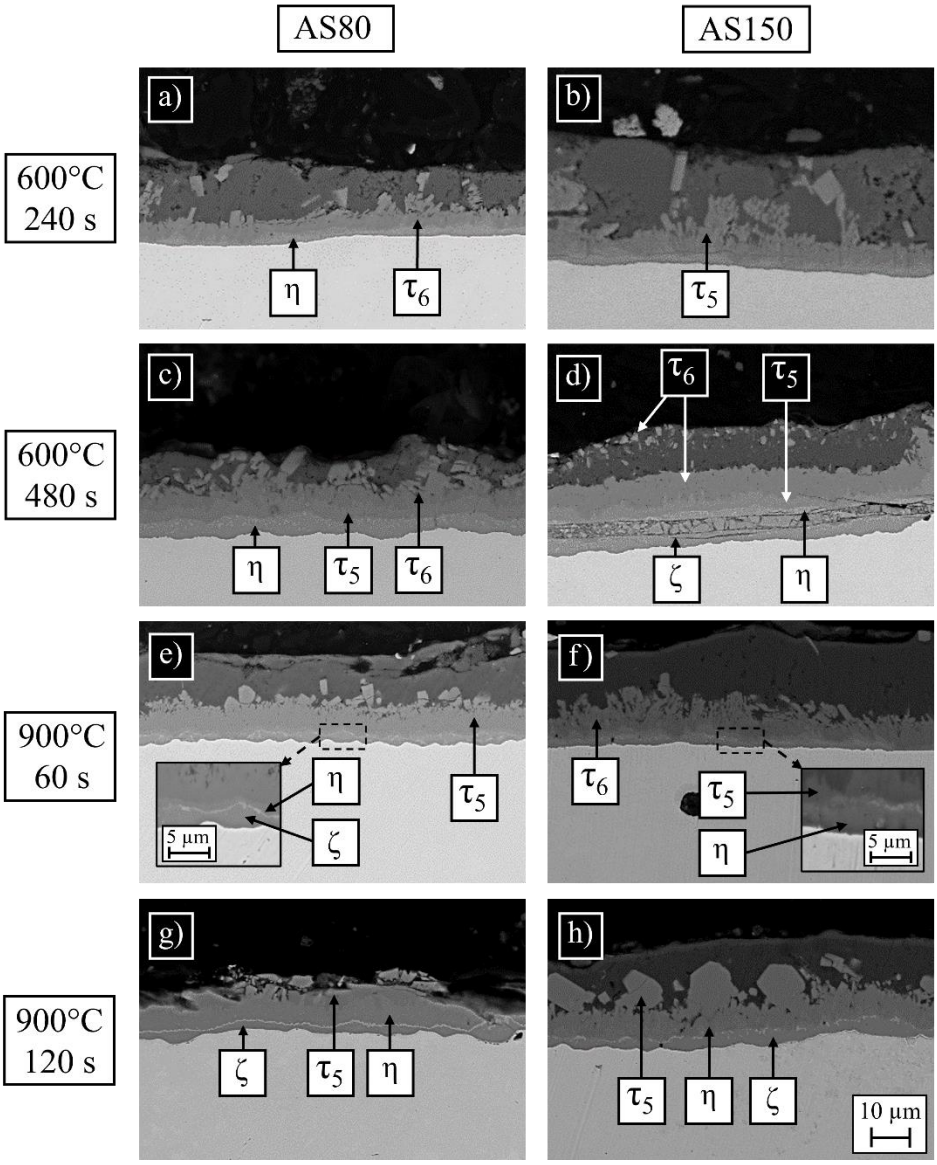

Figure 3-13: Cross-sectional SEM images at 750x magnification for AS80 and AS150 coupons heated at a-b) 600°C for 240 s and c-d) 480 s; and 900°C for e-f) 60 s and g-h) 120 s.

Therefore, it appears as though there is no discernable difference in the heating rate or the final composition of intermetallic compounds between the AS80 and AS150 coating weights. Because the intermetallics diffuse to the surface in less time for the AS80 blanks and could

mitigate roller contamination issues, hot stamping practitioners may opt for thinner coatings, but this selection may come at the cost of decreased corrosion performance [95].

3.3.3 *In-situ* Emittance Measurements

To aid in the development of heat transfer models, *in-situ* emittance measurements were performed to build upon the *in-situ* reflectance and roughness measurements. Tests on sapphire discs at a variety of temperatures and temperature combinations according to equations (13) and (16) can be seen in Figure 3-14a and b, respectively. Dividing the measured emission of the sapphire disc by the measured emission of the blackbody according to equation (13) at temperatures of 380°C, 400°C, and 420°C (Figure 3-14a) produced very similar results, with a slight increase in the spectral emittance outside 6-10 µm with increasing temperature, aligning with the results of Sova et al. [90, 91]. When compared directly to the results of Xiao et al. [87], general agreement was found when measuring over the same wavelengths. However, the emittance exceeded unity in the 6-10 µm range, indicating that there is an issue in the measurement process, as the emission from a sample should never be greater than a blackbody. It is possible that contribution from the background could be influencing the measurement, and spectral emittances were generated from two temperatures according to equation (16), as seen in Figure 3-14b. This caused the measurement to stray from the results of Xiao et al. [87] and introduced discrepancies in the emittance between the different temperature combinations. Emittance values in the 6-10 µm range even greater compared to Figure 3-14a were shown, and the emittance increased above unity at the peak near 21 µm.

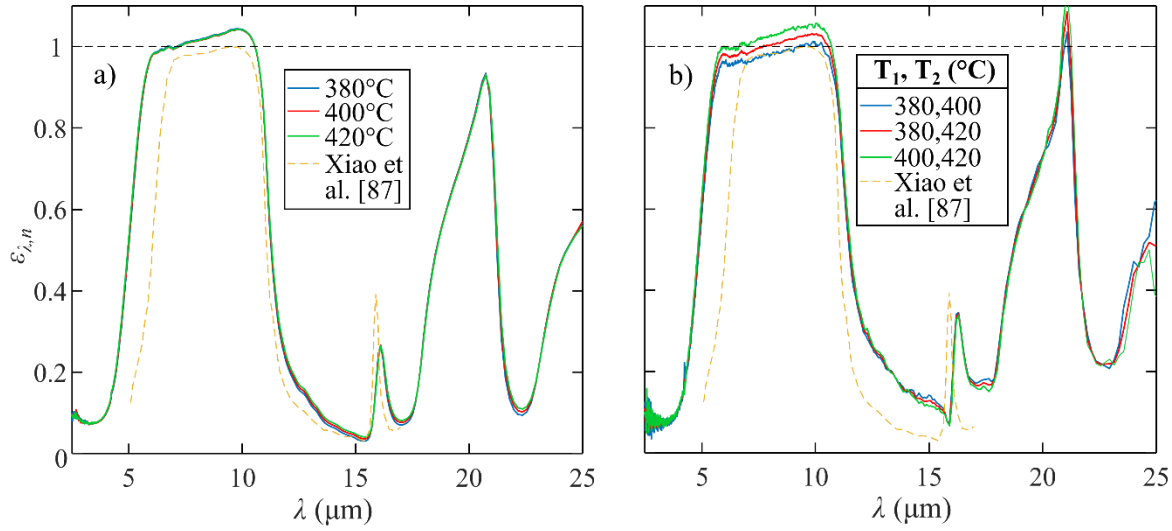

Figure 3-14: *In-situ* spectral emittance measurements of a sapphire sample using a) equation (13) and b) equation (16).

The spectral response function was then calculated to determine if the detector is more sensitive to measurements at different temperature combinations, which can be seen in Figure 3-15. However, excellent agreement was found, especially below 15 μm. This indicates that the issues present in the measurements of Figure 3-14 are due to misalignment in the optical paths between the HTHP cell and the blackbody reference, and that the error is not due to the calibration of the FTIR system. Additionally, because the samples are perpendicularly aligned to the FTIR, multiple reflections between the sample and the FTIR detector may induce error in the measurement process. This effect is discussed by Xiao et al. [87], who suggest near-normal alignment to avoid this issue. However, the HTHP cell in this setup is rigidly fixed and cannot be angled during testing. Representatives from the FTIR manufacturer, Bruker®, acknowledged issues within the testing setup, and suggested the measured emission from the HTHP cell be multiplied by a correction factor of 0.947.

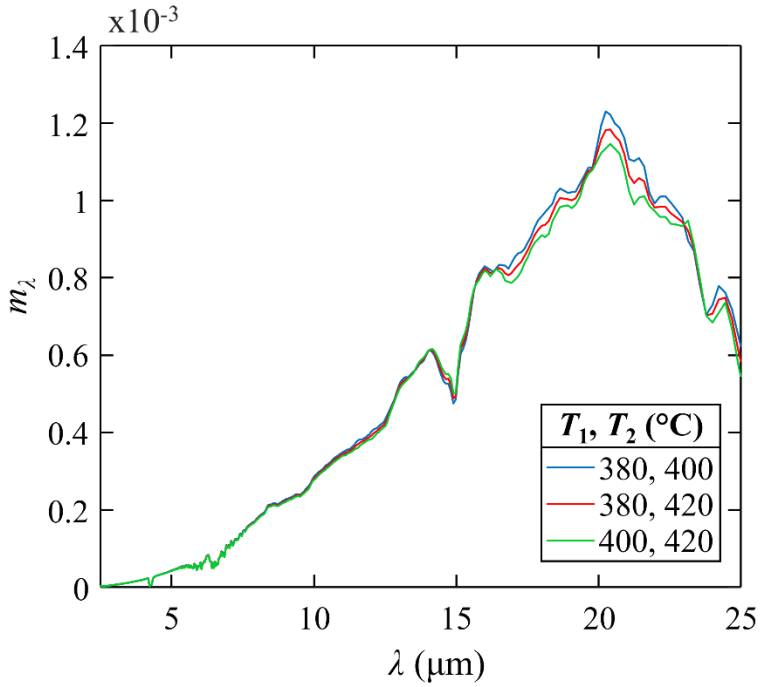

Figure 3-15: Spectral response function of DTGS detector at different temperature combinations.

The spectral emittance of hot stamping samples was then measured using equation (13), as it gave the most repeatable results, and the correction factor suggested by Bruker®. These results can be seen in Figure 3-16a. The first elevated temperature measurement at 467°C shows slightly higher spectral emittance compared to the spectral emittance from the as-received sample calculated from the reflectance in Figure 2-14 using equation (11), but this is expected as the emittance of metals increases with temperature according to the Hagen-Rubens relation [52]. Additionally, absorption bands for CO_2 and H_2O at 2.6 μm, 4.3 μm, and 6.3 μm causing inflection points in the *in-situ* emittance signal are present, aligning with literature results [96-98]. As the temperature increased to the initial melting point of the coating, the spectral emittance decreased at wavelengths below 11 μm, before increasing at

all wavelengths to a final value when the samples reached their maximum temperature of approximately 681°C. Moreover, similar to the results in Figure 2-14, a peak at 10.2 µm emerges at approximately 658°C, indicating intermetallic compounds have penetrated the surface of the coating. However, despite the use of the correction factor, the spectral emittance between 2-2.4 µm for the samples at the highest temperatures is still slightly above unity, diminishing the credibility of these results. Nevertheless, the total emittance based on these measurements integrated according to equation (12) can be seen in Figure 3-16b. Here, a slight increase in the total emittance is observed until approximately 577°C, until a sharp decrease is detected at the initial melting point of the coating. The total emittance remains at the decreased value until approximately 660°C, after which it increases to its final value of approximately 0.87. These results strongly correlate with the *in-situ* roughness measurements shown in Figure 3-7.

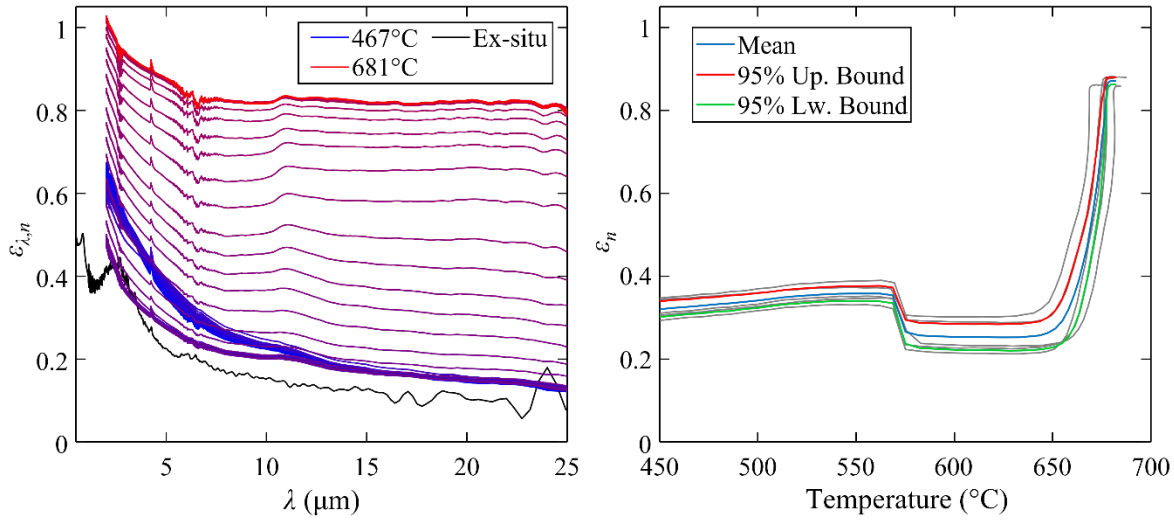

Figure 3-16: a) spectral emittance for hot stamping samples heated between starting and finishing temperatures of 467°C and 681°C and b) total emittance for five samples with the mean and the 95% confidence interval.

Although these results follow the appropriate trends outlined in previous literature results covering *in-situ* radiative property measurements [30, 62], their relevance to industrial practitioners is dubious. As previously mentioned, the spectral emittance is greater than unity between 2-2.4 μm. Moreover, due to limitations in the sensitivity of the detector, measurements at wavelengths only greater than 2 μm could be made. This is problematic as wavelengths less than 2 μm make up a significant contribution to the emission profile in the studied temperatures, biasing the calculated total emittance to the values at longer wavelengths. Finally, the heating rate of the HTHP cell is much lower than what would normally be used in hot stamping operations, and extrapolating these results to industrially relevant heating rates would be challenging. Nonetheless, these results provide the framework for future, refined *in-situ* emittance measurements, which will be discussed in Chapter 5.

3.4 Summary

The measurements performed in this section build upon the reflectance measurements in the previous chapter by providing *in-situ* quantitative methods of characterizing the development of the coating. *In-situ* roughness experiments showed a decrease at the initial melting of the coating followed by large increases in roughness as intermetallic compounds solidified the molten coating. *Ex-situ* roughness tests on samples extracted from the furnace at intermittent dwell times showed general agreement, especially after the solidification of the coating. These tests also showed that higher dwell temperatures solidified the coating in less time and

produced a rougher surface, indicating temperature-specific melting reactions occurring between 600°C and 700°C, agreeing with the results of Chapter 2.

In-situ roughness tests were also performed on thinner AS80 coated blanks and compared to the thicker AS150 coating. Due to the decreased diffusion path, the coating on the AS80 blanks solidified and roughened in less time and at lower temperatures compared to the AS150 blanks, and a slightly rougher surface was detected for the AS80 samples heated between 700°C and 900°C. *Ex-situ* SEM-EDS measurements showed the propagation of intermetallic compounds through the coating as well as faster diffusion rates and increased oxidation at higher temperatures. Intermetallic compounds reached the surface of the thinner AS80 coating in less time compared to the thicker AS150, highlighting the potential for their use to decrease the amount of time the furnace rollers are susceptible to contamination from the Al-Si coating.

Finally, *in-situ* spectral emittance measurements were also performed on hot stamping blanks in a high-temperature cell connected to an FTIR spectrometer. Despite unreasonable results at lower wavelengths, the results show appropriate trends, demonstrating a distinct decrease in emittance at the initial melting of the coating and an increase shortly thereafter.

From the *ex-situ* reflectance measurements in Chapter 2 and the *in-situ* emittance measurements in this chapter, changes in the chemical composition at the surface of the samples could be detected through peaks in spectroscopic measurements. Chapter 4 will expand upon this concept by using Raman spectroscopy measurements to study the evolution of the Al-Si coating during heating.

Chapter 4

Raman Spectroscopy and Microscopy Measurements

As mentioned in Chapter 1 and Chapter 2, oxidation and intermetallic diffusion occurring at the surface of the Al-Si coating is largely undocumented in literature, but critically influence the degree of molten aluminum transferred to the furnace rollers. Intermetallic compounds can be characterized with *ex-situ* techniques on quenched samples, but these methods are often labour-intensive and destructive to the sample. Moreover, as demonstrated in Chapter 2, quenching and preparing *ex-situ* samples can alter the oxide layer generated during heating. Therefore, this chapter employs *in-situ* and *ex-situ* Raman spectroscopy to assess the chemical development occurring at the surface of the Al-Si coating during heating. Videos of the evolving surface were first captured through *in-situ* microscopy, visualizing the different melting reactions occurring within the coating. *In-situ* Raman spectroscopy showed a spectral signature that changed over key temperature regions during the heating process, which was linked to the restructuring of an oxide layer. Finally, the progression of intermetallic compounds at the surface of the coating was captured through *ex-situ* Raman spectroscopy measurements, providing a simple and effective means of characterizing the chemical structure of the coating with minimal sample preparation. The contents of this chapter have been submitted to “Materials Characterization” for publication in a journal article.

4.1 Principles of Raman Spectroscopy

Raman spectroscopy has been widely utilized as a non-destructive method of classifying materials and identifying chemical reactions [99]. Figure 4-1 shows a schematic of the

Raman scattering process. This technique estimates the vibrational characteristics of a substance by striking a molecule at some base energy state (E_0) with light from a laser at a known frequency (v_L). This excites the molecule to a virtual energy state, and the vibrational frequency or energy shift of the resultant scattered photons is measured as the molecule relaxes to a lower energy state [100]. The majority of scattered photons will not have a frequency shift (*i.e.*, $v_R = v_0$) and the final vibrational energy state of the molecule will be unchanged, which is known as Rayleigh (elastic) scattering. However, if the vibrational frequency of a scattered photon is less than the incident photon ($v_S < v_0$), the vibrational energy state of the molecule will return to a slightly higher level (E_1, where $E_1 - E_0 = h(v_0 - v_S)$ and h is the Planck constant) compared to its initial state, which is known as Stokes scattering. Conversely, if the molecule was initially in an elevated vibrational energy state and relaxes to an energy state that is lower than the initial state, the scattered photon will have a vibrational frequency higher than the incident photon ($v_{AS} < v_0$), which is known as anti-Stokes scattering.

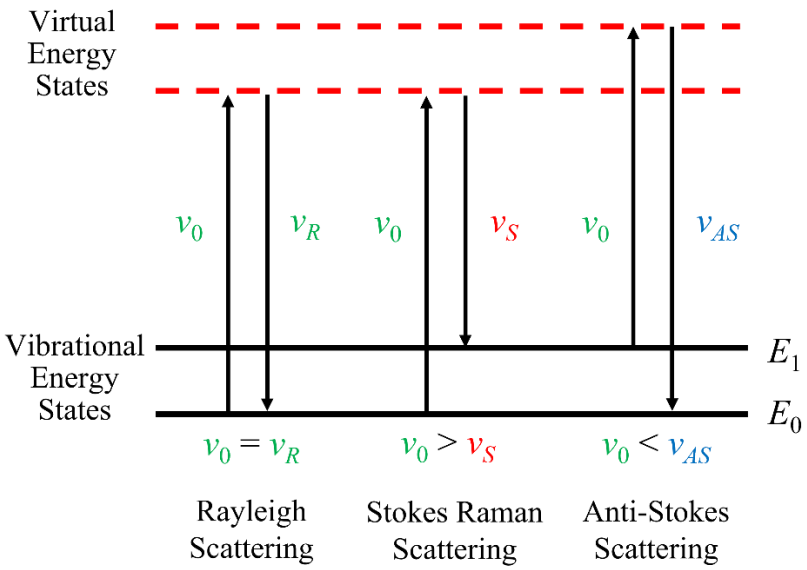

Figure 4-1: Raman scattering energy states schematic.

Molecules of different chemical composition will preferentially scatter photons in the Stokes and anti-Stokes regimes at specific vibrational bands, producing a "fingerprint" and allowing the classification of the material. The vibrational frequency shift spectra are often converted to a Raman shift or Δv [101], where

$$\Delta v = \frac{1}{\nu_L} - \frac{1}{\nu} \quad (18)$$

Raman spectroscopy in the Stokes regime is typically preferred as the likelihood of anti-Stokes scattering is far lower [102], but methods have been devised to increase the sensitivity of anti-Stokes scattering measurements [100].

Finally, as the wavelength of the laser decreases, the efficiency of Raman scattering increases, but fluorescence scattering is more prevalent, which obscures the Raman signal [103]. Fluorescence occurs when an excited molecule more gradually scatters the energy of

incident photons at various energy levels, giving the appearance of Raman scattering, but in reality, the final energy state of the molecule is unaffected [104].

4.2 Experimental Methods

To perform these experiments, a Renishaw® inVia Reflex Raman microscope equipped with WiRe 5.3® software and a 45 W, 532 nm laser was utilized. A schematic of this microscope can be seen in Figure 4-2. After laser light is scattered by the sample surface, it passes through a notch filter that removes Rayleigh scattered light. The remaining scattered light passes through a diffraction grating and into a charge-coupled device (CCD) detector, generating so-called Raman spectra. *In-situ* measurements were performed by heating the samples using a CCR 1000 sample stage from Linkam Scientific®, with either compressed air or 99.998% N_2 gas flowing into the sample chamber, while *ex-situ* samples were placed on a glass slide. Spectral data was averaged from 3 and 10 accumulations for the *in-situ* and *ex-situ* measurements, respectively, with an exposure time of one second for each accumulation. *In-situ* measurements were acquired at intervals of 15 to 25 s. Coupons measuring 38 mm x 38 mm x 1.7 mm were cut from AS150 Usibor® 1500 [3, 10] sheets and used for the *ex-situ* experiments, while 3 mm x 3 mm pieces were removed from these coupons for the *in-situ* tests.

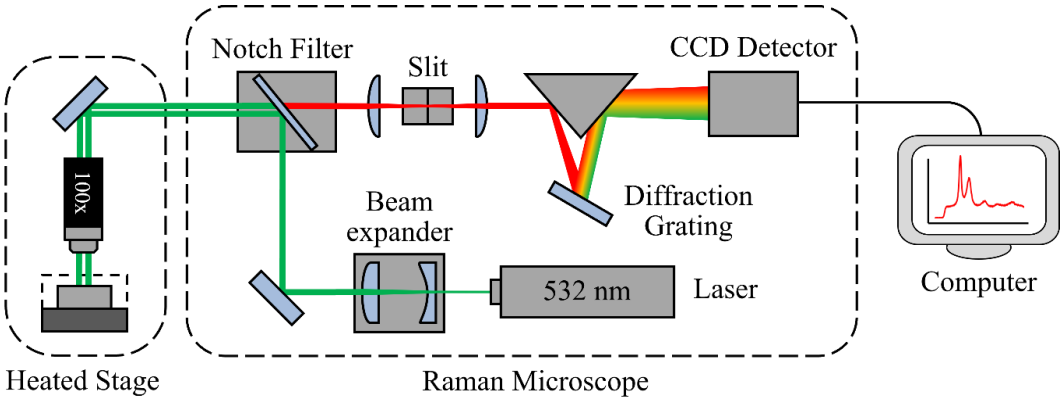

Figure 4-2: Raman spectroscopy measurement schematic.

To visualize the effect of furnace setpoint, blanks were heated at 100°C·min^{-1} and then held at setpoints of 600°C, 630°C, 660°C, 800°C, and 900°C for a total of 10 min. *In-situ* Raman spectra were also acquired for samples heated at 100°C·min^{-1} to 600°C, 700°C, and to 900°C in air, and to 640°C, 700°C, and 900°C in a nitrogen environment. Additional samples were heated to 650°C, 660°C, and 675°C in air to investigate the behaviour of the Raman signal at setpoints near the temperature specified in reaction (4). *Ex-situ* Raman measurements were performed on samples heated in a laboratory-scale muffle furnace at setpoints of 610°C, 618°C, 630°C, 650°C, and 660°C for 4 min and 7 min. For each test, the furnace was soaked for at least 5 min to ensure steady-state operation.

Raman spectra of several oxide powders were also collected for reference measurements. including α-Al_2O_3, (Inframat®, 26R-0803UP), γ-Al_2O_3, (Inframat®, 26R-0842UPGG), and SiO_2 (MSE Supplies®, PO3702). α-Fe_2O_3 samples synthesized at 800°C in dry O_2 according to [105] were used as well. Finally, to link distinct Raman spectra to intermetallic compounds in the Al-Fe-Si system, cross-sections of samples heated at furnace setpoints of 600°C for 16

min and 900°C for 2 min and 5 min were analyzed using SEM-EDS and Raman spectroscopy.

4.3 Results

4.3.1 Visual Surface Evolution

Screen captures of the *in-situ* microscopy videos can be seen in Figure 4-3, with dwell times selected to illustrate clear changes in surface morphology. Samples heated at 600°C are distinctly different than those at higher temperatures in that the surface roughens without showing any intermittent smoothness (Figure 4-3b-Figure 4-3d), showing that the structure is capable of evolving without the complete dissolution of the surface. This observation is consistent with the *in-situ* reflectance and roughness measurements in Chapters 2 and 3, respectively, where two peaks of high reflectance were observed when measuring samples heated above 600°C but only progressive roughening for samples heated to 600°C [48, 69]. A melting event on the surface is evident for all the samples heated to 630°C and above (Figure 4-3e-j), while samples heated between 800°C and 900°C show particularly smooth surfaces followed by significantly rougher surfaces (Figure 4-3k-p). This behaviour indicates that multiple melting transitions occur in the 600-630°C and 630-660°C ranges, agreeing with the reactions proposed by Barreau et al. [39].

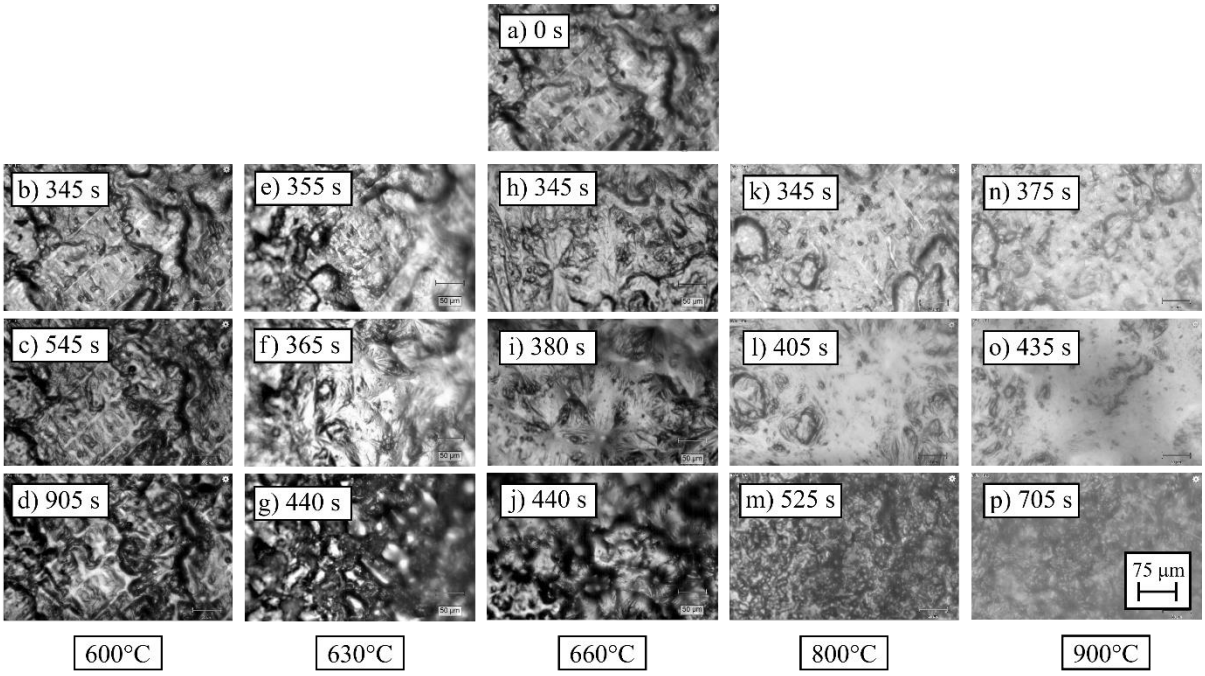

Figure 4-3: Top-view progression of hot stamping samples while heating at 100°C·min^{-1} at 20x magnification. a) As-received (0 s); heating to 600°C for b) 345 s, c) 545 s, and d) 905 s; heating to 630°C for e) 355 s, f) 365 s, and g) 440 s; heating to 660°C for h) 345 s, i) 380 s, and j) 440 s; heating to 800°C for k) 345 s, l) 405 s, and m) 525 s; and heating to 900°C for n) 375 s, o) 435 s, and p) 705 s.

4.3.2 *In-situ* Raman Spectroscopy

In-situ variable temperature Raman spectroscopy performed in air during a heat ramp and dwell time at a set temperature enable the surface composition to be tracked as a function of time and temperature, as shown in Figure 4-4. Initially, Raman spectra match that for silicon [106] at temperatures below 600°C. No defined peaks are observable immediately after melting, but a broad signal that may correspond to fluorescence then emerges near 150 cm^{-1} (Figure 4-4d-f). These ranges are labelled “M” and “F1”, respectively (Figure 4-4a-c). This

peak near 150 cm^{-1} disappears after the dissolution of the coating when heated to 700°C and 900°C but reappears at higher frequencies as time and temperature increase (Figure 4-4e-f). This spectrum is labelled as "F2" (Figure 4-4b-c). From these preliminary measurements, it appears the transition between the F1 and F2 spectra occurs between 600°C and 700°C. To investigate this phenomenon more precisely, measurements at additional setpoint temperatures were performed, as seen in Figure 4.5. The final spectra for the sample heated to 650°C did not resemble the F2 spectra, which started to materialize at the holding temperature of 675°C (Figure 4-5c). Moreover, the final spectra for a sample heated to 660°C (Figure 4-5b) appeared to be in transition between the F1 and F2 spectra. These measurements show that the transition in fluorescence behaviour is likely related to reaction (4) based upon these temperature ranges.

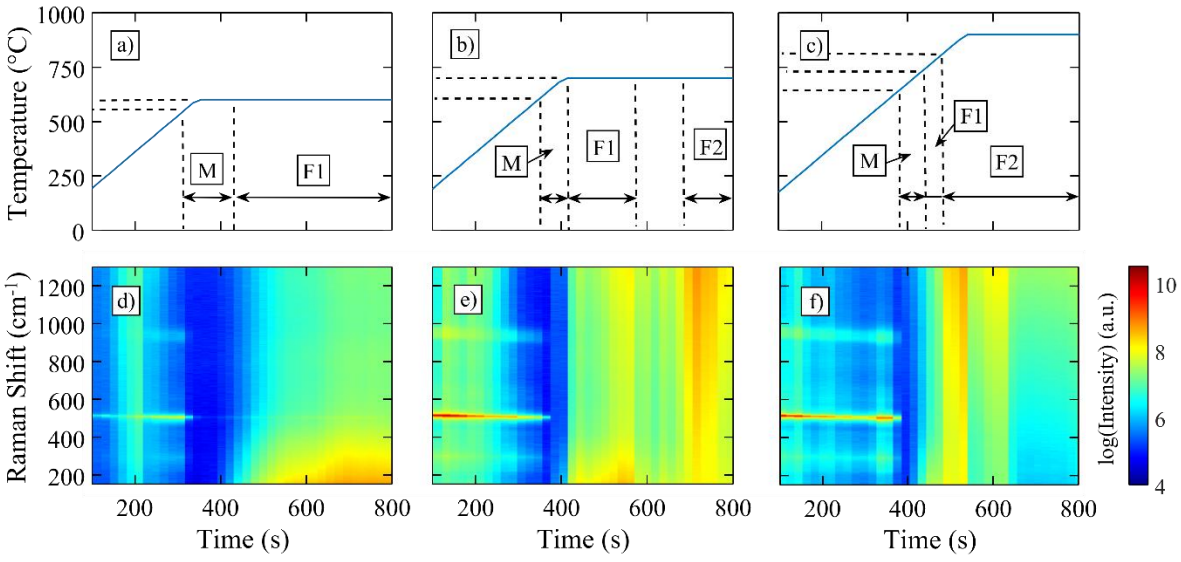

Figure 4-4: Temperature curves for hot stamping samples heated in air at 100°C·min^{-1} to a) 600°C, b) 700°C, and c) 900°C and d-f) their respective *in-situ* Raman signals.

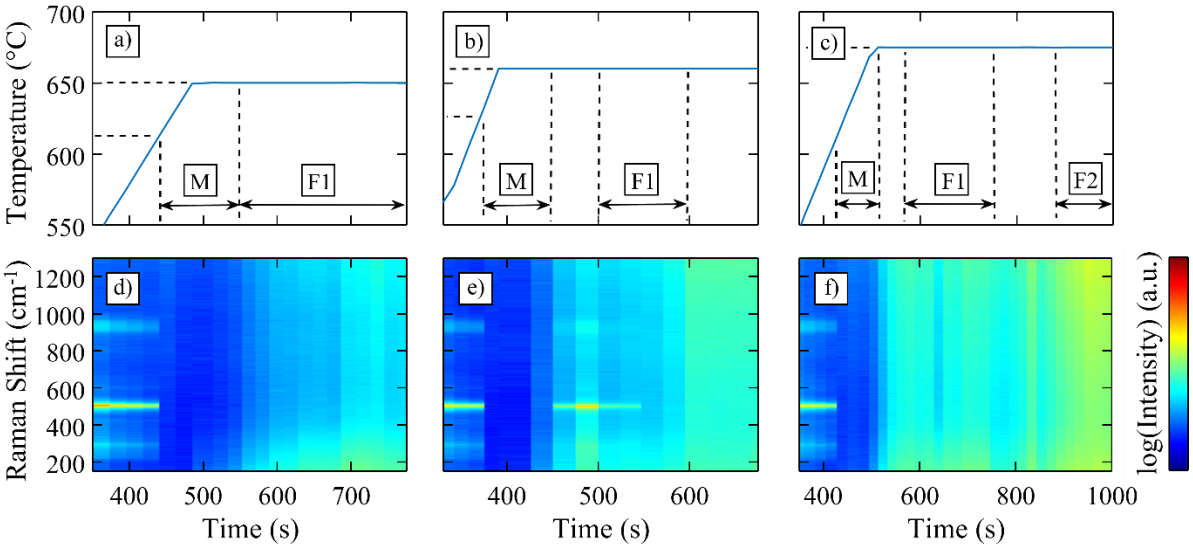

Figure 4-5: Temperature curves for hot stamping samples heated in air at 100°C·min^{-1} to a) 650°C, b) 660°C, and c) 675°C and d-f) their respective *in-situ* Raman signals.

In-situ variable temperature Raman spectroscopy was also performed in a nitrogen environment to illustrate the effect of process environment, as seen in Figure 4-6. Samples were heated at 100°C·min^{-1} and held at setpoints of 640°C (Figure 4-6a), 700°C (Figure 4-6b), and 900°C (Figure 4-6c). Samples exhibit the fluorescence characteristics near 150 cm^{-1}, or F1 spectra, after they are heated for extended dwell times at the 640°C and 700°C setpoints (Figure 4-6d-e), but the sample heated to the 900°C setpoint shows signals resembling the F2 spectra (Figure 4-6f). This behaviour is similar to that seen when heating samples to 900°C under air (Figure 4-4d), but the signals are more intense. The difference in final spectra between the samples heated to 700°C in the air and nitrogen environments (Figure 4-4e and Figure 4-6e) demonstrates that the transition between the F1 and F2 spectra can be pushed to higher temperatures when a reductive atmosphere is utilized. This appears

to indicate that the change in fluorescence behaviour around 655°C is linked to the formation or restructuring of an oxide.

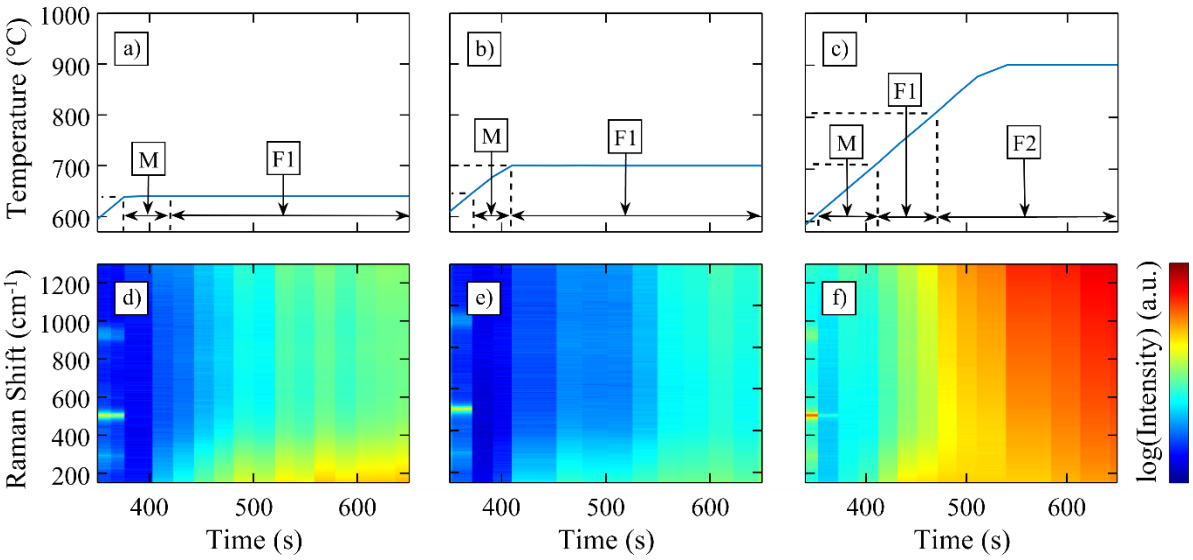

Figure 4-6: Temperature curves for hot stamping samples heated in a nitrogen environment at 100°C·min^{-1} to a) 640°C, b) 700°C, and c) 900°C and d-f) their respective *in-situ* Raman signals.

The observed fluorescence behaviour may indicate the formation of Al_2O_3 on the samples. Molten aluminum rapidly oxidizes in an air environment, and a γ-Al_2O_3 phase will form on aluminum melts for lower superheating temperatures (500-750°C), progress through other metastable Al_2O_3 phases, and then transition to α-Al_2O_3 at higher temperatures (900-1100°C) [107, 108]. Mortenson et al. investigated Al_2O_3 using Raman spectroscopy and noted that small amounts of iron impurities induced strong fluorescence bands up to approximately 2250 cm^{-1} in Raman shift or 582 nm in wavelength [109]. The fluorescence peaks observed here (Figure 4-5 and Figure 4-6) may arise due to leeching of iron from the substrate into Al_2O_3 that forms on the surface. Such fluorescence peaks are problematic for Raman spectroscopy, inhibiting observation of expected vibrational modes. Indeed, the final spectra

in Figure 4-4f and Figure 4-6f are similar to the Raman spectra of α-Al_2O_3 and γ-Al_2O_3 performed by Aminzadeh and Sarikhani-fard with a 514.5 nm laser [110]. Therefore, the transitional nature of the spectra shown in Figure 4-4 and Figure 4-6 could indicate different phases of Al_2O_3 forming at the surface, but further work must be performed to confirm this hypothesis. The ability to characterize the development of the oxide layer *in-situ* using Raman spectroscopy would have significant industrial value as the formation of a robust oxide layer could decrease the transfer of liquid Al-Si to the furnace rollers, as mentioned in Chapter 1 [47].

Because thermal expansion can prevent observation of clear spectral signatures at high temperatures by broadening and shifting Raman peaks, a series of *ex-situ* analyses were performed.

4.3.3 *Ex-situ* Raman Spectroscopy

First, oxide standards relevant to the Al-Fe-Si system, including α-Fe_2O_3, α-Al_2O_3, γ-Al_2O_3, and SiO_2, were measured, all of which typically yield distinct Raman spectra that can be used to fingerprint phases. Raman spectra acquired on these oxides can be seen in Figure 4-7. These results align well with published spectra for α-Fe_2O_3 [111], α-Al_2O_3 [112, 113], and SiO_2 [114], but the peak locations shown for γ-Al_2O_3 were not present in published results [110].

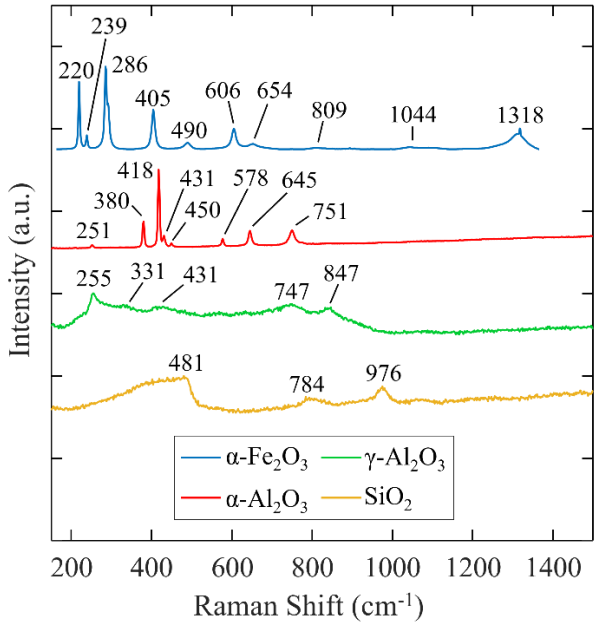

Figure 4-7: *Ex-situ* Raman spectra for α-Fe_2O_3 (Hematite), α-Al_2O_3 (Corundum), γ-Al_2O_3, and SiO_2.

To our knowledge, the Raman spectra of the relevant Al-Fe-Si and Al-Fe intermetallic compounds that can propagate to the surface of hot stamping samples have not been documented in literature. Samples were therefore cross-sectioned after heating and then analyzed by SEM and EDS, followed by Raman microscopy to link Raman spectra to specific intermetallic compounds. The EDS and Raman measurements were not necessarily performed at the same location across the length of the intermetallic layers, but significant variation was not detected in this direction. Heating schedules of 600°C for 16 min and 900°C for 2 min and 5 min produced a variety of intermetallic compounds through the depth of the film, as seen in the SEM micrographs in Figure 4-8.

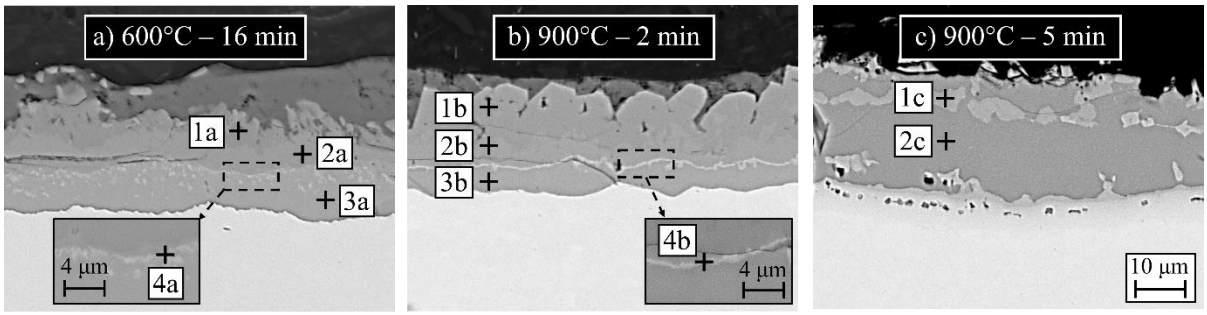

Figure 4-8: Cross-sectional SEM images for samples heated at a) 600°C for 16 min, b) 900°C for 2 min, and c) 900°C for 5 min. Raman spectroscopy and EDS measurements were conducted on the various intermetallic layers.

EDS analysis was used to measure the elemental composition of the sample at selected locations (Table 4-1). The distribution of intermetallic sublayers generally aligns with the results in Figure 2-13 and with those of Grigorieva et al. for the samples heated to 900°C [14], but slightly different compositions were documented at locations 4b and 1c (Figure 4-8). Since the composition of the silicon-rich bands at locations 4a, 4b, and 1c did not align directly with a common Al-Fe-Si compound, a combination of intermetallic compounds was ascribed according to the ternary phase diagram provided by Rivlin et al. [50]. However, because the EDS interaction volume may be larger than these thin layers, the EDS-inferred composition of these areas must be treated with some skepticism. Raman spectra acquired on the layers provide a distribution of peaks between 100 cm^{-1} and 700 cm^{-1} (Table 4-1 and Figure 4-9). Given that Raman spectra are additive, it is notable that the spectra given in Figure 4-9b do not clearly show the strongest peaks of θ or η in Figure 4-9a. The acquisition of distinct Raman signatures for these layers casts further doubts on attributing their composition to a combination of multiple intermetallic compounds. Nevertheless, the assignment of Raman spectra for the intermetallic phases in Figure 4-9a provides a useful

identification tool that can be used to track intermetallic development at the surface of the hot stamping samples when analyzed at room temperature.

Table 4-1: EDS measurements and Raman spectra for the various intermetallic layers shown in Figure 4-8.

Heating Profile	Location	Composition (at.%)			Compound Identification	Raman Shift Peak Locations (cm^{-1})
		Al	Fe	Si		
600°C 16 min	1a	73.3	13.0	13.7	τ_6	184, 236, 250, 297, 340, 408
	2a	68.5	19.0	12.5	τ_5	131, 157, 203, 238, 272, 317, 404, 434
	3a	69.1	27.4	3.5	η	246, 272, 319, 362
	4a	59.6	26.8	13.6	$\tau_1 + \tau_2 + \theta$	134, 308, 392
900°C 2 min	1b	69.0	19.7	11.3	τ_5	130, 154, 206, 240, 272, 319, 402, 439
	2b	69.4	23.7	6.9	θ	123, 172, 223, 250, 267, 383, 439
	3b	70.0	28.5	4.5	η	248, 282, 321, 366
	4b	57.4	30.3	12.3	$\tau_1 + \theta + \eta$	180, 192, 244, 348, 421
900°C 5 min	1c	44.1	35.9	20.0	$\tau_1 + \eta$	186, 228, 267, 284, 366
	2c	66.1	29.0	4.9	η	243, 332, 352

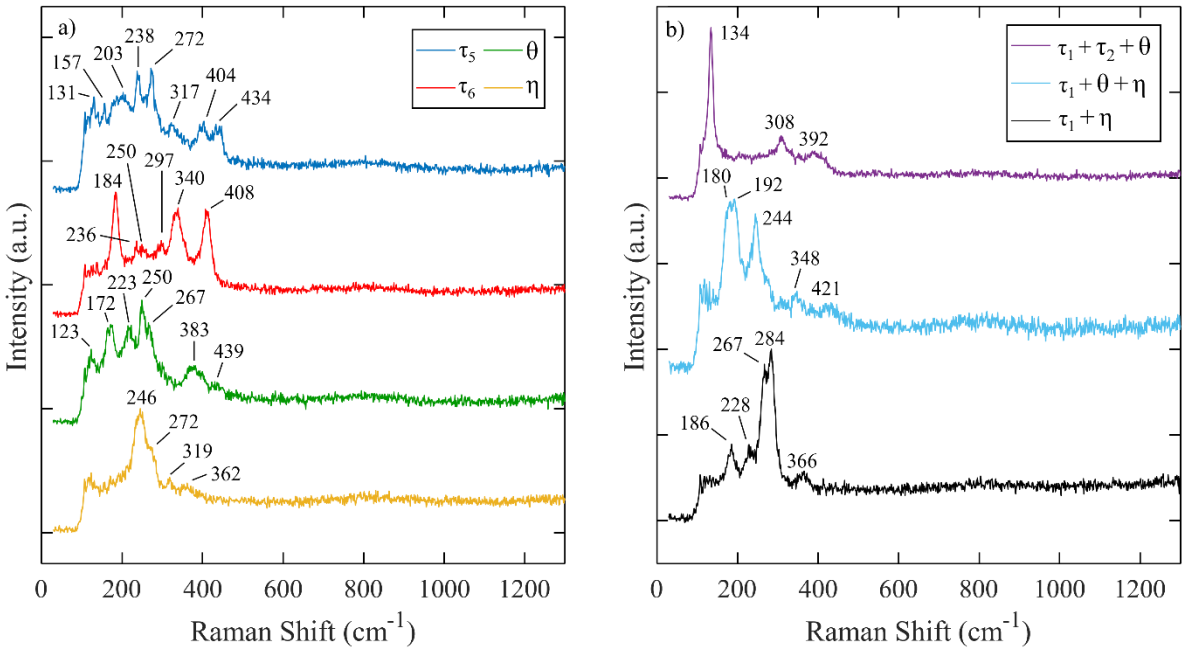

Figure 4-9: Raman spectroscopy signals for a) the intermetallic compounds confirmed by EDS and b) possible intermetallic combinations as determined from the ternary phase diagram given by Rivlin et al. [50].

Using these fingerprints, precision *ex-situ* measurements were performed on samples heated at furnace setpoints near the temperatures specified for reactions (1)-(4), allowing the unique features of the samples to be probed. The final surface state for two dwell times and multiple holding temperatures can be seen in Figure 4-10, with identified intermetallic compounds labelled on the figure. A stark difference in surface state can be detected between the 618°C and 630°C holding temperatures at both dwell times, as well as between the 650°C and 660°C holding temperatures when heated for 7 min. The change in surface chemistry between the 4 min and 7 min measurements suggests that the samples heated for 4 min provides a measure of intermetallics formed at the surface, while those heated for 7 min contain intermetallic compounds arising from diffusion of iron from the base steel to the top

of the coating. Spectra acquired for samples heated for 4 min resemble τ_6 for the lower furnace setpoints, before transitioning to a weak τ_5 signal for the sample heated to 630°C. No clear intermetallic signature was detected for setpoints of 650°C and 660°C. It is possible that a large-scale transition from τ_6 to τ_5 is shifted to higher temperatures due to the short amount of time held above the temperature prescribed in reaction (3). Samples heated for 7 min show only τ_6 at the surface for the sample heated to 610°C, which is replaced by τ_5 for all samples heated between 618°C to 660°C. These results align well with the temperature given in reaction (2). Finally, local α-Fe_2O_3 compounds were detected on the samples shown in Figure 4-10c-e, g, and i.

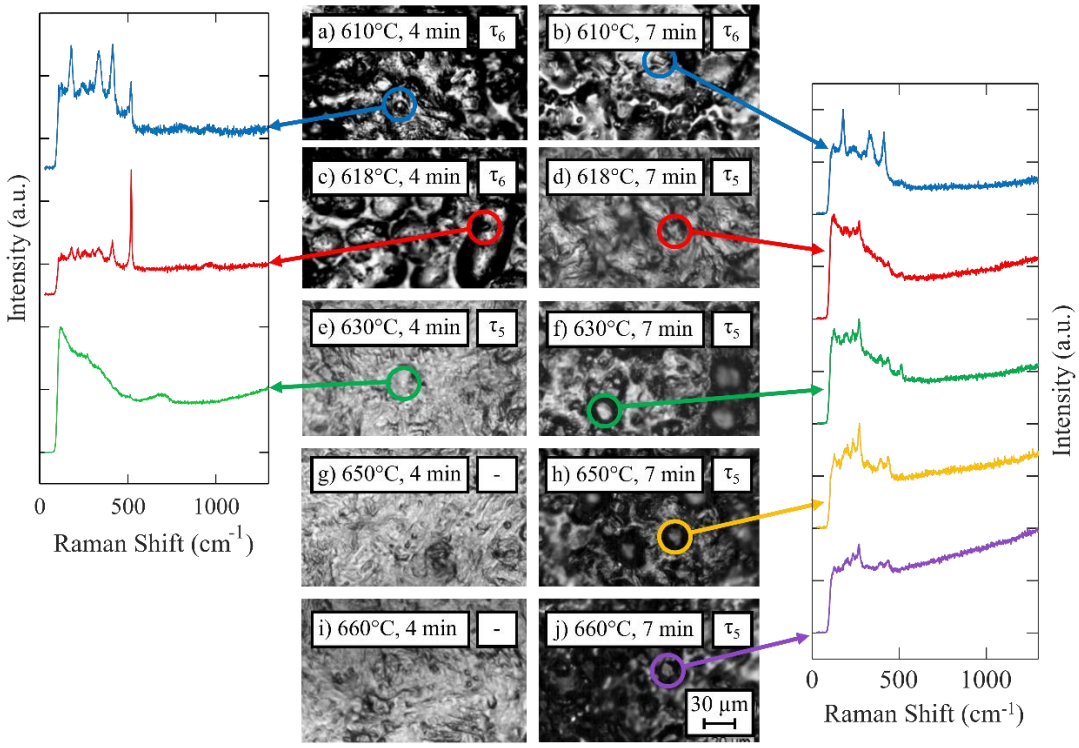

Figure 4-10: Surface state progression between 610°C and 660°C at 20x magnification for samples heated to 610°C for a) 4 min and b) 7 min; 618°C for c) 4 min and d) 7 min; 630°C for e) 4 min and f) 7 min; 650°C for g) 4 min and h) 7 min; and 660°C for i) 4 min and j) 7 min. Detected intermetallic spectra are depicted in the side panels.

It is important to note that these results show additive signals in some cases. For example, a strong silicon peak at 520 cm^{-1} is present for the samples in Figure 4-10a and Figure 4-10c, indicating that the surface is still comprised of some aggregate Si compounds in addition to the detected τ_6 phases. The measurements in Figure 4-10d-f show the presence of the F1 fluorescence signal while the spectrum in Figure 4-10j resembles the F2 fluorescent signal from Figure 4-4 and Figure 4-6. This is consistent with the temperature ranges in which these fluorescent spectra were acquired. However, the mixing of intermetallic spectra was not detected for measurements at the surface or in the intermetallic sublayers on cross-sectional

samples. Therefore, the inclusion of multiple phases or lack thereof can be reported with a higher degree of confidence using Raman spectroscopy compared to EDS.

These results illustrate the clear benefit of using Raman spectroscopy to characterize the development of Al-Si coatings compared to other methods in literature. With minimal sample preparation time, a single measurement can isolate individual intermetallic phases at the surface or from a cross-sectional perspective. Moreover, the *in-situ* development of an oxide layer at the surface of the coating could also be easily assessed, but external measurements like X-ray diffraction should be performed to verify this process.

4.4 Summary

This chapter documents the first investigation of the evolution of the Al-Si coating on 22MnB5 steel using Raman spectroscopy. *In-situ* microscopy conducted on samples held at different furnace setpoint temperatures showed multiple temperature-dependent melting reactions occurring between 577°C and 655°C. Moreover, *in-situ* Raman spectroscopy in air and nitrogen environments displayed changes in fluorescence behaviour in the Raman spectra at elevated temperatures, indicating temperature stages related to the development of an oxide layer. *Ex-situ* Raman measurements performed on cross-sectioned samples cooled to room temperature after heating yielded a variety of unique spectra, which were linked to specific intermetallic compounds using SEM-EDS. This allowed intermetallics to be fingerprinted at the surface of samples and the prevalence of certain intermetallic compounds at different temperature setpoints and dwell times to be documented. The results provide valuable data to furnace operators on the development of the Al-Si coating and a powerful

technique to easily assess the composition of compounds at the surface of hot stamping blanks during heating.

Chapter 5

Conclusions

5.1 Summary of Thesis

Hot stamping has emerged as a mainstay technique to produce strong and reliable automotive parts while reducing vehicle weight. This process commonly involves heating aluminum-silicon coated 22MnB5 steel blanks in a roller hearth furnace before quenching them in a forming die. However, the melting and transformation of the coating at elevated temperatures causes molten aluminum to transfer to the furnace rollers and the radiative properties of the blanks to vary drastically during heating. As few studies document the liquid regime of the coating, this work uses a combination of *in-situ* and *ex-situ* techniques with industrially-relevant heating methods to discover new insights regarding the coating transformation process.

In-situ laser reflectance tests revealed that the liquefication of the Al-Si coating occurred in multiple stages that were dependent on temperature and heating rate. It was also confirmed through SEM-EDS measurements that intermittent solidification between two main melting regimes was caused by surface oxidation, before intermetallic diffusion completely transformed the Al-Si coating into multiple Al-Fe-Si intermetallic sublayers. Information about the structure and composition of the surface could be inferred through inflection points in *ex-situ* reflectance spectra. Specifically, oscillations, or lack thereof, in the near infrared were linked to the development of a thin oxide layer, which was confirmed through high-magnification SEM images.

Additional *in-situ* analyses were performed to acquire quantitative measurements of the development of the Al-Si coating during heating. *In-situ* roughness profiles were generated through statistical approximations of images taken of scattered light from the surfaces of the blanks. These results mirrored the *in-situ* reflectance tests, but demonstrated that samples heated at higher temperatures showed significantly rougher surfaces, despite the complete intermetallic transformation of the coating in all cases. It was also documented that blanks with a thinner coating produced slightly rougher surfaces after heat treatment. *In-situ* spectral emittance measurements showed sharp decreases and increases at the melting and resolidification of the coating, respectively, but their accuracy and usefulness were hampered by deficiencies in the experimental setup.

Moreover, Raman spectroscopy measurements yielded important insight into the chemical development of the Al-Si coating during heating. Distinct Raman spectra emerged in specific temperature regions, indicating the formation and restructuring of an oxide layer after melting reactions within the coating. Intermetallic propagation was also documented through precise *ex-situ* measurements, generating unique Raman spectra for several important intermetallic compounds in the Al-Fe-Si system.

5.2 Future Work

This work enhances the knowledge-base available to furnace operators regarding the evolution of the Al-Si coating during heating, and provides industry with specialized diagnostic methods, allowing them to make better-informed decisions about process parameters such as blank heating schedule, coating thickness, etc. This work also serves as a

foundation for additional research that could lead to further improvements to the hot stamping process.

Firstly, coating liquefication should be directly related to coating transfer by measuring the deposits left on the furnace rollers. As specific heating parameters increase the degree of aluminum transfer, problematic temperature regions and melting reactions will be isolated. Investigating blanks with different coating weights would be useful to investigate if coating transfer is inversely proportional to coating thickness due to the decreased liquid window.

These efforts would be aided by improved Raman spectroscopy techniques. In Chapter 4, it was hypothesized that the observed fluorescence behaviour was linked to the restructuring of an oxide. Future work will confirm this, and the identity of the oxide phases in question. This could be done by using transmission electron microscopy, x-ray diffraction, fluorometry, or more intensive chemical analysis techniques. More detailed Raman spectroscopy measurements on the intermetallic compounds present at the surface could refine the reaction scheme covering the dissolution and resolidification of the Al-Si coating.

Finally, the *in-situ* emittance measurements must be improved before they can be used in thermal models. Although difficult to locate, more standards with known spectral emittances could be acquired to verify the signal from the HTHP cell. The maximum temperature and heating rate of the heating block should be upgraded to resemble realistic heating curves utilized by industry. Once a reliable method for measuring the radiative properties has been established, the heating conditions could be carefully adjusted to optimize the heat absorptance of the hot stamping blanks, thereby saving industrial time and resources.

References

[1] P. K. Mallick, Materials, Design, and Manufacturing for Lightweight Vehicles (2nd Ed.), Amsterdam: Elsevier, 2021.

[2] H. Karbasian and A. E. Tekkaya, "A review on hot stamping," *Journal of Materials Processing Technology*, vol. 210, pp. 2103-2118, 2010.

[3] ArcelorMittal, "Steels for hot stamping - Usibor® and Ductibor®," 5 January 2022. [Online]. Available: https://automotive.arcelormittal.com/products/flat/PHS/usibor_ductibor.

[4] B. Çetin and H. Meço, "Metallurgy of Steels," in *Hot Stamping of Ultra High-Strength Steels*, Cham, Springer, 2019, pp. 19-29.

[5] M. Merklein, M. Wieland, M. Lechner, S. Bruschi and A. Ghiotti, "Hot stamping of boron steel sheets with tailored properties: A review," *J. Mater. Process. Technol.*, vol. 228, pp. 11-24, 2016.

[6] M. Verma, H. Yan, J. Culham, M. Di Ciano and K. Daun, "Development and Validation of a Thermometallurgical Model for Furnace-Based Austenitization During Hot Stamping," *Journal of Heat Transfer*, vol. 141, pp. 1-10, 2019.

[7] J. Freudenberger, J. Göllner, M. Heilmaier, G. Mook, H. Saage, Vivek Srivastava and U. Wendt, "Materials Science and Engineering," in *Handbook of Mechanical Engineering*, Würzburg, Springer, 2008, pp. 75-222.

[8] M. Zhang, Q. Li, K. Han, C. Huang, R. Wu, R. Fu, L. Li, Z. Wan and B. Sun, "Continuous Cooling Transformation Diagram and Properties of Hot Forming Steel," *Applied Mechanics and Materials*, Vols. 152-154, pp. 585-588, 2012.

[9] M. Di Ciano, N. Field, M. A. Wells and K. J. Daun, "Development of an Austenitization Kinetics Model for 22MnB5 Steel," *Journal of Materials Engineering and Performance*, vol. 27, no. 4, pp. 1792-1802, 2018.

[10] ArcelorMittal, "Steels coated with Alusi®, an aluminium-silicon alloy," 28 December 2021. [Online]. Available: https://automotive.arcelormittal.com/products/flat/coatings/alusi.

[11] D. W. Fan and B. C. de Cooman, "State-of-the-Knowledge on Coating Systems for Hot Stamped Parts," *Steel Research International,* vol. 83, no. 5, pp. 412-433, 2012.

[12] W.-J. Cheng and C.-J. Wang, "Effect of silicon on the formation of intermetallic phases in aluminide coating on mild steel," *Intermetallics,* vol. 19, pp. 1455-1460, 2011.

[13] W.-J. Cheng and C.-J. Wang, "Microstructural evolution of intermetallic layer in hot-dipped aluminide mild steel with silicon addition," *Surface & Coatings Technology,* vol. 205, pp. 4726-4731, 2011.

[14] R. Grigorieva, P. Drillet, J.-M. Mataigne and A. Redjaïmia, "Phase transformations in the Al-Si coating during the austenitization step," *Solid State Phenomena,* Vols. 172-174, pp. 784-790, 2011.

[15] D. Shin, J.-Y. Lee, H. Heo and C.-Y. Kang, "TEM Microsctructural evolution and Formation Mechanism of Reaction Layer for 22MnB5 Steel Hot-Dipped in Al-10% Si," *Coatings,* vol. 8, pp. 467-480, 2018.

[16] M. Kolaříková, R. Chotěborský, M. Hromasov and M. Linda, "The characteristics of Al-Si coating on steel 22MnB5 depending on the heat treatment," *Acta Polytechnica,* vol. 59, no. 4, pp. 351-357, 2019.

[17] W. Liang, W. Tao and Y. Zhang, "Influence of heating parameters on properties of the Al-Si coating applied to hot stamping," *Science China Technological Sciences,* vol. 60, no. 7, pp. 1088-1102, 2017.

[18] P. Orozco-González, M. Castro-Román, S. Maldonado-Ruíz, S. Haro-Rodríguez, F. Equihua-Guillén, R. Muñiz-Valdez, S. Luna-Álvarez, M. Montoya-Dávilla and A. Hernández-Rodríguez, "Nucleation of Fe-Rich Intermetallic Phases on α-Al_2O_3 Oxide Films in Al-Si Alloys," *Journal of Minerals and Materials Characterization and Engineering,* vol. 3, pp. 15-25, 2015.

[19] N. Krendelsberger, F. Weitzer and J. C. Schuster, "On the Reaction Scheme and Liquidus Surface in the Ternary System Al-Fe-Si," *Metallurgical and Materials Transactions A,* vol. 38, no. 8, pp. 1681-1691, 2007.

[20] T. I. Yanson, M. B. Manyako, O. I. Bodak, N. V. German, O. S. Zarechnyuk, Č. Radovan, J. V. Pacheco and K. Yvon, "Triclinic $Fe_3Al_2Si_3$ and Orthorhombic $Fe_3Al_2Si_4$ with New Structure Types," *Acta Crystallographica,* vol. C52, no. 12, pp. 2964-2967, 1996.

[21] R. N. Corby and P. J. Black, "The Structure of α-(AlFeSi) by Anomalous-Dispersion Methods," *Acta Crystallographica,* vol. B33, no. 11, pp. 3468-3475, 1977.

[22] C. Rømming, V. Hansen and J. Gjønnes, "Crystal Structure of ß-$Al_{4.5}$FeSi," *Acta Crystallographica,* vol. B50, no. 3, pp. 307-312, 1994.

[23] M. Mihalkovič and M. Widom, "Structure and stability of Al_2Fe and Al_5Fe_2: First-principles total energy and phonon calculations," *Physical Review B,* vol. 85, p. 014113, 2012.

[24] P. J. Black, "The Structure of $FeAl_3$. I," *Acta Crystallographica,* vol. 8, no. 1, pp. 43-48, 1955.

[25] K. Schubert, U. Rösler, M. Kluge, K. Anderko and L. Härle, "Kristallographische Ergebnisse an Phasen mit Durchdringungsbindung," *Naturwissenschaften,* vol. 40, no. 16, p. 437, 1953.

[26] R. N. Corby and P. J. Black, "The Structure of $FeAl_2$ by Anomalous Dispersion Methods," *Acta Crystallographica,* vol. B29, no. 12, pp. 2669-2677, 1973.

[27] J. L. Murray and A. J. McAlister, "The Al-Si (Aluminum-Silicon) System," *Bulletin of Alloy Phase Diagrams,* vol. 5, no. 1, pp. 74-84, 1984.

[28] R. Kolleck, R. Veit, M. Merklein, J. Lechler and M. Geiger, "Investigation of induction heating for hot stamping of boron alloyed steels," *CIRP Annals,* vol. 57, no. 1, pp. 275-278, 2009.

[29] S. J. Grauer, E. J. F. R. Caron, N. L. Chester, M. A. Wells and K. J. Daun, "Investigation of melting in the Al-Si coating of a boron steel sheet by differential scanning calorimetry," *Journal of Materials Processing Technology,* vol. 216, pp. 89-94, 2015.

[30] K. S. Jhajj, S. R. Slezak and K. J. Daun, "Inferring the specific heat of an ultra high strength steel during the heating stage of hot forming die quenching, through inverse analysis," *Applied thermal Engineering,* vol. 83, pp. 98-107, 2015.

[31] Z. Gui, W. Liang and Y. Zhang, "Enhancing ductility of the Al-Si coating on hot stamping steel by controlling the Fe-Al phase transformation during austenitization," *Science China Technological Sciences*, vol. 57, no. 9, pp. 1785-1793, 2014.

[32] K. Wang, Z. Gui, P. Liu, Y. Wang and Y. Zhang, "Cracking behavior of Al-Si coating on hot stamping boron steel sheet," *Proceedia Engineering*, vol. 81, pp. 1713-1718, 2014.

[33] O. Sherepenko, V. Schreiber, I. Schischin, M. Wohner, P. Wernlein, N. Mitzschke and S. Jüttner, "Influence of surface layers on resistance spot joinability of partially hardened steel 22MnB5 with aluminum-silicon and zinc coatings," *Welding in the World*, vol. 64, pp. 755-771, 2020.

[34] A. Chiocca and Z. Wang, "Impact of Heat-Treatment Conditions on Spot Weldability of Usibor®1500-AS and Ductibor®1000-AS," in *Sheet Metal Welding Conference XIX*, Livonia, 2021.

[35] L. Dosdat, J. Petitjean, T. Vietoris and O. Clauzeau, "Corrosion Resistance of Different Metallic Coatings on Press-Hardened Steels for Automotive," *Steel Research International*, vol. 82, no. 6, pp. 726-733, 2011.

[36] C. Allély, L. Dosdat, O. Clauzeau, K. Ogle and P. Voloitch, "Anticorrosion mechanisms of aluminized steel for hot stamping," *Surface and Coatings Technology*, vol. 238, pp. 188-196, 2014.

[37] L. Pelcastre, J. Hardell, A. Rolland and B. Prakash, "Influence of microstructural evolution of Al-Si coated UHSS on its tribological behaviour against tool steel at elevated temperatures," *Journal of Materials Processing Technology*, vol. 228, pp. 117-124, 2016.

[38] F. Jenner, M. E. Walter, R. M. Iyengar and R. Hughes, "Evolution of Phases, Microstructure, and Surface Roughness during Heat Treatment of Aluminized Low Carbon Steel," *Metallurgical and Materials Transactions A*, vol. 41A, pp. 1554-1563, 2010.

[39] M. Barreau, C. Méthivier, T. Sturel, C. Allely, P. Drillet, S. Cremel, R. Grigorieva, B. Nabi, R. Podor, J. Lautru, V. Humblot, J. Landoulsi and X. Carrier, "In situ surface imaging: High

temperature environmental SEM study of the surface changes during heat treatment of an Al-Si coated boron steel," *Materials Characterization,* vol. 163, pp. 1-13, 2020.

[40] C.-J. Wang and S.-M. Chen, "The high-temperature oxidation behavior of hot-dipping Al-Si coating on low carbon steel," *Surface & Coatings Technology,* vol. 200, pp. 6601-6605, 2006.

[41] I.-Y. Sohn, H.-S. Hwang, J.-W. K. D. Choi, Y.-R. Cho and J. S. Kim, "Characteristic comparison for coated HPF steels," in *Hot Sheet Metal Forming of High-Performance Steel*, Toronto, 2015.

[42] D. W. Fan, H. S. Kim, J.-K. Oh, K.-G. Chin and B. C. De Cooman, "Coating Degradation in Hot Press Forming," *ISIJ International,* vol. 50, pp. 561-568, 2010.

[43] C. Shi, K. J. Daun and M. A. Wells, "Spectral emissivity characteristics of the Usibor 1500P steel during austenitization in argon and air atmospheres," *International Journal of Heat and Mass Transfer,* vol. 91, pp. 818-828, 2015.

[44] M. Windmann, A. Röttger and W. Theisen, "Phase formation at the interface between a boron alloyed steel substrate and an Al-rich coating," *Surface & Coatings Technology,* vol. 226, pp. 130-139, 2013.

[45] M. Jönsson, "The Problem with Melted Al-Si in the Hot Stamping Furnace," in *International Conference on Advanced high Strength Steel and Press Hardening*, Xi'an, 2017.

[46] H. Lehmann, A. V. Starck, A. Muhlbauer and C. Kramer, "Rollenherdöfen für die Wärmbehandlung beim Presshärten," *Praxishandbuch Thermoprozesstechnik 2,* vol. 2, 2011.

[47] F. Luther, H. Hartmann, M. Debeaux, C. Fritzsche, O. Strauß, M. Graul, K. Krüger, J. Laß, S. Mütze and T. Koll, "Extended Aluminium-Silicon Coating Concept with Improved Properties for Existing Hot Forming Applications," in *Hot Sheet Metal Forming of High-Performance Steel (CHS2)*, Luleå, 2019.

[48] C. M. Klassen and K. J. Daun, "Investigating coating liquefaction and solidification of furnace-heated Al-Si coated 22MnB5 steel using laser reflectance," *Surface and Coatings Technology,* vol. 393, pp. 1-9, 2020.

[49] C. M. Klassen and K. J. Daun, "Investigating the oxidation of Al-Si coated 22MnB5 steel during heating with reflectance measurements," in *Accepted for Hot Sheet Metal Forming of High-Performance Steel*, Barcelona, 2022.

[50] V. G. Rivlin and G. V. Raynor, "Critical evaluation of consitution of aluminium-iron-silicon system," *International Metals Reviews,* vol. 3, pp. 133-152, 1981.

[51] D. Y. Smith, E. Shiles and M. Inokuti, "The Optical Properties of Metallic Aluminum," in *Handbook of Optical Constants of Solids*, Academic Press, 1997, pp. 369-406.

[52] J. R. Howell, Thermal Radiation Heat Transfer, 6th Ed., Boca Raton: CRC Press, 2016.

[53] H. Ehrenreich, H. R. Philipp and B. Segall, "Optical Properties of Aluminum," *Physical Review,* vol. 132, no. 5, pp. 1918-1928, 1963.

[54] K. Lin and K. J. Daun, "Interpreting the spectral reflectance of advanced high strength steels using the Davies' model," *Journal of Quantitative Spectroscopy and Radiative Transfer,* vol. 242, p. 106796, 2020.

[55] L. del Campo, R. B. Pérez-Sáez and M. J. Tello, "Iron oxidation kinetics study by using infrared spectral emissivity measurements below 570°C," *Corrosion Science,* vol. 50, pp. 194-199, 2008.

[56] F. Zhang, K. Yu, K. Zhang, Y. Liu, Y. Zhao and Y. Liu, "Infrared Spectral Emissivity Property of Pure Titanium in the 473-1035 K Temperature Range," *Applied Spectroscopy,* vol. 70, no. 10, pp. 1717-1725, 2016.

[57] K. Zhang, L. Yu, Y. Liu and Y. Zhao, "Effect of surface oxidation on emissivity properties of pure aluminum in the near infrared region," *Materials Research Express,* vol. 4, p. 086501, 2017.

[58] F. Gervais, "Aluminum Oxide (Al_2O_3)," in *Handbook of Optical Constants of Solids*, Academic Press, 1998, pp. 761-775.

[59] T. Makino, O. Sotokawa and Y. Uwata, "Transient behaviors in thermal radiation characteristics of heat-resisting metals and alloys in oxidation processes," *International Journal of Thermophysics*, vol. 9, pp. 1121-1130, 1988.

[60] K. Yu, H. Zhang, Y. Liu and Y. Liu, "Study of normal spectral emissivity of copper during thermal oxidation at different temperatures and heating times," *International Journal of Heat and Mass Transfer*, vol. 129, pp. 1066-1074, 2019.

[61] R. D. Jones and R. W. Richards, "Measurement of the reflectivity changes occurring in coated steels on elevated temperature exposure," *High Temperature Technology*, vol. 6, no. 1, pp. 17-22, 1988.

[62] N. L. Chester, M. A. Wells and K. J. Daun, "Experimental Measurements of Spectral Emissivity of Al-Si Coated Steel Blanks Undergoing Rapid Heating," *Proceedings of the ASME 2014 International Mechanical Engineering Congress and Exposition*, vol. 8A, pp. 1-7, 2014.

[63] T. A. Blake, T. J. Johnson, R. G. Tonkyn, B. M. Forland, T. L. Myers, C. S. Brauer, Y.-F. Su, B. E. Bernacki, L. Hanssen and G. Gonzalez, "Methods for quantitative infrared directional-hemispherical and diffuse reflectance measurements using an FTIR and a commercial integrating sphere," *Applied Optics*, vol. 57, no. 3, pp. 432-446, 2018.

[64] Labsphere, "Reflectance Materials and Coatings," [Online]. Available: https://www.labsphere.com/support/system-product-brochures/. [Accessed 11 August 2021].

[65] M. Pourmajidian, B. Langelier and J. R. McDermid, "Effect of Process Atmosphere Dew Point and Tin Addition on Oxide Morphology and Growth for a Medium-Mn Third Generation Advanced Steel During Intercritical Annealing," *Metallurgical and Materials Transactions A*, vol. 49A, pp. 5561-5573, 2018.

[66] C.-D. Wen and I. Mudawar, "Modeling the effects of surface roughness on the emissivity of aluminum alloys," *International Journal of Heat and Mass Transfer*, vol. 49, pp. 4279-4289, 2006.

[67] C. Shi, K. J. Daun and M. A. Wells, "Evolution of the Spectral Emissivity and Phase Transformations of the Al-Si Coating on Usibor® 1500P Steel During Austenitization," *Metallurgical and Materials Transactions B,* vol. 47B, pp. 3301-3309, 2016.

[68] F. Borsetto, A. Ghiotti and S. Bruschi, "Investigation of the high strength steel Al-Si coating during hot stamping operations," *Key Engineering Materials,* Vols. 410-411, pp. 289-296, 2009.

[69] C. M. Klassen, J. Emmert and K. J. Daun, "Effect of coating thickness on the in-situ reflectance and surface roughness of Al-Si coated 22MnB5 steel," *Surface & Coatings Technology,* vol. 414, p. 127100, 2021.

[70] Y. Chang, X. Tang, K. Zhao, P. Hu and Y. Wu, "Investigation of the factors influencing the interfacial heat transfer coefficient in hot stamping," *Journal of Materials Processing Technology,* vol. 228, pp. 25-33, 2016.

[71] X. Tian, Y. Zhang and J. Li, "Investigation on Tribological Behavior of Advanced High Strength Steels: Influence of Hot Stamping Process Parameters," *Tribology Letters,* vol. 45, pp. 489-495, 2012.

[72] M. Suehiro, J. Maki, K. Kusumi, M. Ohgami and T. Miyakoshi, "Properties of Aluminized Steels for Hot-Forming," in *International Body Engineering Conference & Exposition*, Chiba, 2003.

[73] O. L. Ighodaro, E. Biro and Y. N. Zhou, "Comparative effects of Al-Si and galvannealed coatings on the properties of resistance spot welded hot stamping steel joints," *Journal of Materials Processing Technology,* vol. 236, pp. 64-72, 2016.

[74] A. Ghiotti, S. Bruschi and F. Borsetto, "Tribological characteristics of high strength steel sheets under hot stamping conditions," *Journal of Materials Processing Technology,* vol. 211, pp. 1694-1700, 2011.

[75] R. Podor, X. Le Goff, J. Lautru, H.-P. Brau, M. Barreau, X. Carrier, J. Mendonça, D. Nogues and A. Candeias, "Direct Observation of the Surface Topography at High Temperature with SEM," *Microscopy and Microanalysis,* vol. 26, no. 3, pp. 397-402, 2020.

[76] J. W. Goodman, "Some fundamental properties of speckle," *Journal of the Optical Society of America,* vol. 66, no. 11, pp. 1145-1150, 1976.

[77] L. I. Goldfischer, "Autocorrelation Function and Power Spectral Density of Laser-Produced Speckle Patterns," *Journal of the Optical Society of America,* vol. 55, no. 3, pp. 247-253, 1965.

[78] U. Persson, "Real Time Measurement of Surface Roughness on Ground Surface Using Speckle-Contrast Technique," *Optics and Lasers in Engineering,* vol. 17, pp. 61-67, 1992.

[79] H. Fujii and T. Asakura, "Roughness measurements of metal surfaces using laser speckle," *Journal of the Optical Society of America,* vol. 67, no. 9, pp. 1171-1176, 1977.

[80] E. Kayahan, H. Oktem, F. Hacizade, H. Nasibov and O. Gundogdu, "Measurement of surface roughness of metals using binary speckle image analysis," *Tribology International,* vol. 43, pp. 307-311, 2010.

[81] J. B. Meireles, L. da Silva, D. P. Caetano and J. A. O. Huguenin, "Effect of metallic surface roughness on the speckle pattern formation at diffraction plane," *Optics and Lasers in Engineering,* vol. 50, pp. 1731-1734, 2012.

[82] D. Xu, Q. Yang, F. Dong and S. Krishnaswamy, "Evaluation of surface roughness of a machined metal surface baed on laser speckle pattern," *The Journal of Engineering,* vol. 2018, no. 9, pp. 773-778, 2018.

[83] C. M. Klassen, J. Emmert and K. J. Daun, "Inferring the surface roughness of Al-Si coated 22MnB5 steel using an in situ laser speckle characterization technique," in *International Deep Drawing Research Group 39th Annual Conference,* Seoul, 2020.

[84] L. del Campo, R. B. Pérez-Sáez, M. J. Tello, X. Esquisabel and I. Fernández, "Armco Iron Normal Spectral Emissivity Measurements," *International Journal of Thermophysics,* vol. 27, no. 4, pp. 1160-1172, 2006.

[85] J. D. Dai, X. Wang and G. Yuan, "Fourier Transform Spectrometer for Spectral Emissivity Measurement in the Temperature Range between 60 and 1500°C," *Journal of Physics: Conference Series,* vol. 13, pp. 63-66, 2005.

[86] D. Ren, H. Tan, Y. Xuan, Y. Han and Q. Li, "Apparatus for Measuring Spectral Emissivity of Solid Materials at Elevated Temperatures," *International Journal of Thermophysics,* vol. 37, pp. 1-20, 2016.

[87] Y. Xiao, C. Wan, A. Shahsafi, J. Salman, Z. Yu, R. Wambold, H. Mei, B. E. Rubio Perez, W. Derdeyn, C. Yao and M. A. Kats, "Precision Measurements of Temperature-Dependent and Nonequilibrium Thermal Emitters," *Laser Photonics Reviews,* vol. 14, p. 1900443, 2020.

[88] Specac, "High Temperature High Pressure cell," [Online]. Available: https://www.specac.com/en/products/ftir-acc/transmission/solid/high-temperature-high-pressure-cell. [Accessed 21 January 2022].

[89] Infrared Systems Development Corporation, "IR-563/301 Blackbody System," [Online]. Available: https://www.infraredsystems.com/Products/blackbody563.html. [Accessed 11 February 2022].

[90] R. M. Sova, M. J. Linevsky, M. E. Thomas and F. F. Mark, "High-temperature infrared properties of sapphire, AlON, fused silica, yttria, and spinel," *Infrared Physics & Technology,* vol. 39, pp. 251-261, 1998.

[91] R. M. Sova, M. J. Linevsky, M. E. Thomas and F. F. Mark, "High-temperature Optical Properties of Oxide Ceramics," *Johns Hopkins APL Technical Digest,* vol. 13, no. 3, pp. 368-378, 1992.

[92] E. Billur and H.-S. Son, "Aluminum-Based Coatings," in *Hot Stamping of Ultra High-Strength Steels,* Cham, Springer, 2019, pp. 63-65.

[93] I. Yakubtsov and R. Sohmshetty, "Evolution of Al-Si Coating Microstructure during Heat-Treatment of Usibor® 1500," *IOP Conference Series: Materials Science and Engineering,* vol. 418, p. 012015, 2018.

[94] M. Windmann, A. Röttger and W. Theisen, "Formation of intermetallic phases in Al-coated hot-stamped 22MnB5 sheets in terms of coating thickness and Si content," *Surface and Coatings Technology*, vol. 246, pp. 17-25, 2014.

[95] S. Fujita, S. J. Maki, H. I. Yamanaka and M. Kurosak, "Corrosion resistance after hot stamping of 22MnB5 steels aluminized with 80 g/m2 c.w. and ZnO coating," in *5th International Conference on Hot Sheet Metal Forming of High Performance Steel (CHS2)*, Toronto, 2015.

[96] C.-D. Wen, "Investigation of steel emissivity behaviors: Examination of Multispectral Radiation Thermometry (MRT) emissivity models," *International Journal of Heat and Mass Transfer*, vol. 53, pp. 2035-2043, 2010.

[97] C.-D. Wen and I. Mudawar, "Emissivity characteristics of polished aluminum alloy surfaces and assessment of multispectral radiation thermometry (MRT) emissivity models," *International Journal of Heat and Mass Transfer*, vol. 2005, pp. 1316-1329, 2005.

[98] P. G. Lucey, C. I. Honniball, J. G. Davis, S. Li and K. Hibbitts, "Water Absorption at 6 Microns: A New Tool for Remote Measurements of Lunar Surface Water Abundance and Variation," *Lunar and Planetary Science*, vol. 48, p. 1314, 2017.

[99] M. B. Pomfret, J. C. Owrutsky and R. A. Walker, "High-Temperature Raman Spectroscopy of Solid Oxide Fuel Cell Materials and Processes," *The Journal of Physical Chemistry B*, vol. 110, no. 35, pp. 17305-17308, 2006.

[100] P. Rostron, S. Gaber and D. Gaber, "Raman Spectroscopy, Review," *International Journal of Engineering and Technical Research*, vol. 6, no. 1, pp. 50-64, 2016.

[101] A. Kudelski, "Analytical applications of Raman spectroscopy," *Talanta*, vol. 76, no. 1, pp. 1-8, 2008.

[102] D. A. Long, "Raman spectroscopy," in *The Characterization of Chemical Purity: Organic Compounds*, New York, 1977, pp. 149-161.

[103] L. T. Kerr, H. J. Byrne and B. M. Hennelly, "Optimal choice of sample substrate and laser wavelength for Raman spectroscopic analysis of biological specimen," *Analytical Methods*, vol. 7, pp. 5041-5042, 2015.

[104] D. Wei, S. Chen and Q. Liu, "Review of Fluorescence Suppression Techniques in Raman Spectroscopy," *Applied Spectroscopy Reviews*, vol. 50, pp. 387-406, 2015.

[105] Y. Liu and R. D. L. Smith, "Identifying protons trapped in hematite photoanodes through structure-property analysis," *Chemical Science*, vol. 11, pp. 1085-1096, 2020.

[106] T. A. Harriman, D. A. Lucca, J.-K. Lee, M. J. Klopfstein, K. Herrmann and M. Nastasi, "Ion implantation effects in single crystal Si investigated by Raman spectroscopy," *Nuclear Instruments and Methods in Physics Research B,* vol. 267, pp. 1232-1234, 2009.

[107] L. A. Narayanan, F. H. Samuel and J. E. Gruzleski, "Crystallization Behavior of Iron-Containing Intermetallic Compounds in 319 Aluminum Alloy," *Metallurgical and Materials Transactions A,* vol. 25A, pp. 1761-1773, 1994.

[108] Y. Wang, H.-T. Li and Z. Fan, "Oxidation of Aluminium Alloy Melts and Onoculation by Oxide Particles," *Transactions of the Indian Institute of Metals*, vol. 65, no. 6, pp. 653-661, 2012.

[109] A. Mortensen, D. H. Christensen and O. F. Nielsen, "Raman Spectra of Amorphous Al_2O_3 and Al_2O_3/MoO_3 Obtained by Visible and Infrared Excitation," *Journal of Raman Spectroscopy,* vol. 22, pp. 47-49, 1991.

[110] A. Aminzadeh, "Excitation Frequency Dependence and Fluorescence in the Raman Spectra of Al_2O_3," *Applied Spectroscopy*, vol. 51, no. 6, pp. 817-819, 1997.

[111] D. L. A. de Faria, S. V. Silva and M. T. de Oliveira, "Raman Microspetroscopy of Some Iron Oxides and Oxyhydroxides," *Journal of Raman Spectroscopy,* vol. 28, pp. 873-878, 1997.

[112] S. P. S. Porto and R. S. Krishnan, "Raman Effect of Corundum," *The Journal of Chemical Physics*, vol. 47, no. 3, pp. 1009-1012, 1967.

[113] A. Aminzadeh and H. Sarikhani-fard, "Raman spectroscopic study of Ni/Al_2O_3 catalyst," *Spectrochimica Acta Part A,* vol. 55, pp. 1421-1425, 1999.

[114] V. K. Malinovsky, V. N. Novikov, N. V. Surovtsev and A. P. Shebanin, "Investigation of Amorphous States of SiO_2 by Raman Scattering Spectroscopy," *Physics of the Solid State,* vol. 42, no. 1, pp. 65-71, 2000.